



TECHNISCHE  
UNIVERSITÄT  
WIEN  
Vienna University of Technology

INSTITUT FÜR  
MECHANIK UND  
MECHATRONIK  
Mechanics & Mechatronics



## DIPLOMARBEIT

# Aeroacoustic simulation of flow parts in medical and automotive applications

ausgeführt zum Zwecke der Erlangung des akademischen Grades Diplom-Ingenieur  
unter der Leitung von

Univ.Prof. Dipl.-Ing. Dr.techn. Manfred Kaltenbacher  
Institut für Mechanik und Mechatronik  
Abteilung für Technische Akustik

Dipl.-Ing. Dr.techn. Stefan Schoder  
Institut für Mechanik und Mechatronik  
Abteilung für Technische Akustik

eingereicht an der Technischen Universität Wien

**Fakultät für Maschinenwesen und Betriebswissenschaften**

von

Andreas Wurzinger  
Matr.Nr.: 01526267  
Tiefenbachweg 37  
4101 Feldkirchen an der Donau

Wien, am 3. Dezember 2020

---

Andreas Wurzinger

# Eidesstattliche Erklärung

Ich erkläre an Eides statt, dass die vorliegende Arbeit nach den anerkannten Grundsätzen für wissenschaftliche Abhandlungen von mir selbstständig erstellt wurde. Alle verwendeten Hilfsmittel, insbesondere die zugrunde gelegte Literatur, sind in dieser Arbeit genannt und aufgelistet. Die aus den Quellen wörtlich entnommenen Stellen, sind als solche kenntlich gemacht.

Das Thema dieser Arbeit wurde von mir bisher weder im In- noch Ausland einer Beurteilerin/einem Beurteiler zur Begutachtung in irgendeiner Form als Prüfungsarbeit vorgelegt. Diese Arbeit stimmt mit der von den Begutachterinnen/Begutachtern beurteilten Arbeit überein.

Wien, am 3. Dezember 2020

\_\_\_\_\_  
Andreas Wurzinger



Die approbierte gedruckte Originalversion dieser Diplomarbeit ist an der TU Wien Bibliothek verfügbar.  
The approved original version of this thesis is available in print at TU Wien Bibliothek.

# Danksagung

An dieser Stelle möchte ich all jenen danken, die durch ihre fachliche und persönliche Unterstützung zum Gelingen dieser Diplomarbeit beigetragen haben.

Ich danke meinen Betreuern Dipl.-Ing. Dr.techn. Stefan Schoder und Univ.Prof. Dipl.-Ing. Dr.techn. Manfred Kaltenbacher für die zahlreichen hilfreichen Anregungen und Ideen sowie die konstruktive Kritik bei der Erstellung dieser Arbeit.

Ich danke meinen Kollegen Clemens Junger, Clemens Freidhager, Paul Maurerlehner und Florian Eberhart für die gute Zusammenarbeit und Hilfestellungen sowie dafür, dass ich mich immer wieder mit fachlichen und anderen spezifischen Fragen an Sie wenden konnte.

Ebenfalls gilt ein großer Dank an alle Beteiligten des Forschungsprojekts *Numerical computation of the human voice source*, insbesondere M.Sc. Sebastian Falk für das zügige Bereitstellen der Ergebnisse der Strömungssimulation, ohne die diese Arbeit nicht möglich gewesen wäre.

Abschließend gilt mein besonderer Dank meiner Familie, insbesondere meinen Eltern, die mir mein Studium ermöglicht und mich in all meinen Entscheidungen unterstützt haben.



Die approbierte gedruckte Originalversion dieser Diplomarbeit ist an der TU Wien Bibliothek verfügbar.  
The approved original version of this thesis is available in print at TU Wien Bibliothek.

# Kurzfassung

Ein Großteil aller weitverbreiteten technischen Anwendungen ist in der einen oder anderen Weise mit Schall verknüpft, sei es der gewünschten der gewünschte Schall von Musikinstrumenten oder die Geräusche von technischen Maschinen. Des Weiteren ist das Sprechen eine der wichtigsten Kommunikationsmethoden, welche üblicherweise im täglichen Leben als gegeben angenommen wird.

*Computational Aeroacoustics* (CAA) bietet eine Toolbox, um akustische Schallentstehung und Ausbreitung numerisch zu simulieren. Ein effizientes Werkzeug um strömungsinduzierten Schall zu simulieren, ist der in dieser Diplomarbeit vorgestellte hybride Ansatz. Dabei wird der Fokus auf den akustischen Teil sowie dafür notwendiges Pre-Processing gelegt.

Zuerst werden die Grundlagen der Strömungsmechanik und Akustik präsentiert, und die entsprechenden Differenzialgleichungen besprochen. Anschließend wird der Workflow Schritt für Schritt erklärt und ein kurzer Überblick über die verwendeten numerischen Methoden gegeben. Zusätzlich werden zwei verschiedene konservative Algorithmen zur Interpolation zwischen den Rechengittern von CFD (*Computational Fluid Dynamics*) und CAA bezüglich ihrer Anwendungsgrenzen untersucht. Abschließend wird der vorgestellte Ablauf auf ein Axialgebläse angewandt. Eine Gitternetz-Studie sowie die Validierung der Simulationsergebnisse mittels experimenteller Daten zeigen die Anwendbarkeit beider Algorithmen.

Außerdem beinhaltet diese Arbeit eine Quelltermanalyse der akustischen Quellen im menschlichen Stimmbildungsmechanismus. Dazu werden die lokale Zeitableitung des Strömungsdrucks sowie der konvektive Teil der rechten Seite der PCWE (Perturbed Convective Wave Equation) und Strömungsgrößen im Zeit- und Frequenzbereich dargestellt. Diese Darstellungen geben Einblick in den lokalen Einfluss des konvektiven Teils im Gegensatz zur breiter verteilten lokalen Zeitableitung des inkompressiblen Drucks der Strömung. Die Interpretation dieser Quellen liefert Erklärungen und Erkenntnisse für die im Zusammenhang mit dem Projekt *Numerical computation of the human voice source* entstandenen Simulationsergebnissen.



Die approbierte gedruckte Originalversion dieser Diplomarbeit ist an der TU Wien Bibliothek verfügbar.  
The approved original version of this thesis is available in print at TU Wien Bibliothek.

# Abstract

Most technical applications are connected with the production of sound, either as a main output or a by-product. Furthermore, speech is one of the most important human communication methods and the majority of people takes it for granted in everyday life. *Computational aeroacoustics* (CAA) provide a toolbox to numerically simulate sound generation and propagation. A computationally efficient tool to handle flow induced sound generation is the hybrid approach that is presented in this thesis. This hybrid approach incorporates a separation of fluid dynamics and acoustics. Thereby, this work focuses on the acoustic part and its pre-processing, investigating several key steps in the hybrid workflow.

Starting with the fundamentals of fluid dynamics and acoustics, the differential equations used in this work are presented. Thereafter, the CAA workflow is explained and a small overview of the numerical tools, that were used, is given. Furthermore, the conservative interpolation between CFD (*Computational Fluid Dynamics*) and CAA grids is investigated regarding the limitations of two different algorithms. Finally, these methods are applied to an axial fan. A grid study and validation with experimental data shows the applicability of both methods.

Additionally, this work includes a source term analysis of acoustic sources, generated during the human voice production mechanism. Therefore, the local time derivative and the convective part of the PCWE (Perturbed Convective Wave Equation) right-hand-side source, as well as various of their components and flow quantities are visualized in time and frequency domain. These visualizations yield insight in the localized impact of the convective source part in contrast to the more distributed local time derivative of the incompressible flow pressure. Furthermore, interpretation of the source fields delivers explanations for results obtained in the project *Numerical computation of the human voice source*.



Die approbierte gedruckte Originalversion dieser Diplomarbeit ist an der TU Wien Bibliothek verfügbar.  
The approved original version of this thesis is available in print at TU Wien Bibliothek.

# Contents

<b>1</b>	<b>Introduction</b>	<b>1</b>
1.1	Human Phonation . . . . .	1
1.2	Axial Fan Noise . . . . .	1
1.3	Aim of the Thesis . . . . .	2
<b>2</b>	<b>Governing Equations</b>	<b>3</b>
2.1	Fundamental physical principles of flow and sound . . . . .	3
2.1.1	Conservation of Mass . . . . .	3
2.1.2	Conservation of Momentum . . . . .	4
2.1.3	Navier-Stokes Equations . . . . .	5
2.1.4	Acoustic Wave Equation . . . . .	6
2.2	Characterization of Flows by Dimensionless Numbers . . . . .	7
2.3	Aeroacoustics . . . . .	8
2.3.1	Lighthill's Acoustic Analogy . . . . .	8
2.3.2	Perturbation Equations - Perturbed Convective Wave Equation . . . . .	9
<b>3</b>	<b>Computational Aeroacoustics</b>	<b>11</b>
3.1	Finite Element Method . . . . .	12
3.2	Open-domain problem . . . . .	13
3.3	Non-conforming Grids . . . . .	14
3.4	Conservative Interpolation . . . . .	14
3.4.1	Cell-centroid based interpolation . . . . .	14
3.4.2	Cut-volume cell weight interpolation . . . . .	16
3.4.3	Limitations of conservative interpolation schemes . . . . .	18
3.5	Grid convergence analysis . . . . .	27
<b>4</b>	<b>Application - Human Phonation</b>	<b>29</b>
4.1	Simulation Model . . . . .	29
4.1.1	Geometry . . . . .	30
4.1.2	Computational fluid dynamics (CFD) . . . . .	30
4.1.3	Computational aeroacoustics (CAA) . . . . .	31
4.2	Aeroacoustic source term analysis . . . . .	32
4.2.1	Flow quantities . . . . .	34

4.2.2	Aeroacoustic sources . . . . .	39
<b>5</b>	<b>Application - Axial Fan</b>	<b>51</b>
5.1	Experimental setup . . . . .	51
5.2	Simulation setup . . . . .	51
5.2.1	Computational fluid dynamics (CFD) . . . . .	51
5.2.2	Computational aeroacoustics (CAA) . . . . .	53
5.3	Comparison of the interpolation algorithm . . . . .	54
5.4	Artifacts inside the propagation domain . . . . .	56
5.5	Grid study . . . . .	57
<b>6</b>	<b>Conclusion and Outlook</b>	<b>63</b>
	<b>List of Figures</b>	<b>65</b>
	<b>List of Tables</b>	<b>67</b>
	<b>Bibliography</b>	<b>69</b>

# Chapter 1

## Introduction

In the field of computational multi-physics, each physical field coupling requires different methodologies to deal with its characteristics. Many of these methodologies however, are applicable to a wide range of applications and optimization goals. This work focuses on the numerical simulation of aeroacoustic phenomena applied to two applications. At first, human phonation and secondly, the flow-induced noise generated by an axial fan are analyzed, which represent two applications with completely different goal sets.

### 1.1 Human Phonation

Speech by voice is undoubtedly the most important tool in human communication, even increasing in importance with speech recognition finding application in more and more IoT devices replacing text or button input. Any health condition concerning the vocal tract can lead to not only complications in communication but also expressing emotions limiting the affected person in both an individual economic, and a social perspective, leading to isolation and depression [1, 2, 3]. In order to adequately treat any kind of malfunction of the human voice production, a deep understanding has to be achieved. As direct measurements are invasive and complicated to interpret, and experimental analysis is expensive and inflexible in most cases, this work focuses on a simulation model, modeling the fluid motion and acoustics within the vocal tract.

### 1.2 Axial Fan Noise

Besides the many use-cases of sound, the most common form of sound is in form of an unintended by-product. This noise can be unwanted in an applications because it can be an annoyance and degrade the user-experience, or even pose a danger for people's health causing increased stress levels, disturbed sleep or even hearing loss, if the exposure happens for a significant amount of time [4]. In automotive industry, the reduction and/or modification of the emitted noise spectrum is a key research goal. The axial fan is a very common part of any automobile implemented as the main provider

of cooling air for all types of engines or fuel cell stack, and battery packs. Therefore, a universal method to compute the flow-induced sound is for an axial fan can help to investigate the noise production mechanisms in order to minimize noise levels and/or predict the noise spectrum.

## 1.3 Aim of the Thesis

In this work, both problem sets are investigated using the same hybrid aeroacoustic approach, that is described in chapter 3. This hybrid approach separates the acoustics from the fluid dynamics. With the use of CFD, acoustic sources are computed from the flow quantities, that were provided by the project *Numerical computation of the human voice source*, a DFG (German Research Foundation) and FWF (Austrian Research Council) funded joint project by Universitätsklinikum Erlangen (Department for Phoniatics and Pedaudiology), TU Wien (Institute of Mechanics and Mechatronics) and TU Graz (Institute of Fundamentals and Theory in Electrical Engineering), or previous research projects by TU Wien, respectively. In chapter 4, these sources are investigated on the simulation model of an experimental vocal tract. Chapter 5 focuses on the used mesh, investigating the influence of grid interpolation and grid refinement. This thesis was created around the work on the publications on the two aforementioned topics [5, 6] and therefore overlaps in content. The aim of the thesis is to give a more detailed explanation of the used methodology and provide additional explanations of the published findings.

# Chapter 2

## Governing Equations

In this section, the fundamental physical principles of flow and sound are given, which all calculations are based on. Furthermore, the used aeroacoustic formulations are introduced.

### 2.1 Fundamental physical principles of flow and sound

The fundamental equations of fluid dynamics are the basis for this work and will be presented in the following section. For a Newtonian fluid like air, the conservation equations for mass, momentum, and energy lead to a set of equations which are referred to as flow equations. In this work, the conservation of energy can be neglected because of low Mach number flows (see section 2.2) and a non reacting medium. A detailed derivation of the flow equations is done in [7] and is not included in this work.

#### 2.1.1 Conservation of Mass

The conservation of mass states, that the total mass in a closed system is constant over time

$$\frac{dm}{dt} = 0 . \quad (2.1)$$

In continuum theory, this also applies to a differential element  $\delta m$

$$\frac{d \delta m}{dt} = 0 \quad (2.2)$$

The mass can be expressed by a product of element volume  $\delta V$  and density  $\rho$  which leads to

$$\frac{d \rho \delta V}{dt} = 0 \quad (2.3)$$

From this form, the conservation of mass can be obtained by applying Reynold's transport theorem:

$$\frac{\partial \rho}{\partial t} + \frac{\partial(\rho v_i)}{\partial x_i} = 0 \quad (2.4)$$

This equation states, that the sum of density change over time and the change in density and velocity due to convection has to be zero. This equation can be simplified for an incompressible flow with constant density  $\rho = \rho_0 = \text{const}$  to

$$\frac{\partial v_i}{\partial x_i} = 0 \quad (2.5)$$

This means, that for an incompressible flow, the divergence of the velocity field is zero at all times.

### 2.1.2 Conservation of Momentum

The conservation of momentum states, that the momentum change  $\delta I_j$  is caused by external forces  $f_i$

$$\frac{d \delta I_j}{dt} = f_j \quad (2.6)$$

The momentum can be expressed by a product of element mass  $\delta m$  and velocity field  $v_i$ , which leads to

$$\frac{d \delta I_j}{dt} = \frac{d}{dt}(\delta m v_j) = \delta m \frac{dv_j}{dt} + v_j \frac{d \delta m}{dt} \quad (2.7)$$

The second term in (2.7) vanishes because of the conservation of mass (2.1) and with  $\delta m = \rho \delta V$  the momentum change can be written as

$$\frac{d \delta I_j}{dt} = \rho \delta V \left( \frac{\partial v_j}{\partial t} + v_j \frac{\partial v_j}{\partial x_j} \right) \quad (2.8)$$

The external forces  $f_i$  can be split into surface forces  $\mathbf{S}$ , molecular momentum transport  $\mathbf{I}_M$ , and mass forces  $\mathbf{M}$

$$f_j = \sum \delta S_j + \frac{d}{dt} \delta I_{Mj} + \sum \delta M_j \quad (2.9)$$

The volume element mass forces  $\delta M_j$  can be calculated with the acceleration  $\mathbf{g}$

$$\delta M_j = \rho \delta V g_j \quad (2.10)$$

The element surface forces can be obtained from the difference in pressure on both sides of the volume element

$$\delta S_j = -p(x_j)(-\delta \Gamma_j) - p(x_j + \delta x_j)(\delta \Gamma_j) \quad (2.11)$$

with surface  $\delta\Gamma$ . Using a Taylor series expansion and neglecting terms of higher order, this leads to

$$\delta S_j = -\frac{\partial p}{\partial x_j} \delta V \quad (2.12)$$

If  $\tau_{ij}$  is the  $j$ -component of the momentum input per unit area in  $i$ -direction, then the forces due to molecular momentum transport can be written by the sum of in and output on both element sides

$$\frac{d}{dt} \delta I_{Mj} = -\tau_{ij}(x_i)(-|\delta\Gamma_i|) - \tau_{ij}(x_i + \delta x_i)(|\delta\Gamma_i|) \quad (2.13)$$

with surface  $\delta\Gamma$ . Again, applying a Taylor series expansion and neglecting higher order terms yields

$$\frac{d}{dt} \delta I_{Mj} = -\frac{\partial \tau_{ij}}{\partial x_i} \delta V \quad (2.14)$$

All the above stated terms combined and divided by the element volume  $\delta V$ , the conservation of momentum is written as

$$\rho \left( \frac{\partial v_j}{\partial t} + v_i \frac{\partial v_j}{\partial x_i} \right) = -\frac{\partial p}{\partial x_j} - \frac{\partial \tau_{ij}}{\partial x_i} + \rho g_j \quad (2.15)$$

### 2.1.3 Navier-Stokes Equations

In order to solve the conservation of momentum (2.15), a material model is needed to obtain a relation for the stress tensor  $\tau$ . For a Newtonian fluid, the viscous stresses arising from its flow are linearly dependent on the shear rate. As a result, the viscous tensor  $\tau$  can be written in terms of the velocity  $\mathbf{v}$  and the dynamic viscosity  $\mu$

$$\tau_{ij} = -\mu \left( \frac{\partial v_j}{\partial x_i} + \frac{\partial v_i}{\partial x_j} \right) + \frac{2}{3} \delta_{ij} \mu \frac{\partial v_k}{\partial x_k} \quad (2.16)$$

(2.16) inserted into (2.4) and (2.15) are called the *compressible Navier-Stokes equations*. For the compressible flow, the conservation of energy equation is needed additionally to solve the 5 unknowns  $\rho$ ,  $p$ , and the components of  $\mathbf{v}$ . For the incompressible case however, this set of equations is sufficient to fully model the flow. Assuming constant viscosity  $\mu = \mu_0 = \text{const}$  in addition to constant density  $\rho_0$ , the conservation of momentum can be written by

$$\rho_0 \left( \frac{\partial v_j}{\partial t} + v_i \frac{\partial v_j}{\partial x_i} \right) = -\frac{\partial p}{\partial x_j} + \mu_0 \frac{\partial^2 u_j}{\partial x_i^2} + \rho_0 g_j \quad (2.17)$$

(2.5) and (2.17) represent the *incompressible equations of fluid dynamics*. The above stated assumptions of constant density and viscosity valid for most flows of low Mach number ( $\text{Ma} \leq 0.3$ ).

As a starting point for some acoustic equations, the *Euler equations* are used. These are obtained by assuming an ideal invicid fluid with no molecular momentum transport, which simplifies (2.17) to

$$\rho \left( \frac{\partial v_j}{\partial t} + v_i \frac{\partial v_j}{\partial x_i} \right) = - \frac{\partial p}{\partial x_j} + \rho g_j \quad (2.18)$$

### 2.1.4 Acoustic Wave Equation

Considering acoustics, the fluid is assumed to be isentropic which results in pressure being only a function of the density. For linear acoustics, this results in the relation between the acoustic pressure  $p^a$  and acoustic density  $\rho^a$

$$p^a = \rho^a c_0^2 \quad (2.19)$$

with the constant speed of sound  $c_0$ . For air at standard conditions<sup>1</sup>, the speed of sound is for instance  $c_0 \approx 343 \text{ m/s}$ . To derive the acoustic wave equations, a so-called perturbation ansatz [8] is used, where the acoustic field is seen as a perturbation of the mean flow field

$$p = p_0 + p^a; \quad \rho = \rho_0 + \rho^a; \quad v = v_0 + v^a \quad (2.20)$$

with  $p^a \ll p_0$  and  $\rho^a \ll \rho_0$ .  $v^a$  is called acoustic particle velocity. Volume forces are neglected and the viscosity  $\mu$  is assumed to be zero, so that the viscous stress tensor  $\tau$  can be neglected as well. Furthermore, the mean velocity  $v_0$  is set to zero for simplification. Inserting the perturbation ansatz (2.20) into (2.4) and (2.15) yields

$$\frac{\partial (\rho_0 + \rho^a)}{\partial t} + \frac{\partial ((\rho_0 + \rho^a) v_i^a)}{\partial x_i} = 0 \quad (2.21)$$

$$(\rho_0 + \rho^a) \left( \frac{\partial v_j^a}{\partial t} + v_i^a \frac{\partial v_j^a}{\partial x_i} \right) = - \frac{\partial (p_0 + p^a)}{\partial x_j} \quad (2.22)$$

Then, assuming spatial and temporal constant mean density  $\rho_0$  and mean pressure  $p_0$  as well as neglecting second order acoustic terms (eg.  $\rho^a v_i^a$ ) results in a linear system of partial differential equations

$$\frac{\partial \rho^a}{\partial t} + \rho_0 \frac{\partial v_i^a}{\partial x_i} = 0 \quad (2.23)$$

$$\rho_0 \frac{\partial v_j^a}{\partial t} + \frac{\partial p^a}{\partial x_j} = 0 \quad (2.24)$$

or in vector notation with  $\nabla = \left( \frac{\partial}{\partial x_j} \right)$  as

$$\frac{\partial \rho^a}{\partial t} + \rho_0 \nabla \cdot \mathbf{v}^a = 0 \quad (2.25)$$

<sup>1</sup>dry air at a temperature of 20 °C

$$\rho_0 \frac{\partial \mathbf{v}^a}{\partial t} + \nabla p^a = \mathbf{0} \quad (2.26)$$

By applying the curl-operation to (2.26)

$$\nabla \times \frac{\partial \mathbf{v}^a}{\partial t} = \mathbf{0} \quad (2.27)$$

provides the information, that the particle velocity field is pure irrotational. Therefore, we can introduce the scalar acoustic potential  $\psi^a$  via

$$\mathbf{v}^a = -\nabla \psi^a \quad (2.28)$$

The relation between  $\psi^a$  and  $p^a$  can be obtained from inserting (2.28) into (2.26):

$$p^a = \rho_0 \frac{\partial \psi^a}{\partial t} \quad (2.29)$$

(2.25) can now be reformulated with (2.19) and (2.29) to arrive at the acoustic wave equation

$$\frac{1}{c_0^2} \frac{\partial^2 \psi^a}{\partial t^2} - \Delta \psi^a = 0 \quad (2.30)$$

with the Laplace operator  $\Delta = \left( \frac{\partial^2}{\partial x_j^2} \right)$ .

Alternatively the acoustic wave equation for the acoustic pressure  $p^a$  is obtained from exploring (2.19), (2.25), and (2.26)

$$\frac{1}{c_0^2} \frac{\partial^2 p^a}{\partial t^2} - \Delta p^a = 0 \quad (2.31)$$

## 2.2 Characterization of Flows by Dimensionless Numbers

In order to classify flow situations, dimensionless numbers are introduced.

The Reynolds number is defined by

$$\text{Re} = \frac{\mathcal{W}l}{\nu} \quad (2.32)$$

with the characteristic flow velocity  $\mathcal{W}$ , flow length  $l$ , and kinematic viscosity  $\nu = \frac{\mu}{\rho}$ . It represents the ratio between stationary inertia forces and viscous forces. The Reynolds number is therefore used to classify flows into laminar and turbulent flows.

The Mach number is defined by

$$\text{Ma} = \frac{\mathcal{W}}{c} \quad (2.33)$$

with the speed of sound  $c$ . It is used for an approximate subdivision into compressible ( $\text{Ma} > 0.3$ ) and incompressible flows ( $\text{Ma} \leq 0.3$ ).

## 2.3 Aeroacoustics

While for most applications the flow field can be modeled sufficiently accurate by assuming an incompressible medium, acoustic wave propagation requires a compressible medium. As the sound is more often than not a byproduct of or at least influenced by the flow field, the fully compressible flow equations need to be solved to obtain results for the flow field and acoustic field at once, which is complicated (for analytical solutions) and/or computationally expensive (for numerical solutions). In order to avoid this dilemma, so-called *aeroacoustic formulations* are used to separate the acoustics from the flow field, by defining acoustic sources, which are obtained from the flow field [9].

### 2.3.1 Lighthill's Acoustic Analogy

In technical applications, most unsteady flows are of high Reynolds number, and the acoustic radiation is a very small by-product of the motion. The turbulence of such flows is usually generated by fluid motion over a solid body and/or flow instabilities. Lighthill transformed the general conservation equations of mass and momentum in a similar way, as done in the derivation of the acoustic wave equation (see section 2.1.4), to arrive at an exact inhomogeneous wave equation whose source terms are important only within the turbulent region [10], [11].

Starting at the mass and momentum balance equations and neglecting any external force density

$$\frac{\partial \rho}{\partial t} + \nabla \cdot (\rho \mathbf{v}) = 0 \quad (2.34)$$

$$\frac{\partial \rho \mathbf{v}}{\partial t} + \nabla \cdot [\boldsymbol{\pi}] = 0 \quad (2.35)$$

with the momentum flux tensor

$$\pi_{ij} = \rho v_i v_j + (p - p_0) \delta_{ij} - \tau_{ij}, \quad (2.36)$$

and  $\delta_{ij}$  the Kronecker delta. Lighthill solved the equations for an ideal, linear acoustic medium where the momentum flux tensor simplifies to

$$\pi_{ij} \rightarrow \pi_{ij}^0 = p' \delta_{ij} = c_0^2 \rho' \delta_{ij} \quad (2.37)$$

with the fluctuating quantities

$$p' = p - p_0, \quad \rho' = \rho - \rho_0, \quad (2.38)$$

which are not equal to the corresponding acoustic quantities  $p^a$  and  $\rho^a$  but rather a superposition of flow and acoustic parts. This led to the well-known *Lighthill equation*

$$\frac{\partial^2 \rho'}{\partial t^2} - c_0^2 \nabla \cdot \nabla \rho' = \frac{\partial^2 L_{ij}}{\partial x_i \partial x_j} \quad (2.39)$$

with

$$L_{ij} = \pi_{ij} - \pi_{ij}^0 = \rho v_i v_j + (p' - c_0^2 \rho') \delta_{ij} - \tau_{ij} \quad (2.40)$$

known as the *Lighthill stress tensor*.

$L_{ij}$  does not account for the generation of sound only. It also describes acoustic *self modulation* caused by ([8])

- acoustic nonlinearity,
- the convection of sound waves by the turbulent flow velocity,
- refraction caused by sound speed variations,
- and attenuation due to thermal and viscous actions.

Neglecting these,  $L_{ij}$  can be simplified to

$$L_{ij} \approx \rho_0 v_i v_j \quad (2.41)$$

for  $\text{Ma}^2 \ll 1$ . With Green's function, an integral solution for (2.39) can be calculated. The density fluctuation at a coordinate  $\mathbf{x}$  and time  $t$  can be obtained from

$$c_0^2 \rho'(\mathbf{x}, t) = \frac{1}{4\pi} \frac{\partial^2}{\partial x_i \partial x_j} \int_{-\infty}^{\infty} \frac{L_{ij}(\mathbf{y}, t - \frac{|\mathbf{x}-\mathbf{y}|}{c_0})}{|\mathbf{x} - \mathbf{y}|} d\mathbf{y}, \quad (2.42)$$

where  $\mathbf{y}$  is the source coordinate.

The main restriction of Lighthill's aeroacoustic analogy (2.42) in its integral form is the restriction, that it can describe free radiation only, because Green's function for free radiation was used to incorporate the initial and boundary conditions. Extensions to the presented analogy to make it more generally applicable and also address solid boundaries in the integral form were proposed by Curle [12] and Ffowcs-Williams and Hawkings (FWH) [13].

### 2.3.2 Perturbation Equations - Perturbed Convective Wave Equation

Based on the idea that physical quantities of the flow field can be split into compressible and incompressible parts, an acoustic/viscous splitting technique for the prediction of flow induced sound was introduced in [14]. [15, 16, 17, 18] presented alternative and improved formulations for linear and non-linear wave propagation.

The flow field quantities are therefore decomposed into mean ( $\bar{p}$ ,  $\bar{\mathbf{v}}$ ,  $\bar{\rho}$ ) and fluctuating

parts. Additionally, the fluctuating parts are split into acoustic  $(p^a, \mathbf{v}^a, \rho^a)$  and flow components  $(p^{ic}, \mathbf{v}^{ic})$ , which are assumed to be incompressible.

$$p = \bar{p} + p^{ic} + p^c = \bar{p} + p^{ic} + p^a \quad (2.43)$$

$$\mathbf{v} = \bar{\mathbf{v}} + \mathbf{v}^{ic} + \mathbf{v}^c = \bar{\mathbf{v}} + \mathbf{v}^{ic} + \mathbf{v}^a \quad (2.44)$$

$$\rho = \bar{\rho} + \rho_1 + \rho^a \quad (2.45)$$

Furthermore, a density correction  $\rho_1$  is used in equation 2.45. A detailed derivation of the perturbation equations for both, compressible and incompressible flows is done in [19]. For an incompressible flow the above stated decomposition leads to the following perturbation equations

$$\frac{\partial p^a}{\partial t} + \bar{\mathbf{v}} \cdot \nabla p^a + \rho_0 c_0^2 \nabla \cdot \mathbf{v}^a = -\frac{\partial p^{ic}}{\partial t} - \bar{\mathbf{v}} \cdot \nabla p^{ic} \quad (2.46)$$

$$\rho_0 \frac{\partial \mathbf{v}^a}{\partial t} + \rho_0 \nabla (\bar{\mathbf{v}} \cdot \mathbf{v}^a) + \nabla p^a = 0 \quad (2.47)$$

with spatial constant mean density  $\rho_0$  and speed of sound  $c_0$ , which is an equivalent system of partial differential equations as published in [16]. Introducing the scalar acoustic potential  $\psi^a$  as defined in section 2.1.4 (2.47) can be reformulated to

$$\nabla \left( \rho_0 \frac{\partial \psi^a}{\partial t} + \rho_0 \bar{\mathbf{v}} \cdot \nabla \psi^a - p^a \right) = 0 \quad (2.48)$$

which gives

$$p^a = \rho_0 \frac{\partial \psi^a}{\partial t} + \rho_0 \bar{\mathbf{v}} \cdot \nabla \psi^a = \rho_0 \frac{D\psi^a}{Dt} \quad (2.49)$$

Finally, by substituting (2.49) into (2.46), we arrive at the *Perturbed Convective Wave Equation* (PCWE)

$$\frac{1}{c_0^2} \frac{D^2 \psi^a}{Dt^2} - \Delta \psi^a = -\frac{1}{\rho_0 c_0^2} \frac{Dp^{ic}}{Dt} \quad (2.50)$$

This convective equation for the scalar acoustic potential fully describes the acoustic sources, which are generated by incompressible flow structures and its wave propagation through the flowing medium [8]. The source term is calculated by taking the substantial derivative

$$\frac{D}{Dt} = \frac{\partial}{\partial t} + \bar{\mathbf{v}} \cdot \nabla \quad (2.51)$$

of the incompressible pressure. For rotating mesh regions, the mean velocity has to be corrected by the rotational velocity  $\mathbf{v}_r$  of the mesh

$$\frac{D}{Dt} = \frac{\partial}{\partial t} + (\bar{\mathbf{v}} - \mathbf{v}_r) \cdot \nabla \quad (2.52)$$

# Chapter 3

## Computational Aeroacoustics

One of the key challenges in computational aeroacoustics (CAA) is the scale disparity between the flow structures and the acoustic wavelengths, especially in low Mach number applications. To solve the compressible flow equations directly both scales have to be resolved from the sound generating vortices to the microphone positions of interest. This leads to both, a very high number of cells but also a very small required time step size to minimize dissipation effects of the acoustic waves.

To solve this problem, hybrid CAA schemes are introduced, to separate the flow from the acoustic computation (e.g., see [20], [21]).

This allows a workflow as depicted in Fig. 3.1. Starting from a mesh, that is optimized for CFD computations (CFD-Grid: high resolution at wall regions and low resolution near outflow boundaries), the incompressible flow field is calculated using CFD-software (eg. *OpenFOAM*, *Ansys Fluent*, *Star CCM+*). Using an aeroacoustic formulation, eg. the in section 2.3 presented ones, the acoustic sources are computed from the flow field results. These acoustic sources are then interpolated to a different mesh, that is optimized for acoustic computations (CAA Grid: Uniform element size over the whole domain). The acoustic wave propagation is then computed with an FE-solver (eg. *openCFS*<sup>1</sup>, former *CFS++* [22]). Finally, the resulting acoustic potential respectively acoustic pressure can be validated with measurement data using post-processing methods (eg. Fourier transformation, calculation of sound pressure levels,...).

In this chapter an basic idea of the Finite Element method, that is used to perform the numerical simulation of the partial differential equations describing the wave propagation, which are introduced in chapter 2, is given. Furthermore, 2 different interpolation algorithms are presented and analyzed to interpolate the acoustic sources from the flow solution to the acoustic mesh. Finally, a method to quantify and evaluate grid convergence is described.

---

<sup>1</sup><https://opencfs.org/>

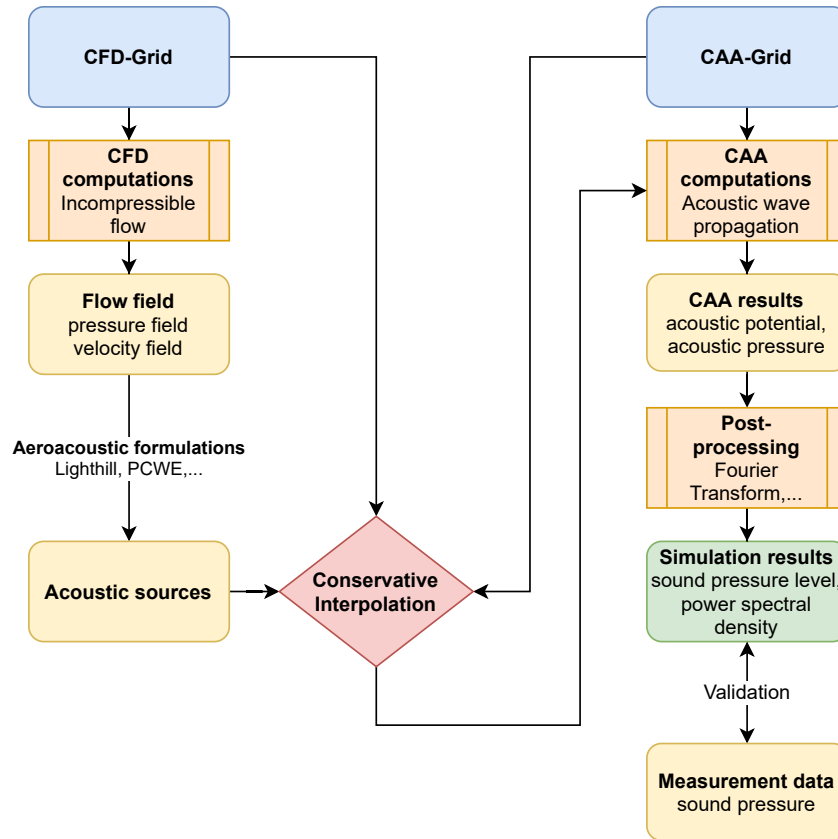


Figure 3.1: Workflow of a typical hybrid CAA scheme, as used in this work.

### 3.1 Finite Element Method

The finite element method (FEM) is a universal tool to solve systems of partial differential equations (PDE) numerically. In contrast to the similar finite difference and finite volume methods, the FEM is well suited to many multi-physics problems including aeroacoustics. It is based on separating the computational domain into a finite number of elements for which the geometrical distribution of the unknown quantity is approximated by so-called Ansatz-functions to reduce the PDEs to a linear algebraic system of equations for the nodal values (of the Lagrangian (nodal) finite elements).

In order to get to the system of algebraic linear equations (ALEs), at first the strong formulation (PDE and given boundary and initial conditions) is transformed into the weak formulation by multiplying the PDE by a test function  $w$  and integrating over the whole computational domain  $\Omega$ . For the acoustic wave equation of linear acoustics, Eq. (2.31) and a set of boundary (e.g.  $p^a(t, \mathbf{x} = \Gamma) = p_{bc}^a$ ) and initial conditions (e.g.  $p^a(t = 0, \mathbf{x}) = p_0^a$  and  $\frac{\partial p^a(t=0, \mathbf{x})}{\partial t} = \dot{p}_0^a$ ) yield

$$\int_{\Omega} w \left( \frac{1}{c_0^2} \frac{\partial^2 p^a}{\partial t^2} - \nabla \cdot \nabla p^a \right) d\Omega = 0 \quad (3.1)$$

which can be reformulated by using integration by parts to

$$\int_{\Omega} \frac{1}{c_0^2} w \frac{\partial^2 p^a}{\partial t^2} d\Omega + \int_{\Omega} \nabla w \cdot \nabla p^a d\Omega = 0 \quad (3.2)$$

neglecting the term  $-\int_{\Gamma} w \frac{\partial p^a}{\partial \mathbf{n}} d\Gamma$  because  $w$  is chosen to be 0 on the boundary. If now  $p^a$  and  $w$  are both replaced by the Ansatz

$$u(t, \mathbf{x}) \approx \sum_{i=1}^n N_i(\mathbf{x}) x_i(t) \quad (3.3)$$

with the number of nodes  $n$  and the Ansatz-functions  $N_i$  this leads to the semi-discrete Galerkin formulation

$$\mathbf{M} \frac{\partial^2 \mathbf{p}^a}{\partial t^2} + \mathbf{K} \mathbf{p}^a = \mathbf{f} \quad (3.4)$$

with the vector of unknown node values  $\mathbf{p}^a$ , the system matrices  $\mathbf{M}$  and  $\mathbf{K}$ , and the load vector  $\mathbf{f}$  due to boundary conditions. For the time discretization, the Newmark method [23] can be used to finish at the system of ALEs.

## 3.2 Open-domain problem

Acoustic problems often include regions, where free radiation in an open domain needs to be simulated. Especially for long simulations, this creates a problem as the standard Dirichlet and Neumann boundary conditions result in total reflection of the acoustic wave. To be able to still use an efficient (and therefore small) computational domain, absorbing boundary conditions (ABC) and/or perfectly matched layers (PML) can be used to ensure a free radiation condition on the boundary.

An ABC is designed to let all waves moving from inside out pass without reflection while reflecting any wave that moves in the opposite direction. This behavior can be realized by a boundary

$$\frac{\partial p^a}{\partial \mathbf{n}} = -\frac{1}{c} \frac{\partial p^a}{\partial t} \quad (3.5)$$

which ensures perfect free radiation for any wave, that impinges orthogonal to the boundary surface.

The idea of the perfectly matched layer is to have an additional layer on the boundary which does not reflect any wave on the inner boundary but numerically damps any wave that is propagating in the PML domain. This is realized by using complex material properties  $\tilde{c} = \frac{c}{1-j\sigma_0}$ ,  $\tilde{\rho} = \rho(1-j\sigma_0)$  and an according damping function  $\sigma_0$ . A proof of the feasibility and optimality of certain damping functions can be found in [22].

### 3.3 Non-conforming Grids

In order to discretize complex geometries and connect moving with static regions it is often necessary to use an irregular grid. These non-conforming interfaces need special treatment so that they still ensure continuity requirements.

Classical Mortaring introduces therefore Lagrange multipliers to incorporate the interface conditions which results in a saddle-point problem that requires special solvers to solve. Nitsche-Type Mortaring, which is used in all following computations, in contrast adds a term to make the system matrices symmetric, and additionally a penalty term in order to ensure the interface conditions. For a detailed explanation of both methods it is referred to [22].

### 3.4 Conservative Interpolation

In the weak form of the partial differential equation used for the finite element method, the source term is written as

$$\int_{\Omega} \Phi f^a d\xi \quad (3.6)$$

where  $\Phi$  is the test function,  $\Omega$  the computational domain, and  $f^a$  the aeroacoustic sources. In a hybrid workflow, (3.6) is calculated according to a suitable aeroacoustic formulation, as described in 2.3, on the flow grid (superscript f in the following section), and then interpolated onto the acoustic grid (superscript a in the following section). This leads to an interpolation in which the integral property of the aeroacoustic sources used by the finite element simulation is conserved. Therefore, the following interpolation methods are called *conservative interpolation methods*.

#### 3.4.1 Cell-centroid based interpolation

The cell-centroid based approach conserves the energy globally but approximates the local energy conservation of the finite element right-hand side by

$$F_i^a = \int_{E^a} N_i^a(\boldsymbol{\xi}) f^a d\xi \approx \sum_{k \in M^f} N_i^a(\boldsymbol{\xi}_{E_k^f}) F_k^f, \quad (3.7)$$

where  $E_k^f$  denotes the cell of the flow grid,  $\boldsymbol{\xi}_{E_k^f}$  the local coordinate,  $M^f$  the number of flow cells, and the index  $i$  the node number on the CAA grid. In order to preserve the acoustic energy, the loads  $F_k^f$  of the fine flow grid are interpolated onto the coarser acoustic grid (see Fig. 3.2).

For an acoustic element, the cell-centroid based approach (Algo. 1) includes all loads  $F_k^f$  which are located in the acoustic finite element  $E^a$ . This geometric connection from the load location to the acoustic element is taken into account by the set  $M^f$ . Based on the

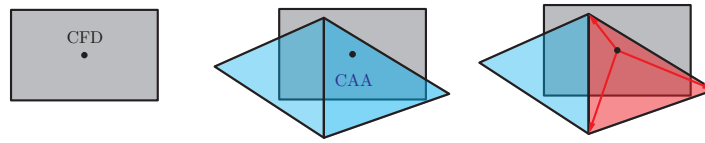


Figure 3.2: Cell-centroid based approach for conservative interpolation. [24]

geometric properties, the loads are weighted by the finite element basis functions and summed up to the acoustic grid. The loads

$$F_k^f = \bigwedge_{l \rightarrow k} \int_{E_l^f} N_l^f(\boldsymbol{\xi}) f^f(\boldsymbol{\xi}) d\xi \quad (3.8)$$

are assembled on the CFD mesh in terms of the finite element method, by the assembly operator  $\bigwedge$ . In order to reduce the computational complexity of (3.8) and to create a computationally efficient algorithm, the integration over the source volume is simplified to a first order volume weighting

$$F_k^f = V_{E_k^f} f_k^f(\boldsymbol{\xi}_{E_k^f}). \quad (3.9)$$

This also avoids the finite element assembly operator. The error introduced by this approximation can be estimated based on a Taylor series and is thus bounded by the product of the characteristic grid size and the gradient of the interpolated quantity, which is assumed to be small for a high quality flow grid.

---

**Algorithm 1** Cell-centroid based interpolation [24]

---

```

1:  $\mathbf{F}^a \leftarrow \text{CentroidInterpolation}(E^a)$ 

2: function CENTROIDINTERPOLATION
3:   for  $i$  in  $E^a$  do
4:      $M^f = \text{GetAllCFDCellsOfCAAElementByCFDCellCenter}(i)$  ▷  $M^f$  holds
       indices of CFD Cells
5:     for  $k$  in  $M^f$  do
6:        $V_{E_k^f} = \text{GetVolumeOfCFDCell}(k)$ 
7:        $F_k^f = \text{ComputeFEMLoadOnCFD}(k)$  ▷ Compute (3.9)
8:        $\mathbf{x}_k = \text{GetCentroidOfCFDCell}(k)$ 
9:        $F_i^a = \text{InterpolateFEMLoadToCAAMesh}(\mathbf{x}_k)$  ▷ Finite element
       interpolation to CAA element (3.7)
10:    end for
11:  end for
12: end function

```

---

As illustrated in Fig. 3.2, the algorithm has to find the nodal source location  $\mathbf{x}_k$  inside an acoustic element (set  $M^f$ ). This global position  $\mathbf{x}_k$  corresponds to a local position  $\boldsymbol{\xi}_{E_k^f}$

in the reference finite element ( $\mathbf{x}_k \rightarrow \boldsymbol{\xi}_{E_k^f}$ ). Finally, the loads  $F_k^f$  are interpolated to the nodes of the acoustic mesh using the finite element basis functions  $N_i^a$  [25]. Considering Fig. 3.2, only one of the two CAA elements will receive values during the interpolation (the right element containing the center location). Consequently, there could be elements having zero nodal values. To describe the observed mechanism, we define a frequency-wavenumber relation (FWR) for a physical quantity (e.g. acoustic pressure, aeroacoustic source term)

$$\omega = f(\|\mathbf{k}\|_2), \quad (3.10)$$

where  $\omega$  is the frequency and  $\mathbf{k}$  the wavenumber; This relation is similar as the dispersion relation for hyperbolic differential operators. However, the limited capability of the interpolation scheme destroys the FWR of the interpolated aeroacoustic sources  $\omega \neq f(\|\mathbf{k}\|_2)$ . Therefore, if target elements receive zero values, then deviations in the underlying wave number of the interpolated field can be expected. [24]

### 3.4.2 Cut-volume cell weight interpolation

The cell-centroid based approach (section 3.4.1) works accurately in cases where the flow grid is much finer than the acoustic grid. However, the mesh size of flow computations varies from fine meshes resolving boundary layers to coarse meshes towards regions without flow gradients. Consequently, hybrid aeroacoustics deal with regions, in which the flow grid is of similar or larger size than the acoustic mesh (see Fig. 3.3). In these cases, the cell-centroid based approach fails locally because it neglects the contributions weighted by the volume.

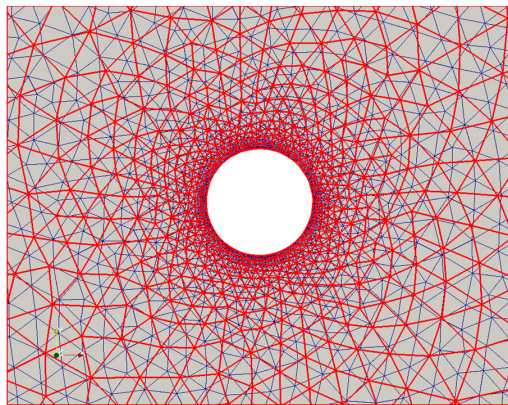


Figure 3.3: General mesh sizes of flow and acoustic grid: CFD grid (red) and CAA grid (blue).

Thus, an improved approach considers for each acoustic volume element  $E_i^a$  the set of flow cells  $E^f$  that intersect

$$E_l^{f \cap a} = E_l^a \cap E^f \quad (3.11)$$

with the respective acoustic volume element [24]. This improved approach conserves the energy globally as well as locally for different mesh sizes and calculates the finite element right-hand side by

$$\int_{E^a} N_i^a(\boldsymbol{\xi}) f^a d\xi = \sum_{k \in M^{f \cap a}} N_i^a(\boldsymbol{\xi}_k) F_k^{f \cap a}. \quad (3.12)$$

Based on this intersection, the loads  $F_k^{f \cap a}$  are volume-weighted,

$$F_k^{f \cap a} = \bigwedge_{l \rightarrow k} \int_{E_l^{f \cap a}} N_l^f(\boldsymbol{\xi}) f^f(\boldsymbol{\xi}) d\xi. \quad (3.13)$$

In order to avoid the finite element assembly operator in (3.13), it is assumed that the aeroacoustic source term is constant over the fluid cell. Therefore, the integral is reduced to a multiplication of the intersection volume  $V_c \rightarrow V_{E_l^{f \cap a}}$  by the source density  $f_l^f$  at the volumetric center  $\mathbf{x}_c \rightarrow \boldsymbol{\xi}_{E_l^{f \cap a}}$  of the intersection polyhedron

$$F_k^{f \cap a} = V_{E_k^{f \cap a}} f_k^f(\boldsymbol{\xi}_{E_k^{f \cap a}}). \quad (3.14)$$

The algorithmic workflow is depicted in Fig. 3.4. In contrast to the cell-centroid based approach, first, the intersecting cells are determined and then the volumetric center  $\mathbf{x}_c \rightarrow \boldsymbol{\xi}_{E_l^{f \cap a}}$  and the volume of the intersection polyhedron  $V_c \rightarrow V_{E_l^{f \cap a}}$  are computed.

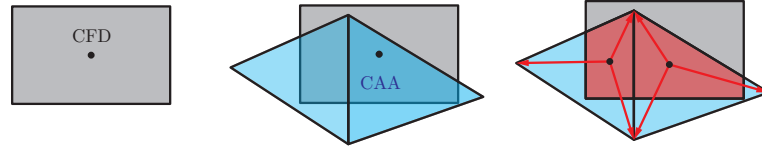


Figure 3.4: Steps for intersection and interpolation based on cut-volume cell approach. [24]

This additional intersection information enables the source contribution weighted, with the intersection volume, to be added to the nodes of the acoustic element, by using the finite element basis functions evaluated at the center of the polyhedron (see Fig. 3.4). Thereby, cases in which acoustic elements are smaller and embedded into a single flow cell are also covered.

For variable acoustic sources within one fluid cell, the full finite element framework has to be carried out during the conservative interpolation. An additional interpolation or regression step must be executed to construct a function basis. Then the source density  $f_l^f$  could be raised from the lowest order polynomial space to an arbitrary order. As a consequence, the integral (3.13) must be computed which involves matrix multiplications instead of scalar multiplications. Therefore, the centroid position and the volume of a fluid cell have to be transformed to the reference finite element.

**Algorithm 2** cut-volume cell interpolation [24]

---

```

Fa ← CutVolumeCellInterpolation(Ea)

2: function CUTVOLUMECELLINTERPOLATION
   for i in Ea do
4:     Mf∩a = IntersectCFDGridWithCAACell(i)    ▷ Mf∩a holds indices of CFD
       Cells
       for k in Mf∩a do
6:         VEf∩ak = GetIntersectionVolumeOfCFDCell(k)
           Fkf∩a = ComputeFEMLoadOnCFD(k)           ▷ Compute (3.14)
8:         xk = GetCentroidOfIntersectionCell(k)
           Fia = InterpolateFEMLoadToCAAMesh(xk)   ▷ Finite element
           interpolation to CAA element (3.12)
10:        end for
       end for
12: end function

```

---

**3.4.3 Limitations of conservative interpolation schemes**

As mentioned above, both of the presented interpolation schemes conserve the energy either globally (cell-centroid scheme) or both globally and locally (cut-volume scheme). Due to the necessary simplifications that are made in the derivation to make them computationally efficient, and the interpolation itself, which is an approximation method, there are limits to the possible refinement and coarsening of the mesh (represented by small or large mesh ratios). The following section summarizes the findings from [6] on the limitations of the presented conservative interpolation schemes.

**Limitation for fine CAA meshes**

In [6] the cell-centroid based conservative interpolation and the cut-volume cell approach are compared and verified against an analytic function

$$f(\mathbf{x}) = \sin(3\pi x) \quad (3.15)$$

on the domain  $\Omega \in [0, 1]^2$ . Considering the cell-centroid based approach, energy errors will occur for large mesh ratios  $\Gamma$

$$\Gamma = \frac{N_{\text{CAA}}}{N_{\text{CFD}}}, \quad (3.16)$$

where  $N_{\text{CAA}}$  is the number of nodes on the edges of the CAA mesh and  $N_{\text{CFD}}$  is the number of nodes on the edges of the CFD mesh. Figure 3.5 shows how the FE nodal right-hand side values develop on a line at  $y = 0.5$ . Along the evaluation line, the number of nodes of the CFD grid are constant for the different evaluations (101 nodes). In contrast to that, the number of nodes along the CAA mesh varies according to the mesh

ratio. If  $\Gamma < 1$ , the CFD grid is finer than the CAA mesh; for  $\Gamma > 1$ , the CFD grid is coarser than the CAA mesh. The cell-centroid based interpolation performs satisfactorily for low mesh ratios where the CFD grid is finer than the CAA mesh. For larger mesh ratios, the cell-centroid based interpolation exhibits spurious modes and energy is non-physically transferred to shorter wavelengths. In contrast, the cut-volume cell approach has the desired conservative properties for all mesh ratios.

Based on Parseval's theorem, the relative energy content of the real wavelength  $\lambda_a$  compared to the total energy is evaluated by the energy ratio  $e_r$

$$e_r = \frac{(\hat{D}_{\text{RHS}}(\lambda_a))^2}{\sum_{k=1}^N (\hat{D}_{\text{RHS}}(\lambda_k))^2}. \quad (3.17)$$

$\hat{D}_{\text{RHS}}$  are the amplitudes of the discrete wave number transform at the corresponding wavenumber. Table 3.1 compares the cell-centroid based conservative interpolation (cell-centroid) to the conservative cut-volume cell interpolation (cut-volume cell). As expected, the more accurate conservative cut-volume cell interpolation significantly outperforms the cell-centroid based procedure. However, the computational demand increases with the number of cell intersections. Compared to the setup time of the cell-centroid based approach, the setup time for the cut-volume cell intersection takes about 50 times as long but overall, the computational demand increases linearly.

Additionally to the mesh ratio  $\Gamma$ , Tab. 3.1 lists the coverage ratio  $\varepsilon$ , which describes the ratio of CAA cells that are covered by CFD cells relative to the total number of CAA cells. For example, the CAA mesh in Fig. 3.2 has a coverage ratio of  $\varepsilon = 0.5$ ; reddish cells are covered and bluish cells are not covered. It is obvious that the energy ratio  $e_r$  for the cell-centroid based interpolation decreases with decreasing coverage ratio  $\varepsilon$ . Closer examination of the relation between  $e_r$  for the cell-centroid based interpolation and  $\varepsilon$  revealed that  $e_r \sim 1 - (1 - \varepsilon)^3$ .

For large mesh ratios  $\Gamma$ , the cell-centroid interpolation fails to conserve the frequency-wavenumber-relation (FWR) of linear acoustics

$$\omega = c\sqrt{\|\mathbf{k}\|_2}, \quad (3.18)$$

where  $\omega$  is the frequency and  $\mathbf{k}$  the wave number. The cell-centroid interpolation also fails to conserve the FWR of fluid dynamics. In this case, the CAA mesh re-samples the contributions of the CFD grid and redistributes them towards wrong wave numbers  $\mathbf{k}$  that are connected to the spatial occurrence of the CFD values. Figure 3.6 highlights the fact of Fig. 3.5, which demonstrates the spatial redistribution of a source term for a specific frequency  $f$ .

The transformation of the RHS (see Fig. 3.5 as a function over space coordinate  $x$ ) into the wavenumber space for a specific frequency of  $f = 3c/2$  leads to a spectrum in terms of an amplitude wavenumber pair (see Fig. 3.6). Each amplitude, exceeding the 1/3 threshold of the amplitude at the wavelength of ( $\lambda = 2/3m$ ), results in a scatter plot mark.

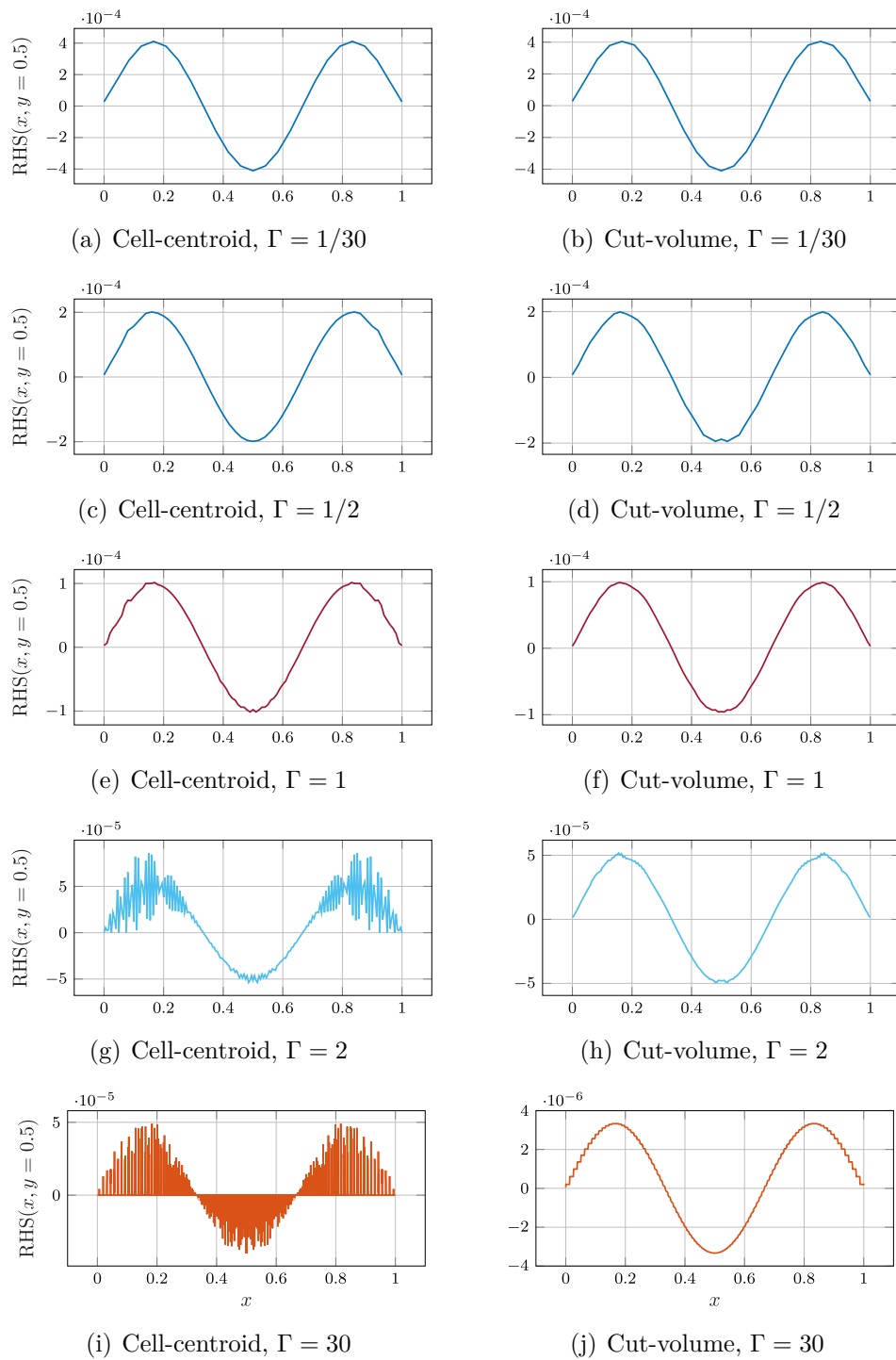


Figure 3.5: RHS values of FE nodes at  $y = 0.5$  in  $x$ -direction. The nr. of nodes on the CFD grid along the evaluation line is 101; whereas the nr. of nodes on the CAA grid along the line is based on the mesh ratio  $\Gamma$ .  $\Gamma < 1$ : the CFD grid is finer than the CAA mesh;  $\Gamma > 1$ : the CFD grid is coarser than the CAA mesh. In (a, c, e, g, i) the cell-centroid based interpolation and in (b, d, f, h, j) the cut-volume cell approach is illustrated for different mesh ratios.

Table 3.1: Ratio of the energy corresponding to the actual wavelength and the total energy for the cell-centroid based procedure and the cut-volume cell procedure, respectively.

$\Gamma$	Coverage ratio $\varepsilon$	Energy ratio $e_r$		cell-centroid	cut-volume
		cell-centroid	cut-volume	CPU time	CPU time
1/30	99.99 %	99.31 %	99.27 %	0.278 s	3.26 s
0.5	99.98 %	99.28 %	99.22 %	0.282 s	4.39 s
1	87.18 %	99.17 %	98.92 %	0.279 s	6.61 s
2	50.29 %	85.48 %	98.79 %	0.368 s	10.983 s
5	20.2 %	52.55 %	98.85 %	0.562 s	23.938 s
10	10.1 %	31.72 %	98.94 %	0.835 s	46.158 s
20	5.05 %	15.73 %	99.04 %	1.457 s	88.403 s
30	3.37 %	11.03 %	99.1 %	2.048 s	129.853 s

The scatter plot reveals that spatial features are redistributed into the range, where typically high Mach number fluctuations are present. This behavior is more dominant for the cell-centroid interpolation as the comparison of the two subplots shows and was previously concluded from Fig. 3.5. Furthermore, these high wavenumber oscillations increase in size and extend for increasing mesh ratios  $\Gamma$ .

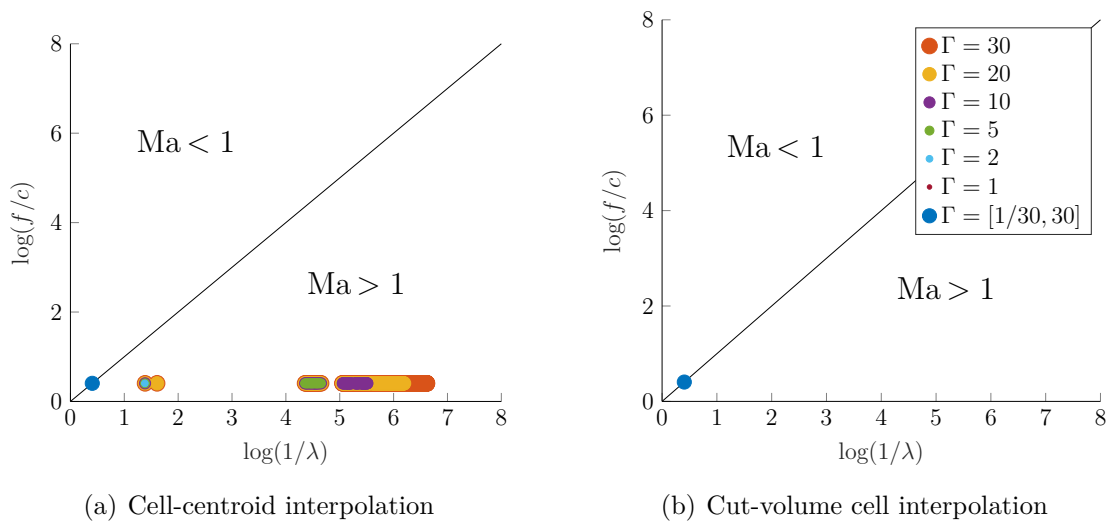


Figure 3.6: The plots show the wave number content of the source signal for the different interpolation methods. The dots show different CAA and CFD mesh combinations.

### Limitation for coarse CAA meshes

Besides mesh refinement there also result limitations, when the CAA mesh becomes coarse in comparison to the CFD mesh. In this section the effects of possible coarseness of the acoustic grid compared to the CFD grid are described according to [6]. Therefore, the cut-volume cell and the cell-centroid based approach are verified numerically for generic source distributions. The verification example uses two-dimensional analytic source fields, where the source distributions are given in Eq. (3.19)–(3.21). These distributions correspond to a monopole, dipole, and quadrupole and are determined solely by the coordinates  $x$  and  $y$ , and the spatial parameter  $\sigma = 0.75$  m. For a source exhibiting monopole radiation, the spatial parameter  $\sigma$  is in the range of the displacement thickness. Considering the dipole sources, the spatial parameter  $\sigma$  is the distribution of a pressure loading of a surface and in the case of a quadrupole, the spatial parameter  $\sigma$  is a measure for the eddy diameter.

$$f_{\text{MP}} = \frac{1}{\sqrt{2\pi\sigma^2}} e^{-\frac{x^2+y^2}{2\sigma^2}} \quad (3.19)$$

$$f_{\text{DP}} = \frac{-x}{\sqrt{2\pi\sigma^2} \cdot \sigma^2} e^{-\frac{x^2+y^2}{2\sigma^2}} \quad (3.20)$$

$$f_{\text{QP}} = \frac{xy}{\sqrt{2\pi\sigma^2} \cdot \sigma^4} e^{-\frac{x^2+y^2}{2\sigma^2}} \quad (3.21)$$

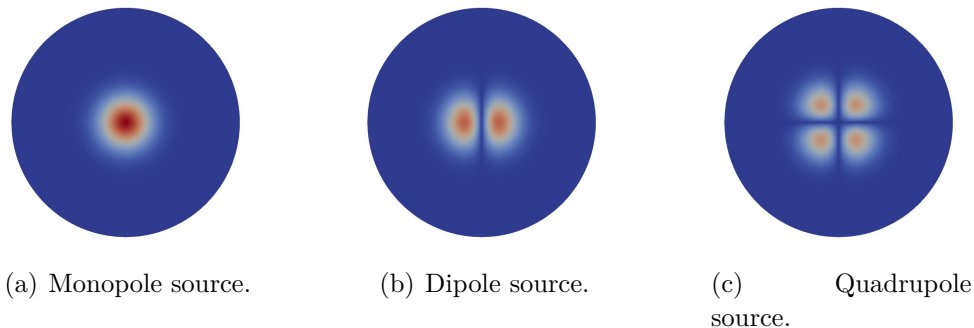


Figure 3.7: Source regions from Fig. 3.8, with different generic sources used for the validation of the interpolation algorithm. Absolute value of the source strength is displayed.

Different source distributions of the wave equation correspond to different free-field radiation patterns. To resolve these sources adequately, there is an upper limit in coarsening the mesh. Therefore, the advantage of a hybrid aeroacoustic workflow is that the source field on the CFD mesh can be kept the same while investigating different resolutions of the CAA grid in the source region. Quantitative plots of the analytic source fields on the CFD mesh are shown in Fig 3.7.

The propagation region does not differ, except in the surrounding area of the source disk, for a smooth transition between the grid of the source region and the propagation region. The complete computation domain consists of a circular source region with a radius of 4.95 m, a propagation region of  $240\text{ m} \times 240\text{ m}$ , and a perfectly matched layer (PML) region with a width of 10 m to account for the free radiation condition (see Fig. 3.8). We performed a time-harmonic simulation at a frequency of  $f_{\text{excite}} = 30\text{ Hz}$  and ambient conditions ( $T = 293.15\text{ K}$ ), resulting in a wavelength of  $\lambda = 11.4\text{ m}$ . Considering the element size inside the propagation region, the mesh resolves the acoustic wave by twenty linear elements per wavelength. All used meshes are unstructured meshes.

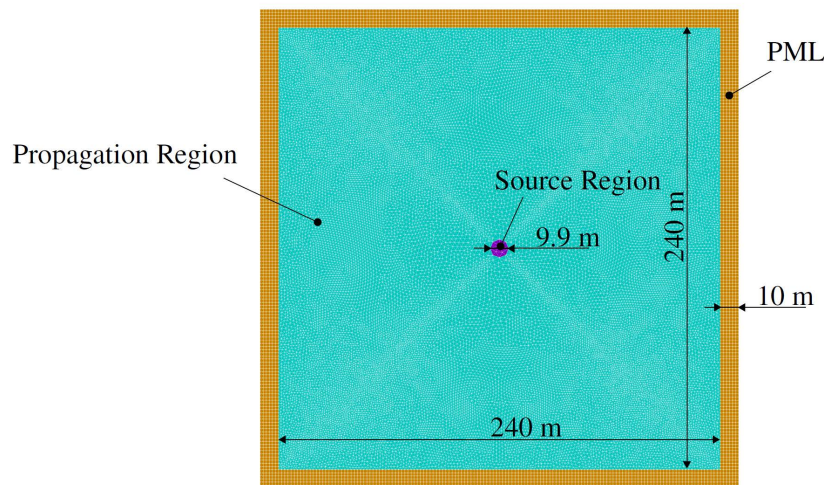


Figure 3.8: Regions and mesh of the CAA simulation.

The propagation domain discretizes the acoustic equations to resolve wave propagation correctly. The cell size of the source mesh is chosen such that it is half of the cell sizes of the finest coarser target mesh and is also used for the reference mesh. The acoustic source fields are prescribed on the source region of the CFD mesh (see Fig. 3.9(a)). Based on this source mesh, the pressure is interpolated on the acoustic target mesh. The interpolated pressure field on the acoustic target mesh is then used as a right-hand side for an acoustic propagation simulation, which is solved in the frequency domain.

For the numerical investigation, different mesh resolutions are used as acoustic target meshes. Figures 3.9(b) and 3.9(c) show the finest coarser and coarsest target mesh. Additionally to the coarser CAA meshes, the effect of finer CAA-meshes (on the radiation) is depicted. The black dashed circle marks the source region from Fig. 3.8. The prescribed right-hand-side values, of this region, are plotted in Fig. 3.7. The different mesh sizes of the source domains used for this verification are listed in Tab. 3.2. The effects on the radiation are discussed below. The last column of this table describes the relation of the element size to the spatial parameter  $\sigma$  of the analytic sources. As the spatial parameter  $\sigma$  represents the size of the source, this column describes the relation between the element and the source size.

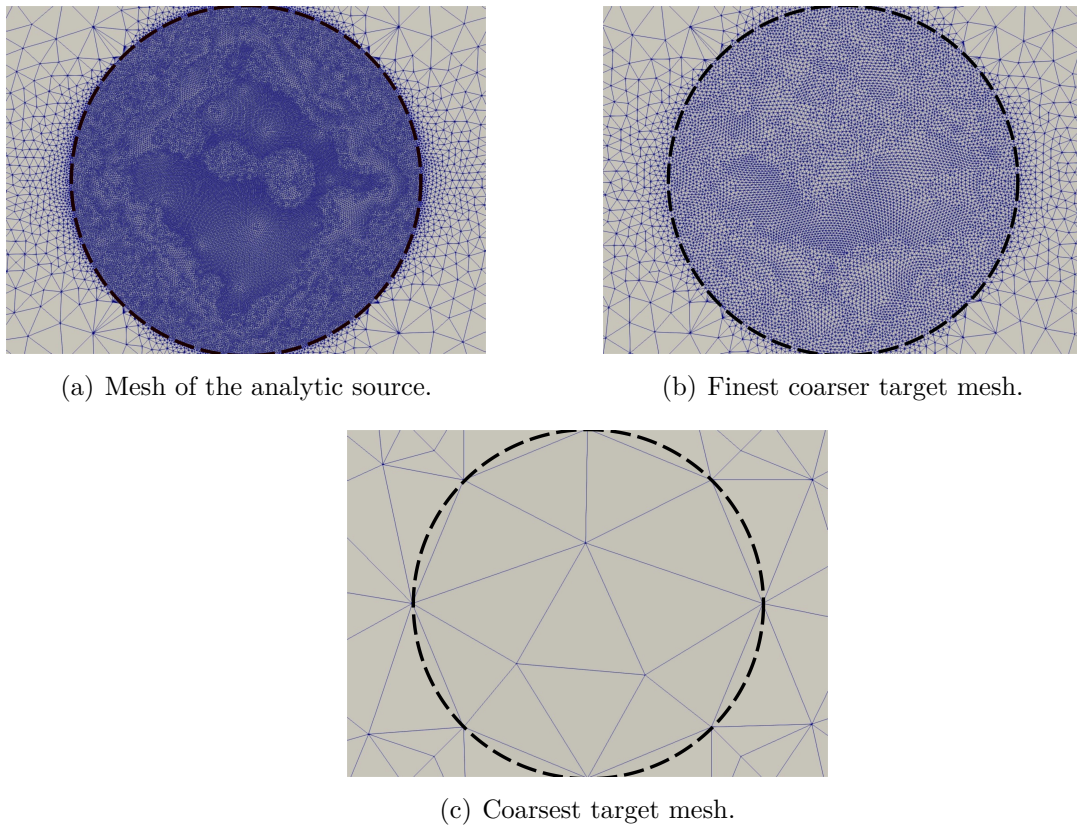


Figure 3.9: Different meshes for the interpolations, with a very fine mesh of the analytic source, and the finest and coarsest target mesh.

Table 3.2: Different meshes used in the source region to investigate the cut-volume cell interpolation.

	Nr. of Cells	Nr. of Nodes	Element size in m	Element size / $\sigma$
Mesh -2	1267140	634815	0.0125	0.01 $\bar{6}$
Mesh -1	305494	153370	0.025	0.0 $\bar{3}$
Reference Mesh	77416	39021	0.05	0.0 $\bar{6}$
Mesh 1	18378	9346	0.1	0.1 $\bar{3}$
Mesh 2	4626	2392	0.2	0.2 $\bar{6}$
Mesh 3	1160	621	0.4	0.5 $\bar{3}$
Mesh 4	292	167	0.8	1.0 $\bar{6}$
Mesh 5	82	52	1.6	2.1 $\bar{3}$
Mesh 6	56	37	2	2.6 $\bar{6}$
Mesh 7	12	11	4	5.3 $\bar{3}$

The evaluation of the acoustic radiation for the three different source fields, is shown in Fig. 3.10 and Fig. 3.11. For each source-setup, for a circular microphone array with a radius of 20 m, the resulting acoustic pressure relative to the maximum evaluated pressure is plotted.

It can be seen, that the acoustic result is almost identical for mesh sizes up to 0.8 m, or to a ratio of the element size to spatial parameter  $\sigma$  of about 1, especially for monopole sources. For larger ratios of mesh size to  $\sigma$ , the radiation patterns are represented correctly; however, the amplitude clearly shows deviations from the real value. The interpolation only fails for the coarsest mesh with a cell size of 4 m. For the setups where the CAA-meshes are finer than the CFD-mesh, the deviations are very similar to the finest coarser mesh, which can be verified in Tab. 3.3. From these results, it can be seen that the cut-volume cell approach can be applied to a large range of acoustic mesh sizes. The upper limit of the acoustic mesh size is given by the source size, which is the spatial parameter  $\sigma$  in this verification example.

The results of the cell-centroid approach are almost identical to the cut-volume cell, for all considered element size to  $\sigma$  ratios, as Tab. 3.3 confirms.

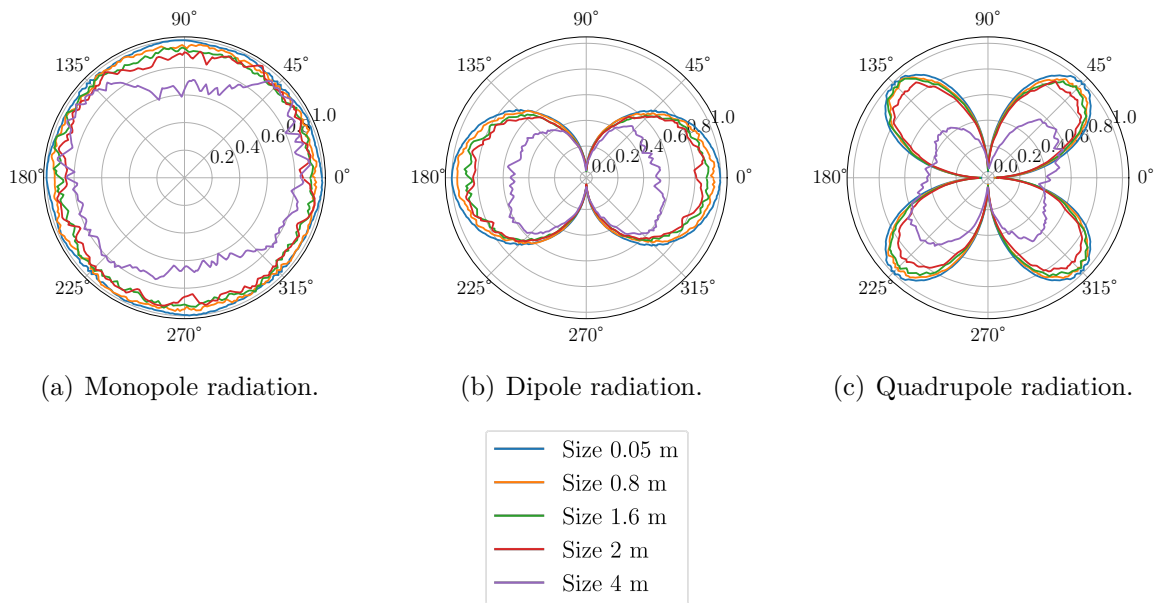


Figure 3.10: Results of the coarsest discretizations for the generic sources (cut-volume cell interpolation).

To conclude for compact aeroacoustic sources, it is essential that the source is at least discretized by one element regarding the decay parameter  $\sigma$ . Overall, this discretization criterion slightly depends on the polar source characteristic (see Tab. 3.3). However, the interpolation error of the dipole and quadrupole source shapes are higher, using the same discretization. Following these rules, acoustic meshes can be designed inside the aeroacoustic source region. This estimation can be incorporated into a post-processing

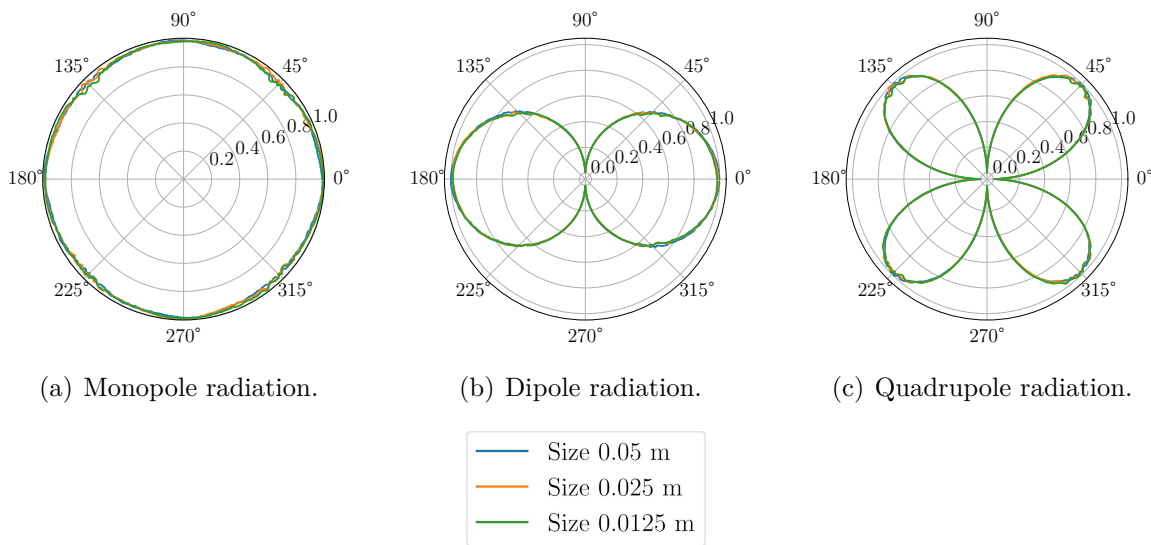


Figure 3.11: Results of the fine discretizations for the generic sources (cut-volume cell interpolation).

routine of the CFD simulation that calculates the values for the source distribution  $\sigma$ .

Table 3.3: Averaged deviations in the acoustic results between reference mesh and finer or coarser meshes (concerning the reference mesh in percent), using cell-centroid and cut-volume cell interpolation.

	cell-centroid interpolation			cut-volume cell interpolation		
	Monopole	Dipole	Quadrupole	Monopole	Dipole	Quadrupole
Mesh -2	-0.45	1.74	0.12	-0.45	1.75	0.13
Mesh -1	-0.36	1.84	0.30	-0.36	1.84	0.29
Mesh 1	-0.23	1.27	0.46	-0.23	1.27	0.46
Mesh 2	-0.21	1.55	0.73	-0.20	1.56	0.73
Mesh 3	0.56	2.53	2.25	0.56	2.53	2.25
Mesh 4	2.58	5.32	4.69	2.58	5.33	4.69
Mesh 5	6.03	12.58	8.61	6.04	12.60	8.62
Mesh 6	8.04	12.98	14.39	8.05	12.98	14.39
Mesh 7	27.21	47.63	70.58	27.25	47.67	70.67

### 3.5 Grid convergence analysis

The influence of the discretization on the result uncertainty is quantified by a grid convergence study. Thereby, the convergence properties and the estimated error of the computational grid with respect to the (in most cases unavailable) analytical continuous solution are of main interest.

In order to deal with these objectives, the grid convergence index (GCI) is introduced as a simple method for uniform reporting of grid-convergence studies without any restriction to integer refinement. The GCI is based on generalized Richardson Extrapolation involving a comparison of discrete solutions at two different grid spacings. [26]

The Richardson Extrapolation of the physical quantity  $L$

$$L^{\text{ext}} \approx L^{\text{fine}} + \frac{L^{\text{coarse}} - L^{\text{fine}}}{1 - r^{p_L}} \quad (3.22)$$

is used to estimate the quantity  $L^{\text{ext}}$  at infinite grid resolution from 2 different discretizations  $L^{\text{fine}}$  and  $L^{\text{coarse}}$  as well as the method's order of convergence  $p_L$ .  $r = h^{\text{coarse}}/h^{\text{fine}}$  is the refinement ratio which is the quotient of the element size  $h$  of the 2 grids. In order to estimate both quantities, at least 3 grids are necessary to perform the grid convergence study. In case of 3 grids, the 2 unknowns can be computed directly from the extrapolation (3.22) for grid 1 and 2 respectively 2 and 3. With  $n \geq 4$  grids available, a minimization problem can be formulated by minimizing

$$\min_{L^{\text{ext}}, p_L} \sum_{i=1}^{n-1} \left[ L_i + \frac{L_{i+1} - L_i}{1 - r_i^{p_L}} - L^{\text{ext}} \right]^2 \quad (3.23)$$

where  $L_i$  are the result quantities for the  $n$  grids, which are ordered in descending refinement and  $r_i = h_{i+1}/h_i$ .

The Grid convergence index is then defined by

$$\begin{aligned} \text{GCI}_i^{\text{fine}} &= F_s \left| \frac{\varepsilon_{L,i}}{1 - r_i^{p_L}} \right| \\ \text{GCI}_i^{\text{coarse}} &= F_s \left| \frac{r_i^{p_L} \varepsilon_{L,i}}{1 - r_i^{p_L}} \right| \end{aligned} \quad (3.24)$$

with the relative deviation

$$\varepsilon_{L,i} = \frac{L_{i+1} - L_i}{L_i} \quad (3.25)$$

and a safety factor  $F_s = 1.25$  (recommendation according to [26] and [27]). From (3.24) follows that  $\text{GCI}_i^{\text{fine}} \approx \text{GCI}_{i-1}^{\text{coarse}}$  if the solutions are converging suitably. As the GCI calculates from the deviation of the simulation result to the estimated true solution, the GCI can be interpreted as an error bandwidth in a statistical sense [26].



Die approbierte gedruckte Originalversion dieser Diplomarbeit ist an der TU Wien Bibliothek verfügbar.  
The approved original version of this thesis is available in print at TU Wien Bibliothek.

# Chapter 4

## Application - Human Phonation

Human communication is based heavily on a perfectly working voice production. Any form of dysphonia can therefore limit the ability to communicate by speech and express emotions like laughing or crying. In order to be able to treat malfunctions of the sound generating process a simulation model is needed to fully understand the ongoing mechanisms. In a cooperation between Universitätsklinikum Erlangen (Department for Phoniatics and Pedaudiology) and TU Wien, the joint project *Numerical computation of the human voice source* aims to develop a simulation tool to predict the voice depending on various parameters including the geometry of the vocal tract. In a hybrid aeroacoustic simulation approach, the derivation of the source terms becomes of major importance. A source term analysis can give conclusion what the main sound production mechanisms are as well as where they occur and can help to reveal terms that can be neglected in order to improve numerical efficiency.

In this chapter, the human voice production mechanism investigated regarding the simulation to an experimental setup that was used in [28]. The following sections presents the findings from [5], additional analysis of the present sources and explains the used methodology in detail.

### 4.1 Simulation Model

For a source term analysis, several factors have to be considered for the selection of the simulation model. First of all, the model should represent the investigated problem. However, to gain useful results from the analysis, the functionality of the model should be verified, or ideally validated by measurement data. Furthermore, to visualize the sources in an appropriate resolution, the source term analysis requires a finer mesh than what would be sufficient fine for just the propagation simulation. For the following analysis the simulation model and methodology is therefore based on the workflow presented in [28].

### 4.1.1 Geometry

The geometry of the simulation model is derived from the experimental setup of a synthetic larynx model developed by Kniesburgers *et al.* [29]. Figure 4.1 shows an illustration of the experimental setup. It consists of a rectangular flow channel with a cross-section of 18 mm × 15 mm, the vocal folds (VF), which are made of silicone, and rigid ventricular or false vocal folds (fVF) [29] [30]. The VF divide the flow channel into subglottal and

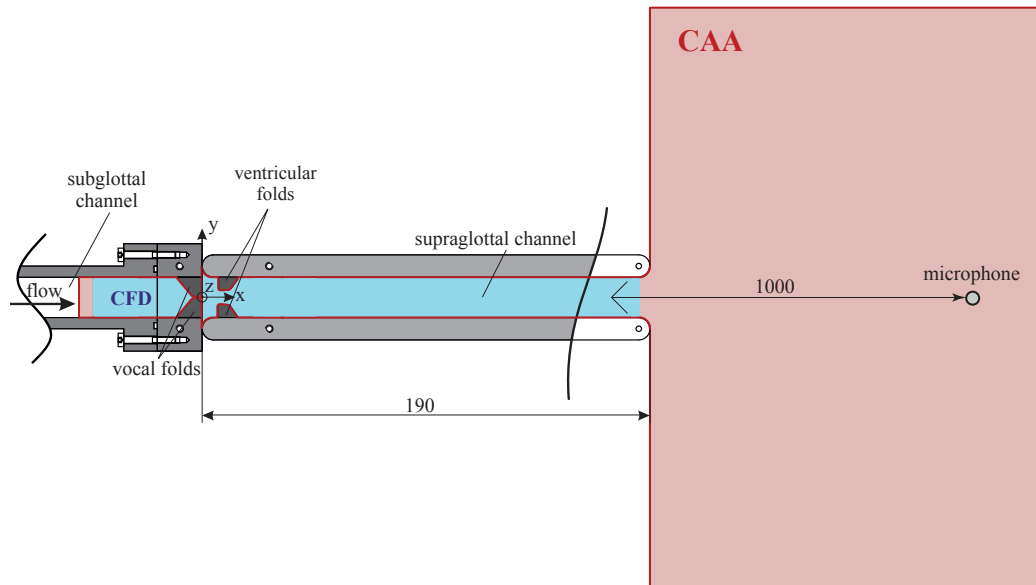


Figure 4.1: Illustration of the larynx model extracted from [29]: Test channel, VF, fVF, and a propagation domain used in the CAA computations (Red highlighted area). CFD domain highlighted in blue. All dimensions are in mm. [28]

supraglottal channels of similar length of 190 mm. The subglottal channel however is truncated in the following simulations to improve computational efficiency. The supraglottal channel is realized by 2 aluminum plates with a thickness of 10 mm on top and bottom, a 5 mm-thick glass plate in front, and a 10 mm-thick plastic plate (polymethylmethacrylat) on the backside. The geometry of the vocal folds replicates the M5 model introduced by [31] and [32].

### 4.1.2 Computational fluid dynamics (CFD)

The computational domain for all CFD computations is highlighted blue in figure 4.1. It covers all parts of the experimental setup, where a comparably high flow speed is expected. The incompressible flow equations were solved with the commercial software package *Star-CCM+* (Siemens PLM Software, Plano, TX/USA) with a cell-centered non-staggered grid, while the turbulences were modeled by LES with a WALE (wall-adapting

local eddy-viscosity) [33] subgrid scale model [34]. The symmetrical motion of the vocal folds was prescribed as a moving mesh boundary condition instead of incorporating the fluid-structure interaction. Therefore, the glottal area waveform (GAW) was used, which was extracted from the experimental model by measuring the flow-induced motion of the silicone vocal folds. Figure 4.2 shows the GAW of the VF for one oscillation cycle (oscillation frequency  $f = 148$  Hz). All channel walls are modeled by no-slip-no-injection boundary conditions. At the inlet and outlet boundaries the fluid pressure was prescribed to 2450 Pa and 0 Pa respectively [34].

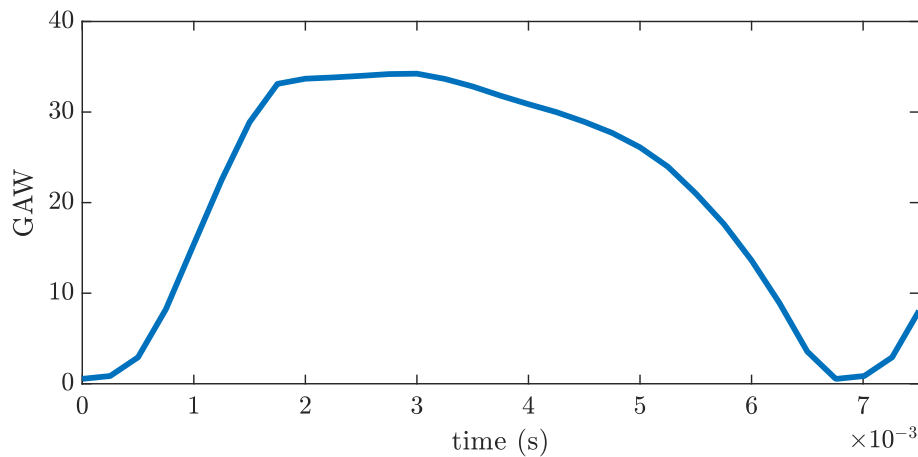


Figure 4.2: Glottal area waveform (GAW) for one cycle of the VF motion.

### 4.1.3 Computational aeroacoustics (CAA)

The computational domain for any aeroacoustic propagation simulations is highlighted red in figure 4.1. Following the hybrid aeroacoustic approach, a different mesh is used for the CAA computations. Figure 4.3 shows the CAA mesh, which was inherited from [28]. In addition to the regions included in the CFD simulation, the CAA also covers the sound propagation to the microphones, which are located in a distance of 1 m to the end of the supraglottal channel as depicted in figure 4.1. Therefore, a cuboid-shaped propagation domain is used. Furthermore, a two-layer-thick perfectly matched layer (PML - [35]) region is attached on the boundary, where the propagation region is truncated, to sufficiently ensure the open domain property [28]. The inlet boundary condition is realized by an absorbing boundary condition (ABC), as it ensures sufficient absorbing for the almost plane waves, that are arriving and is computationally less expensive in comparison to a PML. All other boundaries, including the bottom plane of the propagation domain, are modeled as sound hard. The larynx region and vocal tract are meshed by approximately 127,500 tetrahedral elements with a maximum element size of 4.3 mm. In contrast to that, the propagation and PML regions are meshed with hexahedral elements.

The aeroacoustic sources are calculated following the previously explained PCWE analogy (see chapter 2.3.2). Therefore the flow field is interpolated to the CAA grid using the cut-volume cell interpolation technique (see chapter 3.4.2) and the incompressible fluid density is set to  $\bar{\rho} = 1.138 \text{ kg/m}^3$  while the speed of sound is given by  $c = 343.4 \text{ m/s}$ . The PCWE, that describe the aeroacoustic wave propagation, are then solved by a finite element approach (see chapter 3.1). This presented framework has been implemented in the in-house finite element solver *CFS++* ([22]).

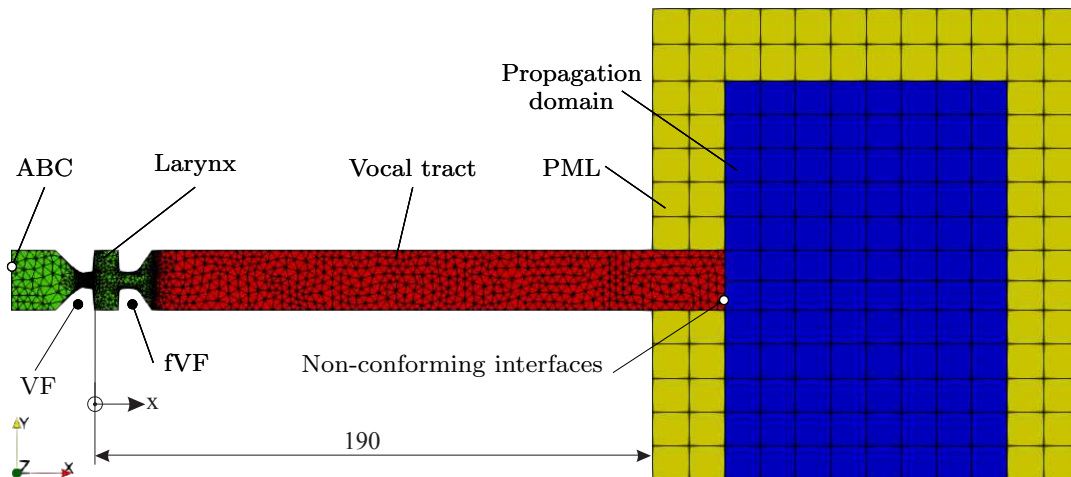


Figure 4.3: Simulation setup for the aeroacoustic simulation. [28]

## 4.2 Aeroacoustic source term analysis

Before the actual aeroacoustic sound propagation simulation, a source term analysis is performed in the following section. This type of analysis gives deeper insight in the sound generating mechanisms and makes it possible to determine dominant frequencies and important regions. Therefore the flow quantities are used, to derive all components of the source terms following the aeroacoustic analogies. Thereafter, all aeroacoustic source terms and their components are visualized and discussed both in time- and frequency domain. All quantities are visualized on the CFD grid directly to mitigate any possible interpolation error. It may also be noted, that any interpolated field quantity, that was interpolated using one of the previously described conservative interpolation schemes yields a non-representative field for source term analysis. This is due to weighting each cell value by its cell's volume which makes an interpretation of the resulting field impossible due to the varying cell sizes. However, using some interpolation scheme that conserves the absolute values of the field quantities like Nearest-Neighbor-interpolation instead introduces a significant error due to the intended large deviations between the flow and the acoustic grid in the hybrid CAA approach. Having obtained the finely resolved source term, a field fast Fourier transformation (field FFT) is performed in

*MATLAB*<sup>®</sup>, which is an FFT of the time signal of every nodal load on the computational grid. For the following visualizations in the frequency domain, a time harmonic visualization of the oscillation mode of the corresponding frequency is depicted.

For the visualizations in the time domain, 4 representative time-steps during one VF oscillation are selected:

1. the VFs are closed (minimum opening),
2. the VFs are opening,
3. the VFs are open (maximum opening),
4. and the VFs are closing.

In figure 4.4, the according VF opening states again using the glottal area waveform (GAW) are indicated.

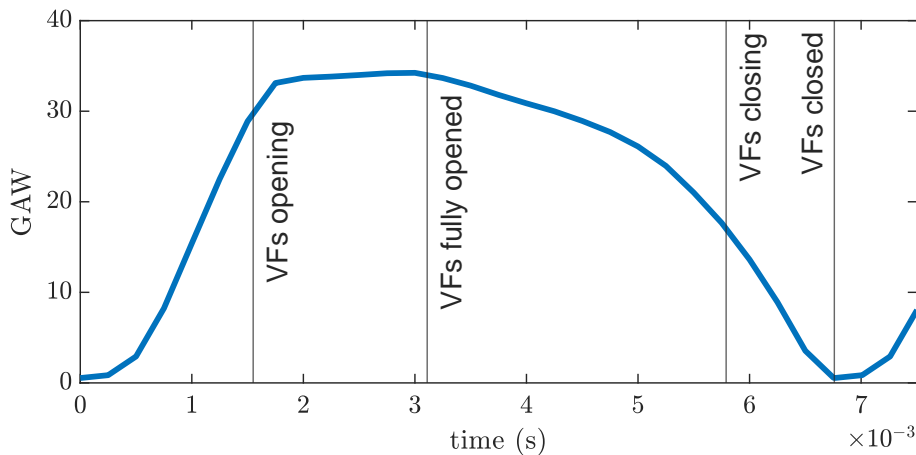


Figure 4.4: Glottal area waveform (GAW) for one cycle of the VF motion with marked characteristic timesteps, which are used for the source term analysis in the time domain.

Secondly, in the frequency domain, besides the base frequency  $f_0$ , a range of higher harmonics as well as a non-harmonic frequency is evaluated:

- $f_0 = 148\text{Hz}$  (VF's base oscillation frequency),
- $2f_0, 7f_0, 10f_0, 30f_0$  (VF's higher harmonics),
- $f = 3589\text{Hz}$  (VF's non-harmonic).

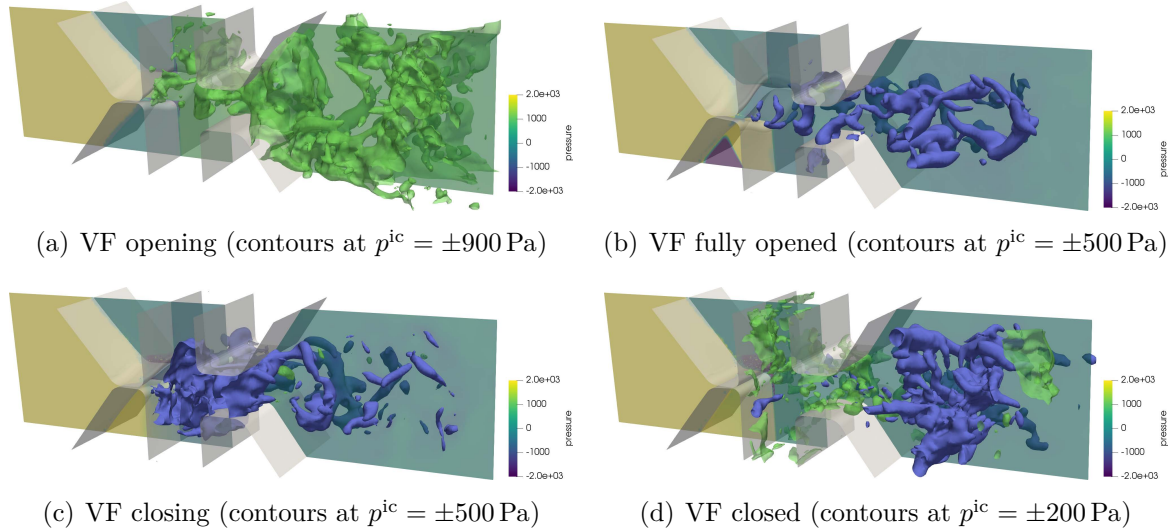


Figure 4.5: Fluid pressure visualization during a full VF cycle.

### 4.2.1 Flow quantities

To be able to interpret the source generating mechanisms, and also to check whether the obtained source field is realistic, we need to take a look at the flow. Therefore, Figure 4.5 visualizes the fluid pressure obtained from the CFD simulation at the 4 characteristic timesteps. At each timestep the flow pressure distribution in the central plane as well as contour planes are depicted. In the first plot the flow is accelerated during the opening of the VFs. Highly turbulent structures, which are generated by the flow pressure jump, that happens with the opening event, are blown downstream. This continues until the VFs are fully opened (Fig. 4.5(b)) and the flow pressure profile shows the shear layers of the glottal jet. Once the VFs are starting to close, the glottal gap becomes a bigger and bigger obstacle for the flow. As a result the fluid decelerates, which is indicated by the highly negative flow pressure profile originating from the glottal gap. Additionally, rather strong fluctuations are caused by the ever increasing flow constriction. In the case of a fully closed glottal gap, the flow is cut off and Fig. 4.5(d) shows decaying flow structures in the otherwise resting fluid, which start to curl as there is no more driving force.

In the frequency domain, time independent observations can be made. Figure 4.6 shows the oscillation mode of 5 corresponding frequencies. For the base oscillation frequency of the vocal folds (Fig. 4.6(a)), a global and monotone pressure drop can be observed in downstream direction.

Figure 4.7 shows the flow pressure and velocity profile at the 4 characteristic time instances along the downstream direction, once at the center line and once at a line, that is located in the side area of the glottal gap in a distance 2.5 mm from the center line. As a result of the boundary conditions of the CFD simulation, the flow pressure values are fixed at the inlet and the outlet. In the subglottal channel, the flow pressure increases

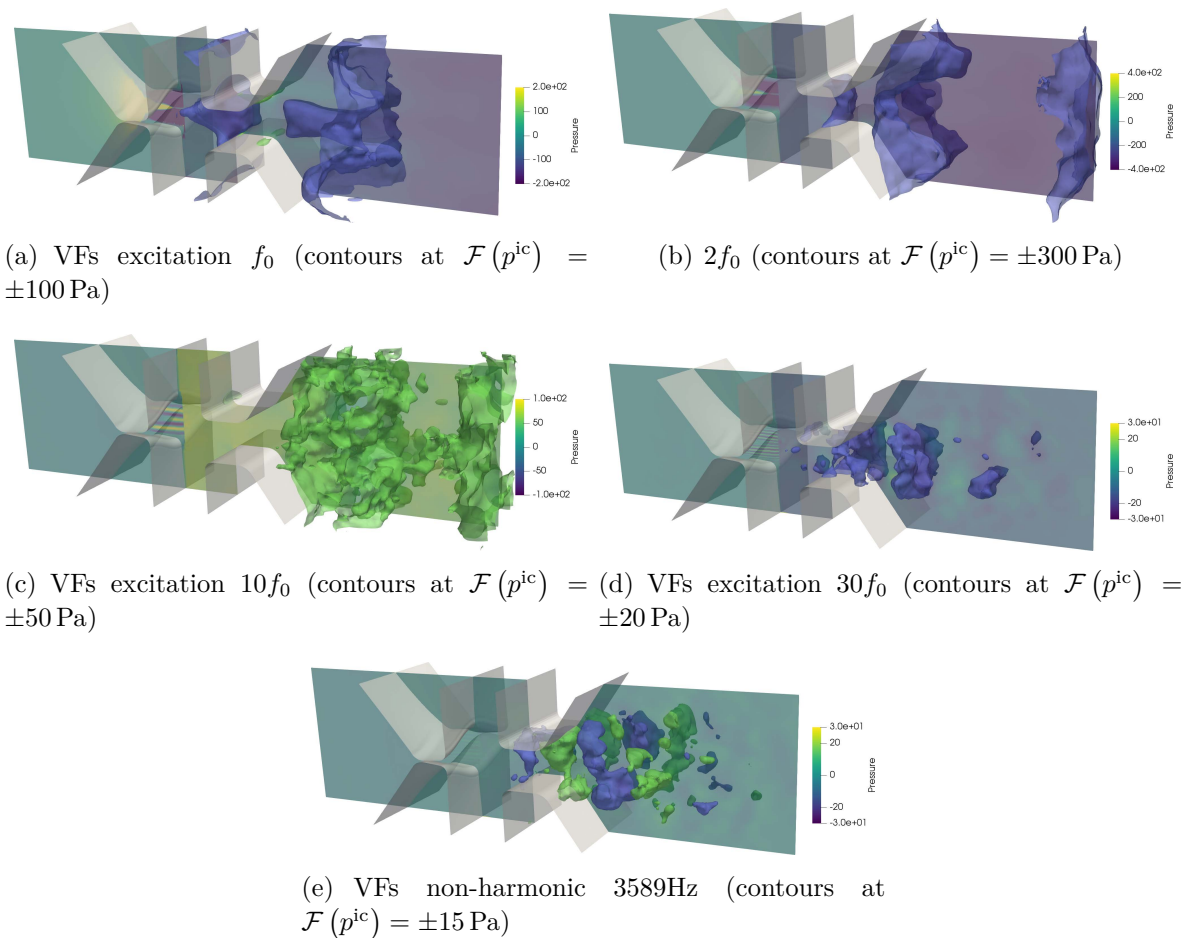


Figure 4.6: Fluid pressure visualization for several frequencies.

linearly towards the vocal folds, that are located at  $x \approx 0.02$  m. In the glottal gap, a big pressure drop occurs. The pressure and velocity fluctuations, that are caused by this jump, are the main sound sources. Downstream the VFs, the flow pressure and velocity decay towards the outlet boundary. This verifies the more or less monotone pressure drop observed for the base oscillation frequency in Fig. 4.6(a). The pressure drop is large for a narrow glottal gap which also gives a large velocity change. As a consequence, this causes the time derivative of the incompressible flow pressure to be significant in a large region around the glottal gap.

For higher harmonics (Fig. 4.6(b) and 4.6(c)) the pressure fluctuations, that originate in the glottal gap and propagate downstream can be observed. For high frequencies both, multiples of the harmonic frequency (Fig. 4.6(d)) and non-harmonic frequencies (Fig. 4.6(e)), show the propagating vortical structures.

Figure 4.8 depicts the mean velocity magnitude profile in a central plane as well as several contours that indicate the shear layer zones of the mean flow. One can observe the glottal jet, within the convective source terms are of significance.

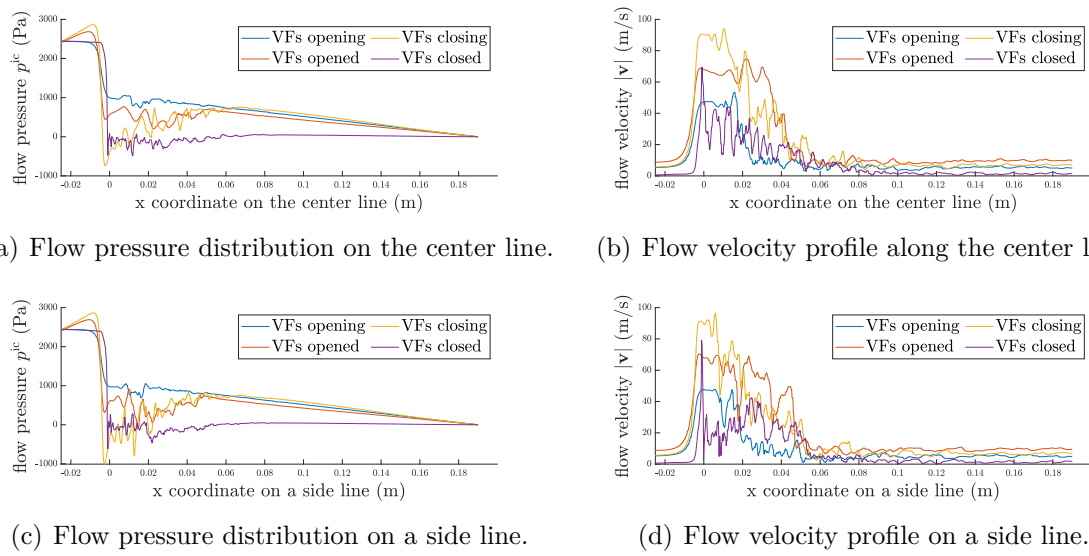


Figure 4.7: Flow pressure and velocity over the computational domain

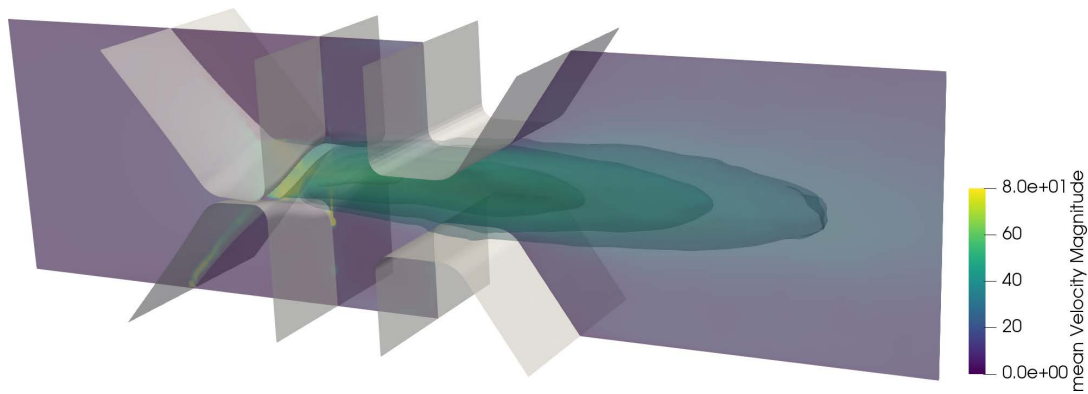


Figure 4.8: Fluid mean velocity field magnitude  $|\bar{\mathbf{v}}|$  and glottal jet visualized by contours at  $|\bar{\mathbf{v}}| = 30, 40, 50, 60 \text{ m s}^{-1}$  inside the glottal region.

In terms of turbulent structures, the turbulent kinetic energy (TKE)  $k$  is a measure of the mean kinetic energy, that can be associated to vortices in the turbulent flow. Figure 4.9 depicts the TKE during a full cycle of the VFs. Again we can observe the contour planes visualizing the glottal jet, which indicates that inside the glottal jet, most of the turbulent structures are located, as stated in the pressure analysis before. This overlap with the regions of high mean velocity is quite intuitive because high velocities result in a high Reynold's number which characterizes turbulent flow. As the TKE is an averaged quantity, it looks quite similar for all timesteps.

Taking a closer look at the flow velocity, Fig. 4.10 gives illustration of the velocity magnitude in the frequency domain. Just like for the flow pressure, for the VF oscillation frequency, the velocity changes globally and propagates downstream. However, Fig. 4.10(b), 4.10(c) and 4.10(d) indicate, that the flow velocity is strongly connected to

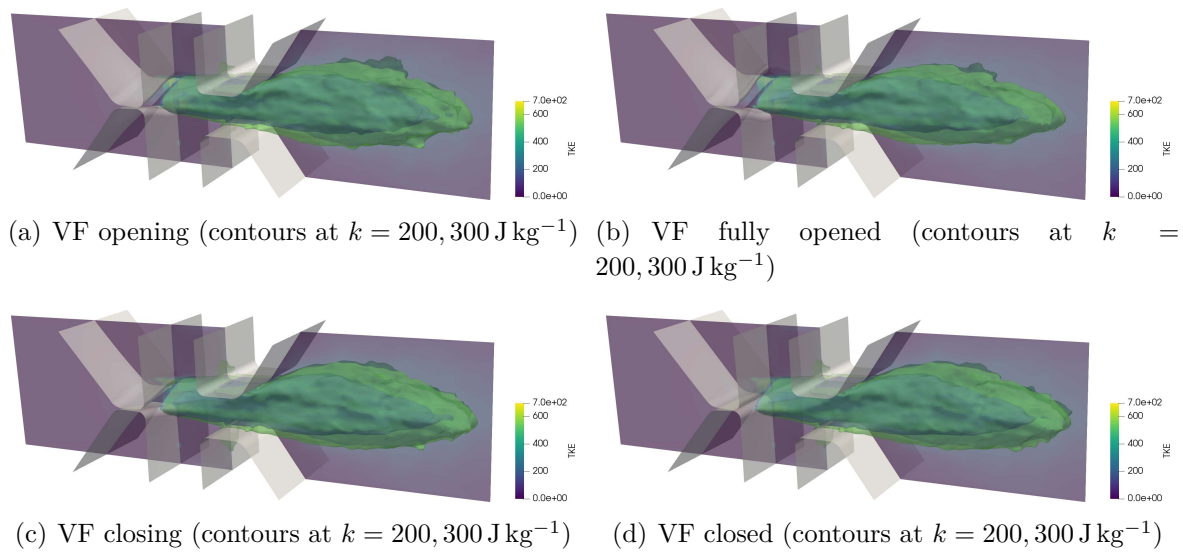


Figure 4.9: Turbulent kinetic energy (TKE)  $k$  during a full VF cycle.

the base oscillation frequency and the velocity profile for higher harmonics doesn't differ significantly from one at a non-harmonic frequency (compare Fig. 4.10(e)). The contour planes become small dots scattered around the whole computational domain, visualizing the turbulent structures inside the flow.

Figure 4.11 shows the incompressible flow pressure gradient magnitude in the time domain. As the flow pressure was discussed previously, many of the following observations are connected to the pressure distribution. While the VFs are opening (Fig. 4.11(a)) and turbulent structures are evolving, the gradient magnitude is rather low in all areas except the highly turbulent regions close to the VFs. Thereafter, the glottal jet flow is visible with a high gradient magnitude inside the jet region caused by turbulent structures, that are moving downstream. This process continues, while the VFs are closing. The area in which a large gradient magnitude is present enlarges because of the fluctuations caused by the decelerating flow. Once the VFs are fully closed, the remaining vortical structures generate the pressure gradient, that is visible in Fig. 4.11(d), in the otherwise resting fluid.

In the frequency domain, Fig. 4.12 depicts the oscillation mode of the incompressible flow pressure magnitude  $|\nabla p^{\text{ic}}|$ . The main observation, made by visually comparing all 5 plots, is the dominance of the VF oscillation frequency. All other oscillation modes are smaller by more than a factor 10. Figure 4.12(a) shows the oscillation mode for the vocal fold oscillation frequency. The time-harmonically visualized flow pressure gradient seems to not change sign throughout the plotted region in respect to this frequency, indicating an in-phase oscillation in the whole domain. This behavior is most likely due to the global pressure variations that were discussed previously. In contrast, the oscillation mode at higher harmonic frequencies is of similar magnitude as the oscillation mode at non-harmonic frequencies.

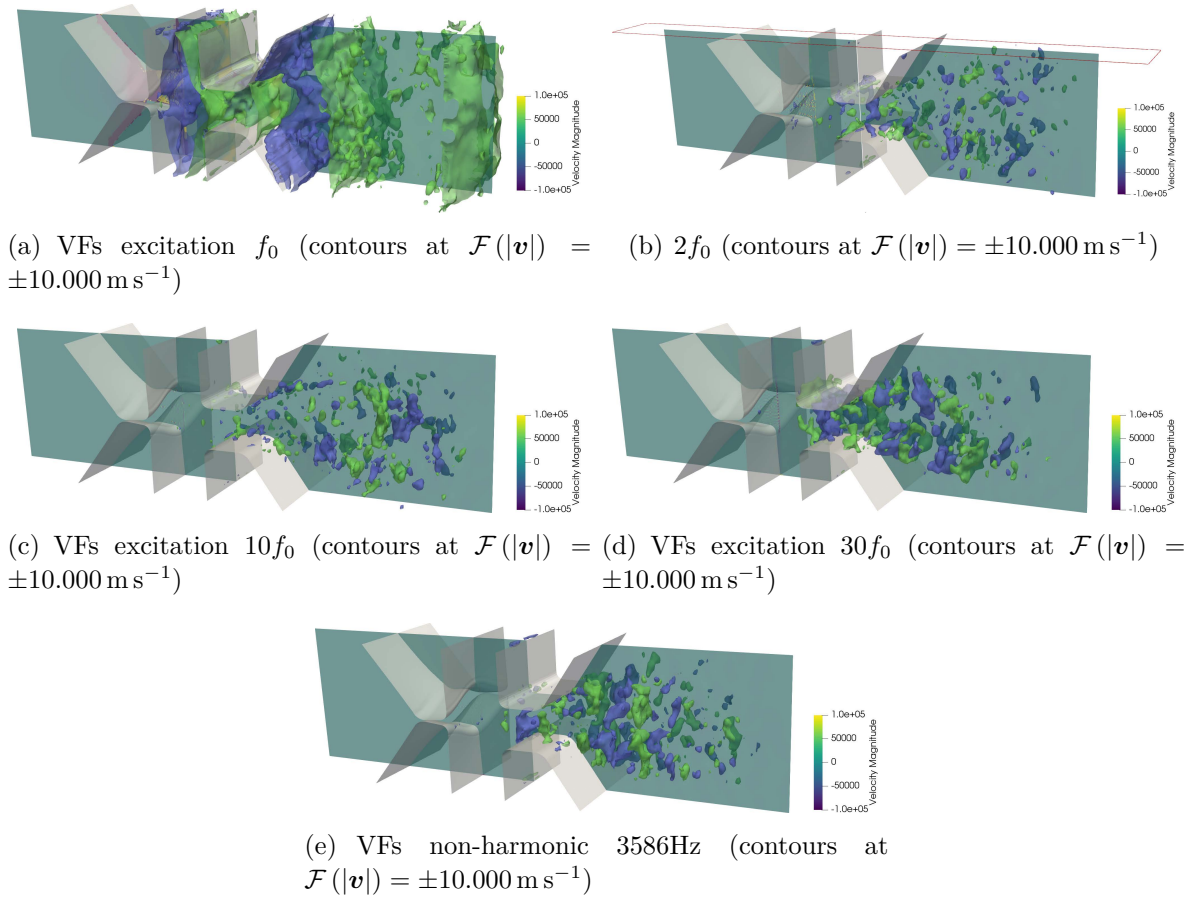
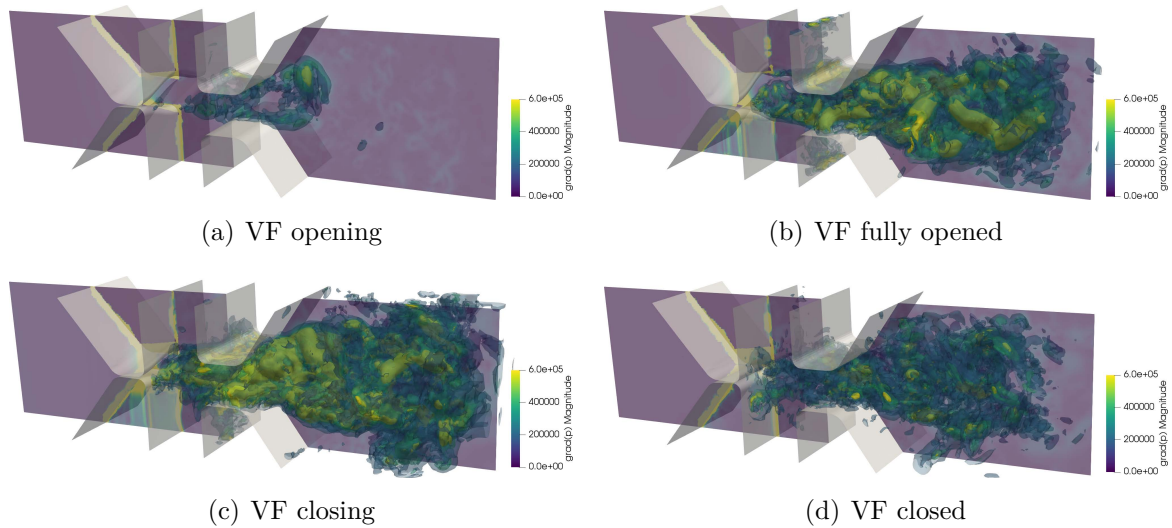


Figure 4.10: Flow velocity visualization for several frequencies.

Figure 4.11: Flow pressure gradient field magnitude  $|\nabla p^{ic}|$  visualized by contours at  $|\nabla p^{ic}| = 2 \cdot 10^5, 4 \cdot 10^5, 6 \cdot 10^5 \text{ Pa m}^{-1}$ .

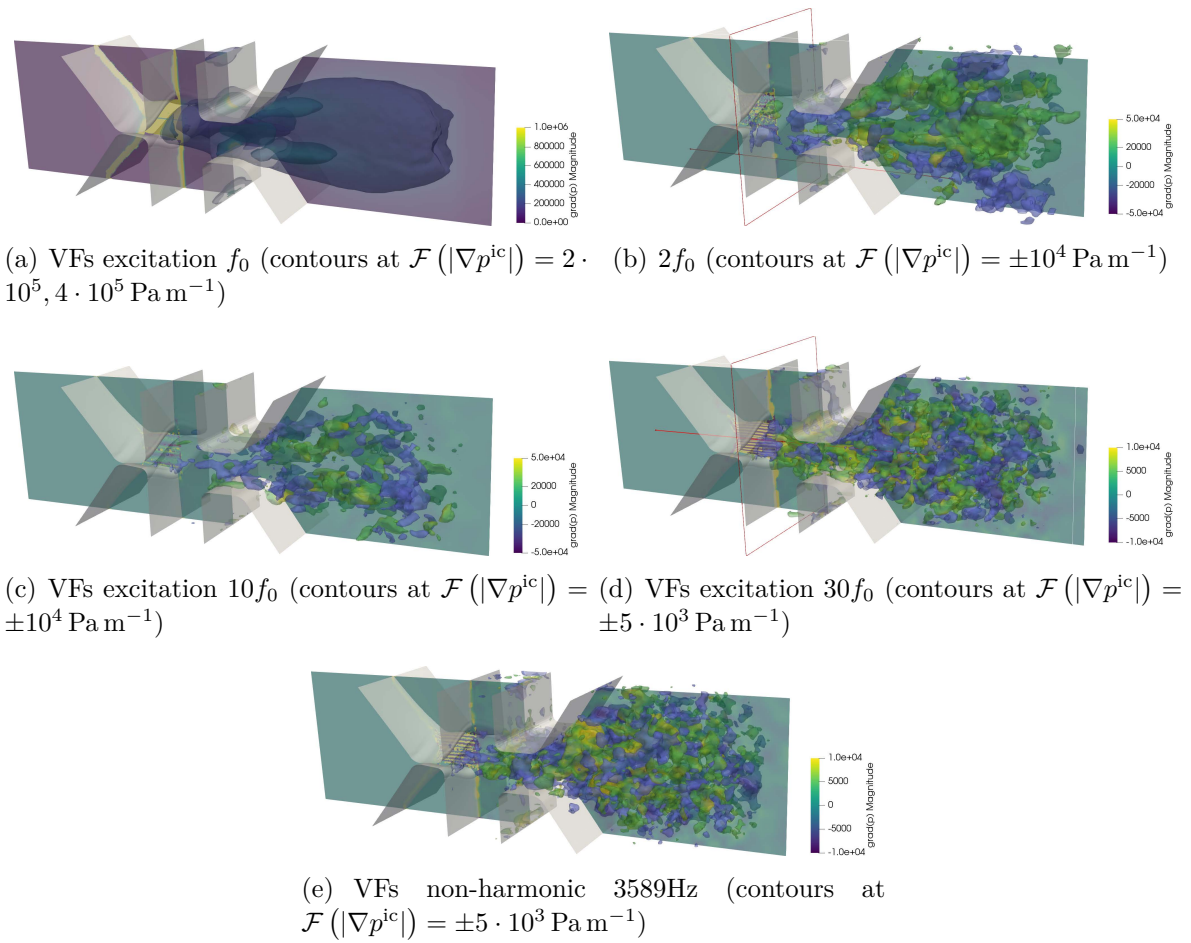


Figure 4.12: Flow pressure gradient field magnitude  $|\nabla p^{\text{ic}}|$  visualization for several frequencies.

## 4.2.2 Aeroacoustic sources

Having analyzed the flow we can now take a look on the components of the aeroacoustic sources for the PCWE and also the perturbed compressible equations (PCE) [17]. In contrast to the PCWE, the convective part of the PCE source is calculated by

$$-\frac{1}{\rho_0 c_0^2} \mathbf{v} \cdot \nabla p^{\text{ic}} \quad (4.1)$$

using the instantaneous incompressible velocity  $\mathbf{v}$ , instead of the incompressible mean velocity  $\bar{\mathbf{v}}$  used in Eq. (2.50). The factor  $1/\rho_0 c_0^2$  is omitted for the following sections as it is globally constant.

Figure 4.13 shows the convective part of the source term belonging to the perturbed compressible equations (PCE) in the time domain, while Fig. 4.14 shows the convective part of the PCWE source term. Visually, both convective source terms look similar although some differences can be noted during the four cycle phases in the time domain.

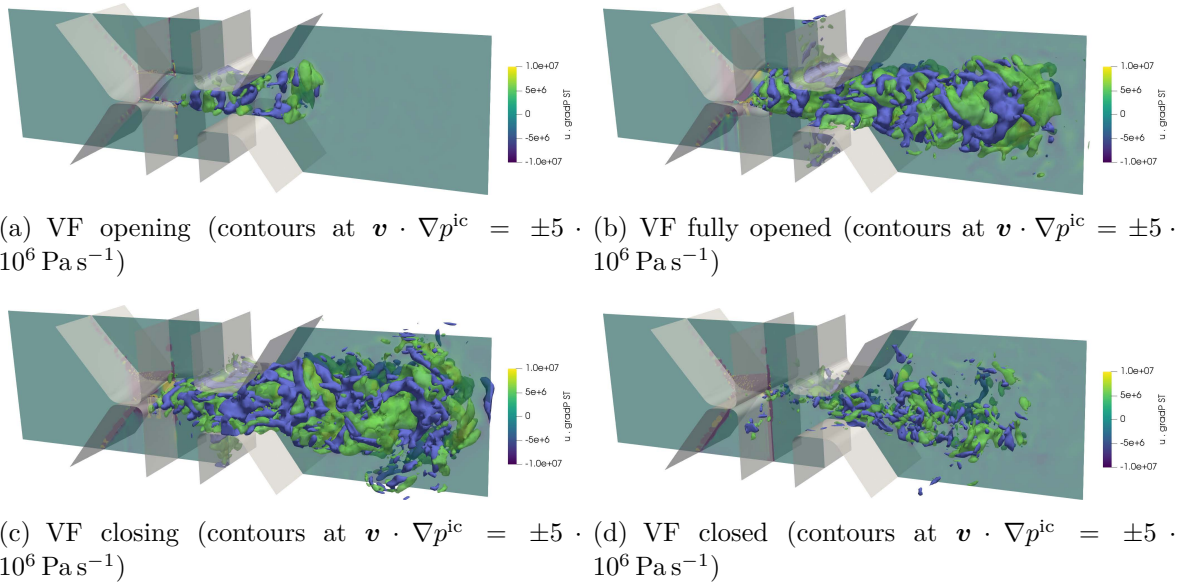


Figure 4.13: Convective part of the source term  $\mathbf{v} \cdot \nabla p^{\text{ic}}$  as it is present in the perturbed compressible equations during a full cycle.

While the VFs are opening and closed, the mean pressure convection is larger in its spatial extend during opening and closed VFs since the mean velocity is larger than the instantaneous velocity  $|\bar{\mathbf{v}}| > |\mathbf{v}|$ . On the other hand, the instantaneous pressure convection is larger due to  $|\bar{\mathbf{v}}| < |\mathbf{v}|$ , when the VFs are fully opened and closing.

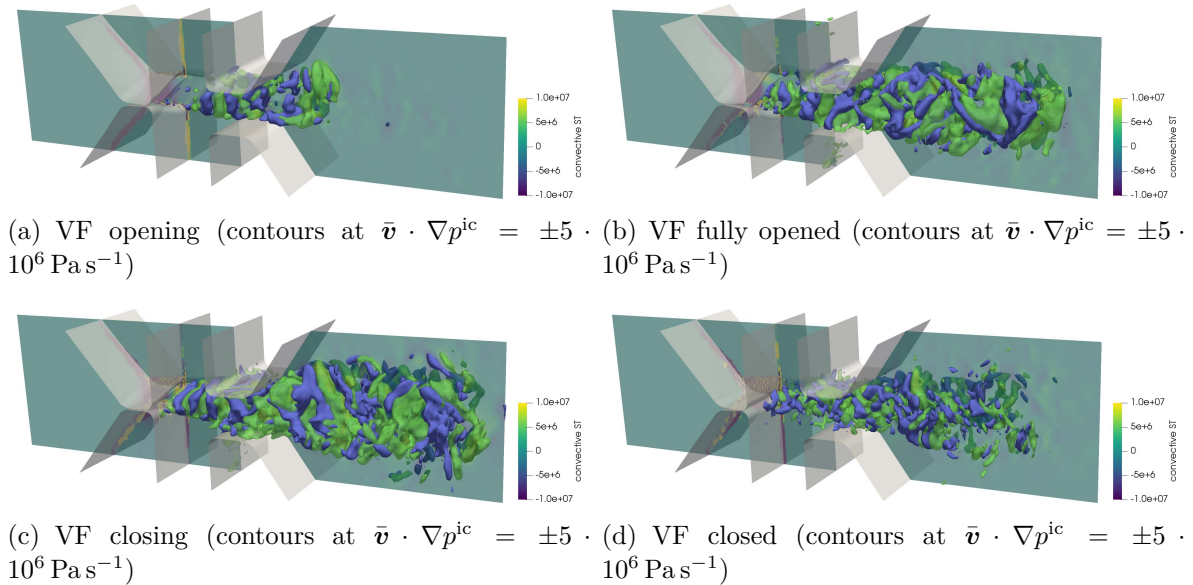


Figure 4.14: Convective part of the source term  $\bar{\mathbf{v}} \cdot \nabla p^{\text{ic}}$  as it is present in the PCWE formulation during a full cycle.

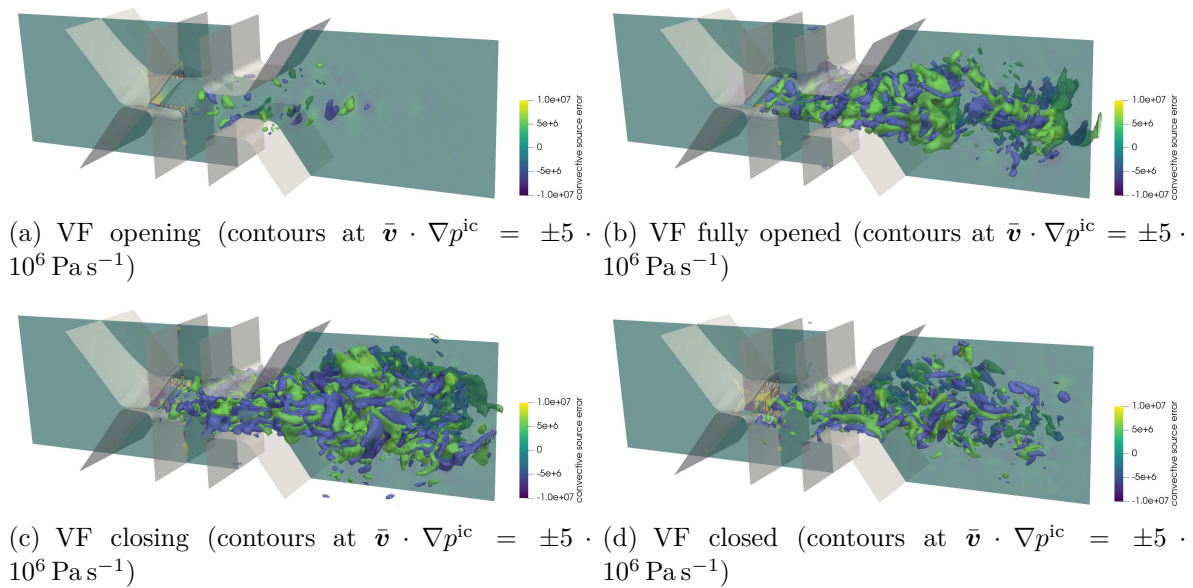


Figure 4.15: Convective part of the source term  $\bar{\mathbf{v}} \cdot \nabla p^{\text{ic}}$  as it is present in the PCWE formulation during a full cycle.

The source error

$$e = \mathbf{v}' \cdot \nabla p^{\text{ic}} = \mathbf{v} \cdot \nabla p^{\text{ic}} - \bar{\mathbf{v}} \cdot \nabla p^{\text{ic}}. \quad (4.2)$$

is depicted in Fig. 4.15 for a full cycle. At all 4 characteristic timesteps, the contour planes form a hose-like structure, which indicates that the main deviations occur outside the center of the vocal tract.

Overall, the convective source term can be interpreted as some sort of flow blending as it is calculated by a projection of the pressure gradient onto the velocity. This results in large contributions in regions with high flow velocities, which is mainly between the VFs inside the glottal jet region (see Fig. 4.8). During the opening of the VFs, the contours show a growing mushroom-like structure that indicates the pressure fluctuations. This continues, while the VFs are fully opened and the structure shows these pressure fluctuations all over the glottal jet region. Once the VFs start closing, the convective sources are still growing and widening into the vocal tract until the required driving energy is missing and the sources decay with the vortices when the VFs are closed completely.

The difference of these two convective source term becomes more apparent in the frequency domain. Figures 4.16 and 4.17 show the oscillation modes at several characteristic frequencies for the PCE and PCWE convective source term, respectively. While the PCE convective source term looked similar to the PCWE convective source term in the time domain, this is not the case at any visualized frequency. While the contour planes are mainly restricted to the glottal jet for the PCWE source term, the oscillation mode contours for the PCE source term show rather strong fluctuations throughout the whole

vocal tract. It may be noted, that the source term still peaks inside the glottal jet region, which is not visualized at this point but intuitive, following from the time domain plots.

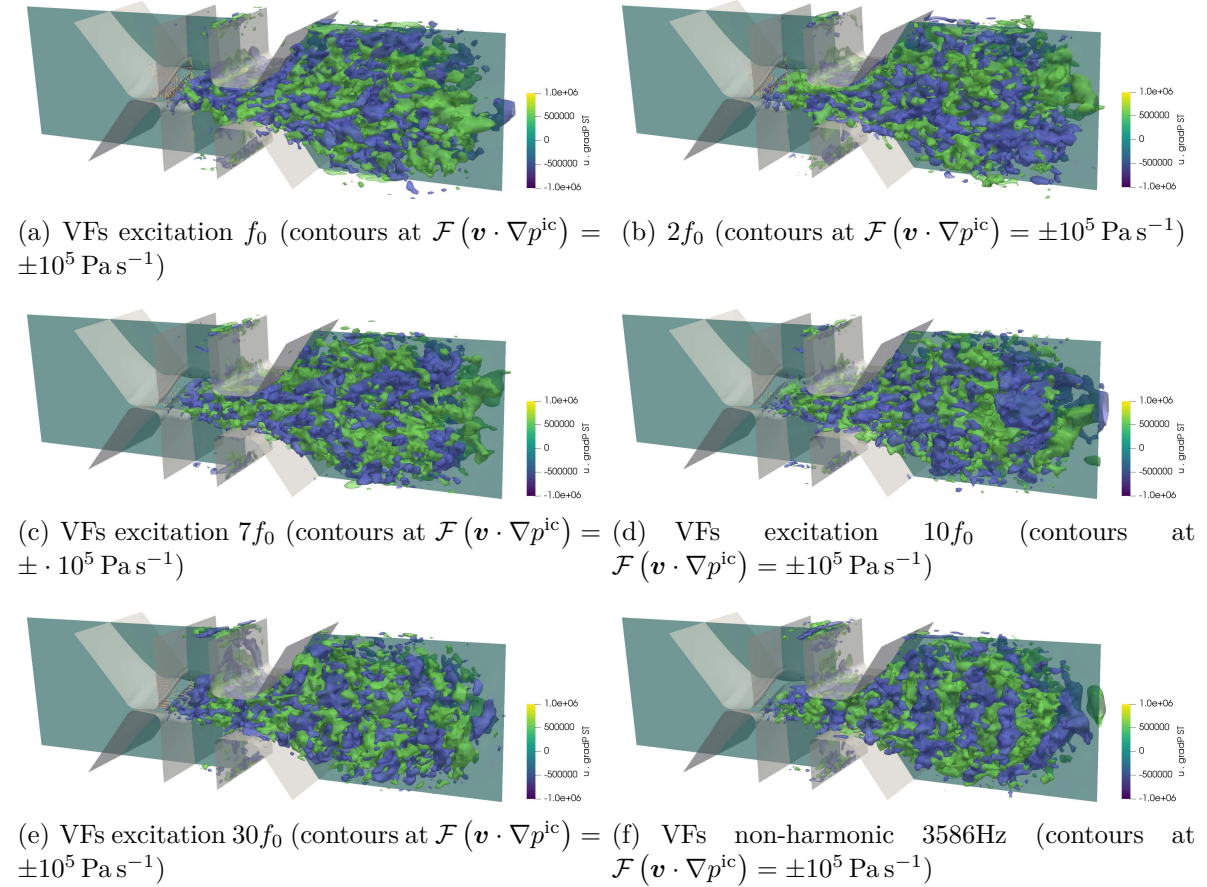


Figure 4.16: Visualization of  $\mathbf{v} \cdot \nabla p^{\text{ic}}$  for in the frequency domain.

Figure 4.18 visualizes the partial time derivative of the incompressible flow pressure in the time domain. Again, during the opening of the VFs, source structures are growing and evolving downstream the vocal tract. When the VFs are fully opened, the structures inside the glottal jet are visible similar to the structures we observed for the convective source term. When the VFs are closing, the increasing flow resistance causes a significant pressure drop, which is shown by the negative source contours in Fig 4.18(c), which are present until the flow is cut-off completely and the flow pressure evens out again. With the perspective of not fully closing vocal folds, this lets us conclude the following as stated in [5]: “Firstly, if the VFs are not fully closing the source energy (at specific time instances) between partly closed and open VFs is not varying in the range of a healthy voice. Secondly, if the VFs are not fully closing the source energy during one cycle is not cut off fully and therefore turbulent and vortical structures are present permanently. These turbulent structures increase the broadband component of the voice signal.”

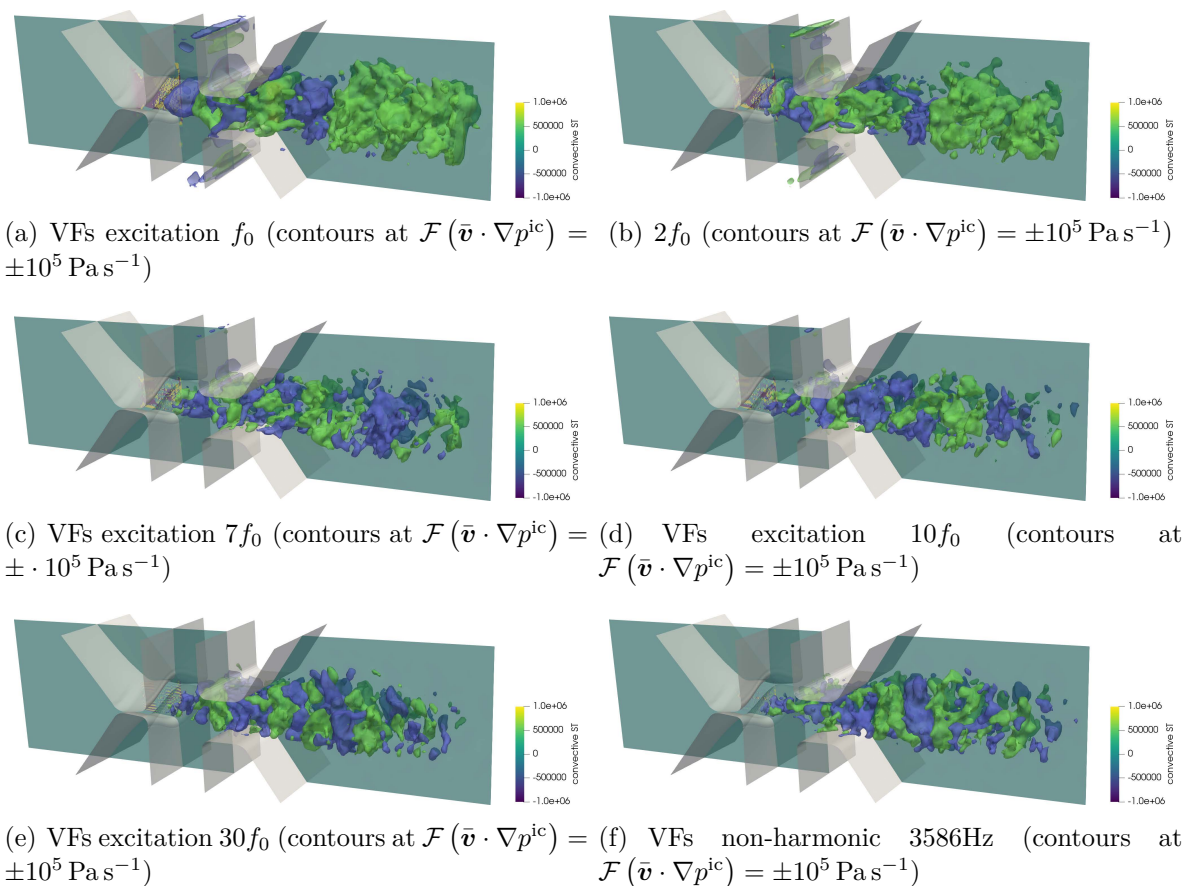


Figure 4.17: Visualization of  $\bar{\mathbf{v}} \cdot \nabla p^{ic}$  for in the frequency domain.

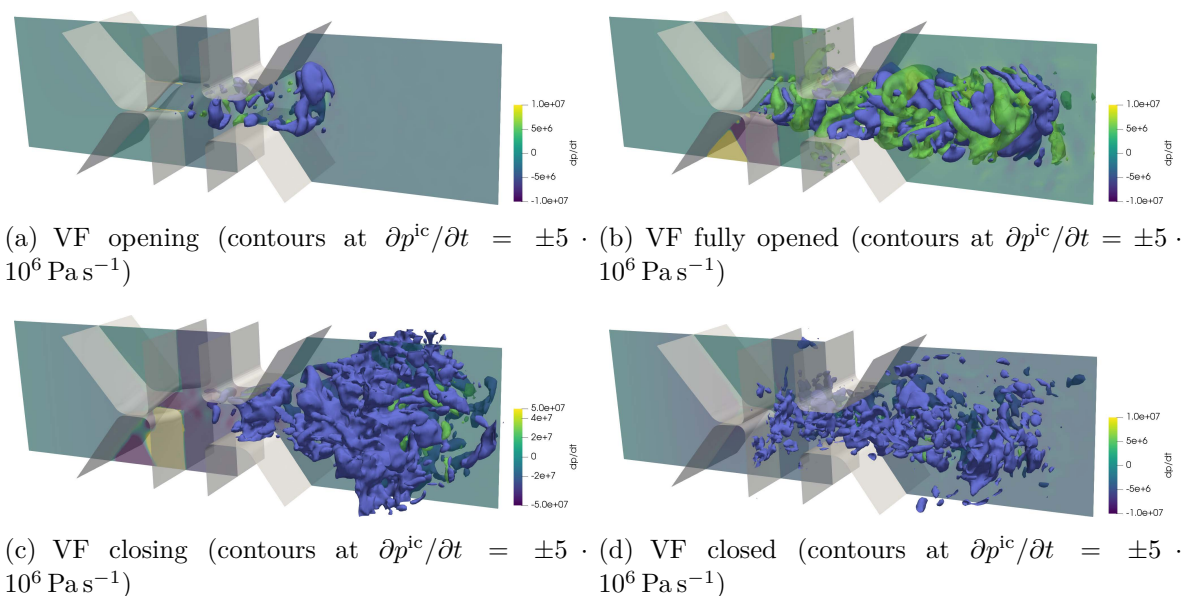


Figure 4.18:  $\partial p^{ic}/\partial t$  during a full cycle.

Figure 4.19 illustrates the local time derivative of the incompressible flow pressure in the frequency domain for the base frequency, several higher harmonics and a non-harmonic frequency. As performing a time derivative in the time domain corresponds to a multiplication with  $i\omega$  in the Fourier transformed domain, the visualized profiles and contours of this source term's oscillation modes are strongly linked with the pressure plots depicted in Fig. 4.6.

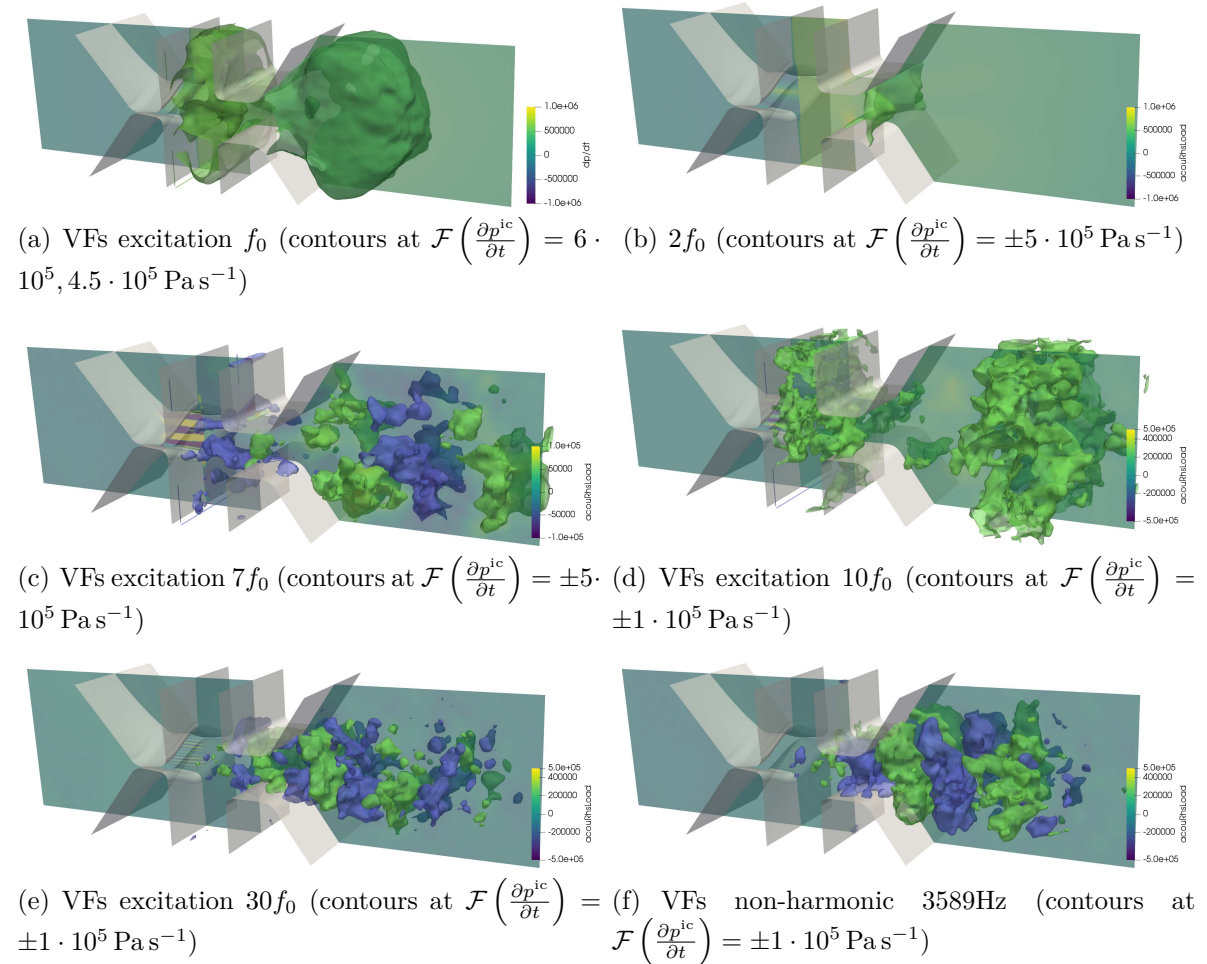


Figure 4.19: Visualization of  $\partial p^{ic}/\partial t$  for in the frequency domain.

In Figure 4.19(a) the base oscillation mode gives much like for the flow pressure, a more or less monotonously decreasing source, that reaches far into the vocal tract. The first couple of higher harmonics (Fig. 4.19(b) and 4.19(d)) again show the propagating fluctuations. Figure 4.19(c) seems to be an exception in this regard as it shows a similar pattern of propagating vortical and turbulent structures downstream the vocal tract that is also observed for very high harmonics (Fig. 4.19(e)) and non-harmonic frequencies (Fig. 4.19(f)). These profiles indicate, that the oscillation mode at those frequencies is not directly coupled to the VF oscillation but rather caused by the turbulent flow that

is generated. Another observation is, that the higher the frequency, the smaller is the spatial extend of the sources. For high frequencies the source structures are basically always located inside the glottal jet region.

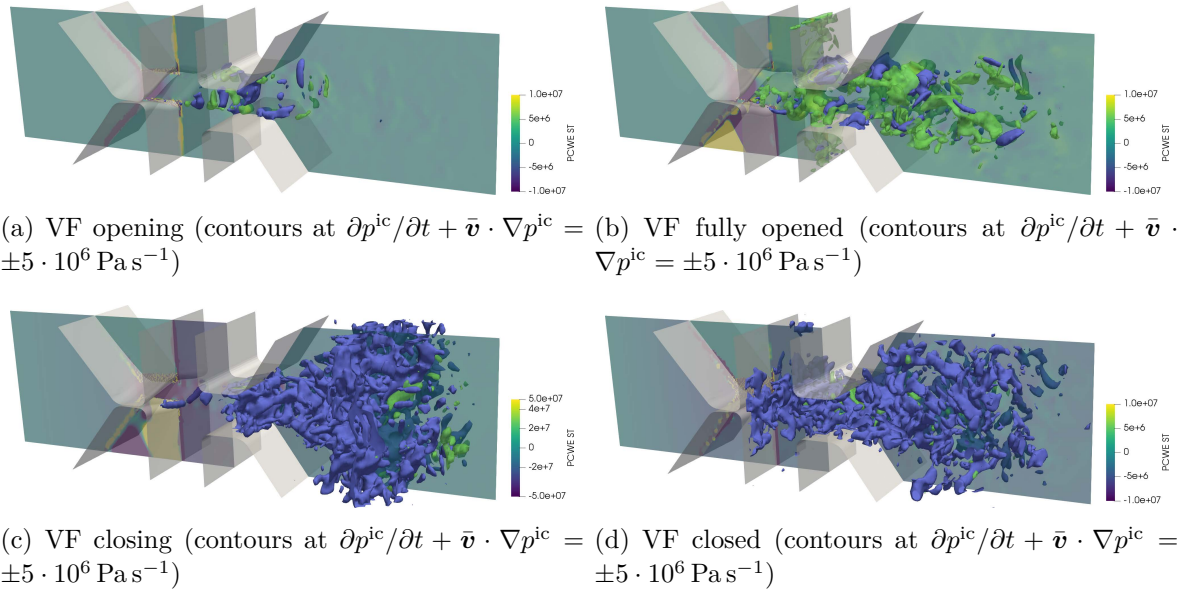


Figure 4.20: PCWE source term during a full cycle.

Figure 4.20 shows the PCWE source term in the time domain. As previously, the 4 subfigures represent the 4 phases during one full cycle. In Fig. 4.20(a), the developing glottal jet during opening VFs. In Fig. 4.20(b), a fully developed glottal jet at maximum strength. In Fig. 4.20(c), the starting vortex decay during closing VFs. And in Fig. 4.20(d), the vortex curling in the stagnating fluid for the fully closed VFs. To sum up, the overall PCWE source for specific time instances looks similar to the time derivative part for the source term visualizations.

In the frequency domain, Fig. 4.21 shows the oscillation modes at 6 frequencies. As the PCWE source sums both previously analyzed source terms  $\partial p^{ic}/\partial t$  and  $\bar{\mathbf{v}} \cdot \nabla p^{ic}$  and the Fourier transformation is a linear operation, the oscillation modes should give a superposition of the oscillation modes of each component. Therefore, at the VF oscillation frequency and the first higher harmonics (see Fig. 4.21(a) and 4.21(b)) the time derivative part of the source term dominates the profile. At high frequencies - both harmonic (Fig. 4.21(e)) and non-harmonic (Fig. 4.21(f)) - the convective source term becomes more important to the shape of the oscillation mode.

For further analysis of the spatial extent of the source terms the convective source term, the local time derivative of the incompressible flow pressure and the sum of both are shown in Fig. 4.22. Therefore, the corresponding values at the center line in the x-direction are evaluated at the four characteristic time steps. In order to calculate the convective source term on the center line, the pressure gradient was approximated by the local derivative in the x-direction  $\frac{\partial p^{ic}}{\partial x}$ , which is valid due to the y and z components of the

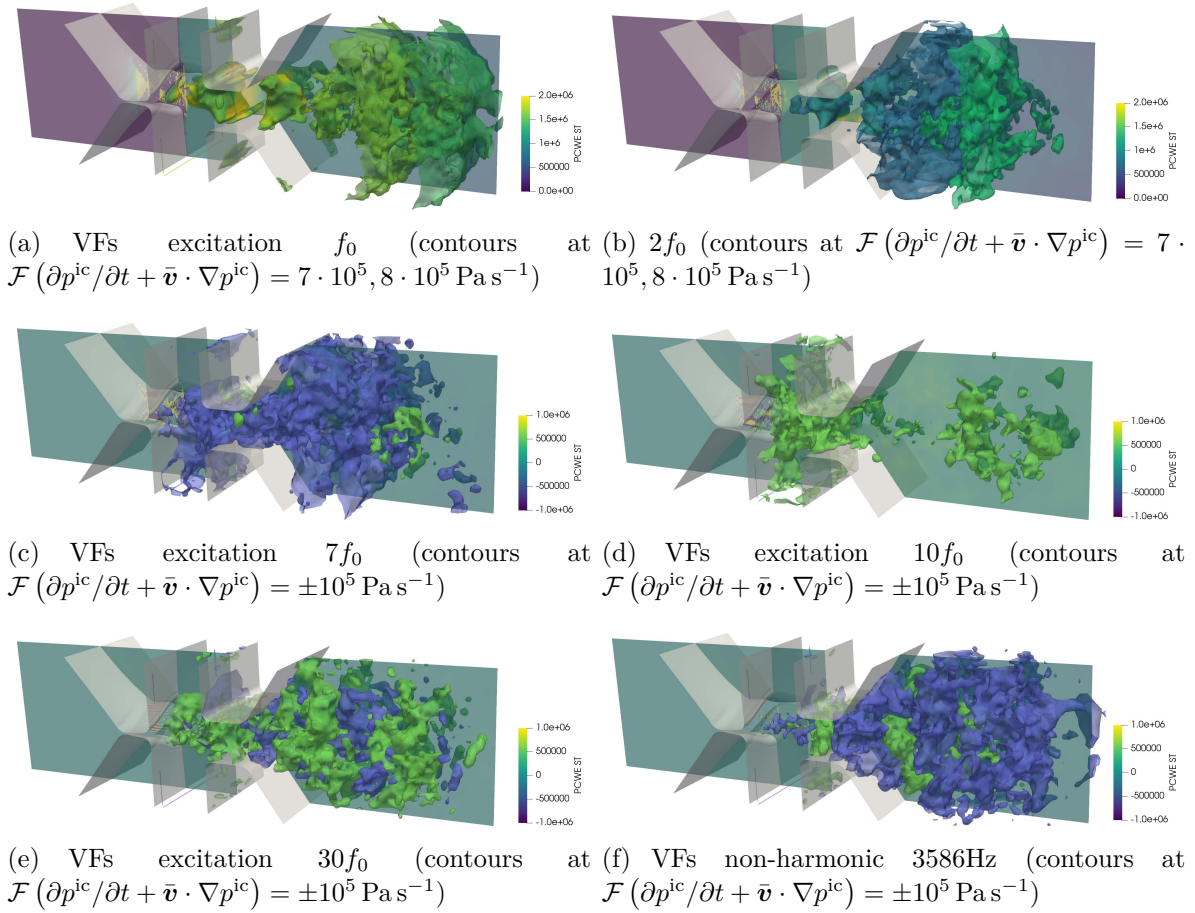


Figure 4.21: Visualization of  $\partial p^{ic}/\partial t + \bar{\mathbf{v}} \cdot \nabla p^{ic}$  in the frequency domain.

mean velocity  $\bar{\mathbf{v}}$  being negligible within the center area along the entire computational domain.

Based on these illustrations, [5] gives an explanation for the previous results and those obtained in [36]:

“First of all, the convective source part  $\bar{\mathbf{v}} \cdot \nabla p$  is localized inside the glottis gap and is of about one magnitude larger than the time derivative source part  $\frac{\partial p^{ic}}{\partial t}$ . However, the time derivative has a larger spatial extend and the integral contribution is larger”.

This global sum over the source terms gives an expectation of the relevancy in the sound spectra in front of the mouth. This indicates, that the convective part is probably less relevant in comparison. From the time instances in Fig. 4.22, we learn that if the gap is narrow, the gradient term is larger, and dominates the visualization (as featured in [36]). If the gap widens, the peak of the convective term is reduced significantly. For a fully opened glottis gap, the convective part and the time derivative part have a similar magnitude. This let us conclude that in the case of glottis insufficiency, we see that the convective term is lower with increasing insufficiency [36]. Although this convective source term is larger in areas of the glottis gap, its overall contribution in the acoustic

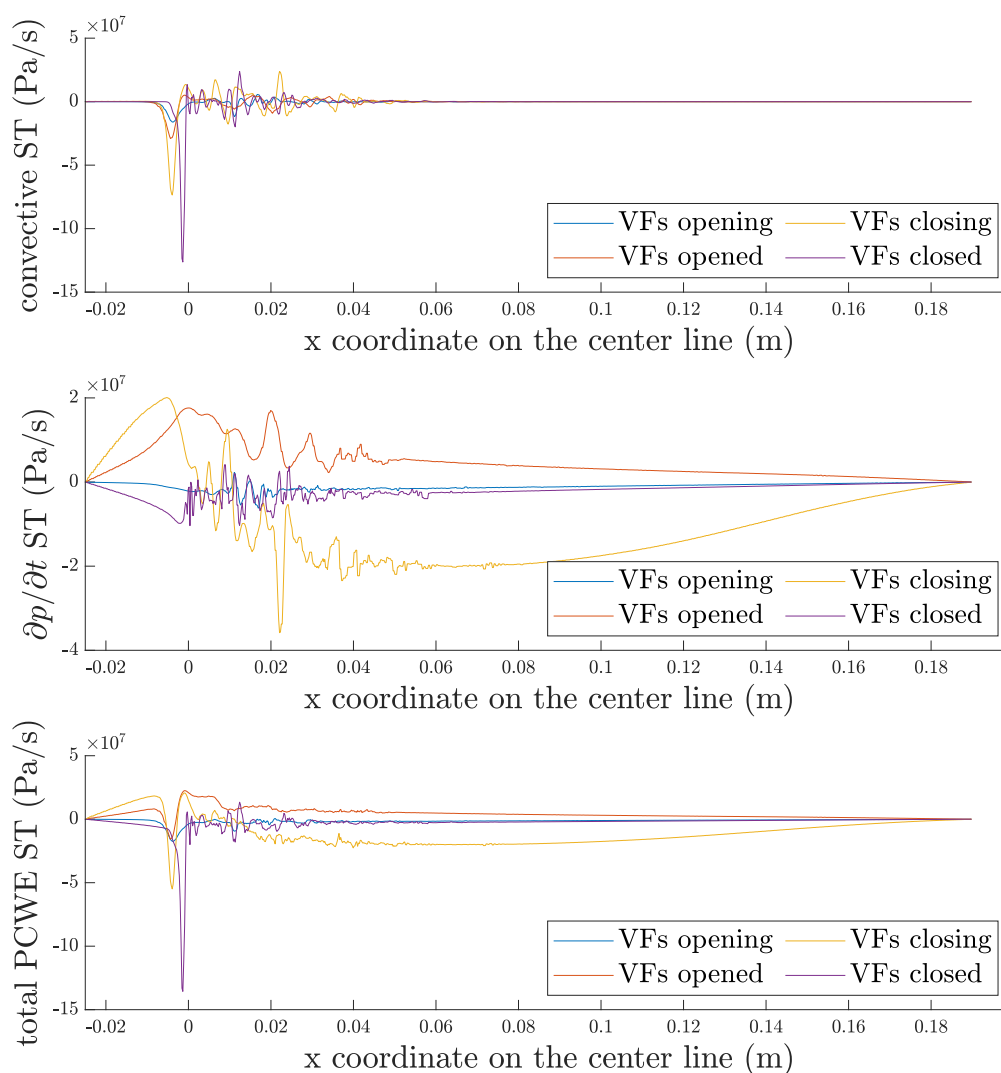


Figure 4.22: Comparison of the flow pressure time derivative and convective source term along the center line in x direction

spectrum is small.

Apart from looking at the spatial distribution of the aeroacoustic sources, further conclusion may be drawn from a global perspective. Investigating the global source gives insight in the energy distribution in the frequency domain. Therefore, the conservatively interpolated source term (RHS of (2.50)) is averaged over all nodes inside the source region. This so-called averaged field FFT yield an globally averaged source, which is depicted in Fig. 4.23. Each contribution is marked by a thin line at the corresponding frequency. Additionally, all contributions at a harmonic frequency are marked by a dot. The spectra

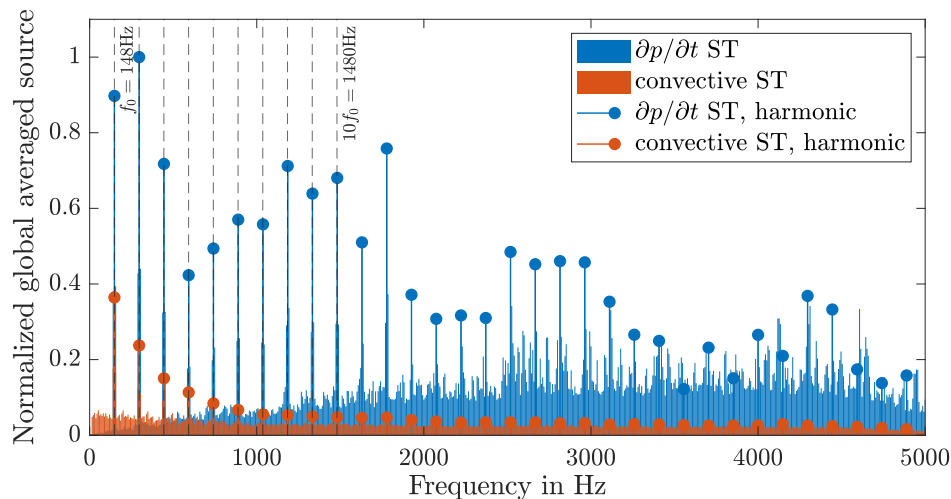


Figure 4.23: Global averaged source of the partial derivative and the convective term

of the averaged field FFT essentially represent the energy content of the primary voice signal, which is the arising sound before it is modified by the filter characteristics of the vocal tract. The result of the averaged field FFT shows, that the convective term has a noteworthy contribution to the total source term in the low frequency range up to about 1500 Hz ( $7f_0$ ). This states a contrast to previous observations made at the analysis of the field FFT plots of the PCWE source term, where the convective source term didn't decrease in amplitude for high frequencies and therefore gains in influence compared to the local time derivative. However, it has to be noted that all previous plots covered only a small part of the vocal tract and, as the convective source term is much more localized around the vocal fold, this shows a decreasing spatial extent with increasing frequency, which isn't as apparent for  $\partial p^{ic}/\partial t$ . In general, the tonal components dominate the spectrum in the lower and middle frequency range, whereas in the higher frequency range the broadband contribution increases and has considerable amplitudes. Regarding a prospective propagation simulation, we can conclude that the convective term might have an impact on the resulting acoustic spectrum in the lower frequency range.

To further investigate the influence of the convective part of the PCWE source term, three acoustic propagation simulations are performed using the presented simulation model with each part of the source term exclusively as well as the whole source term. Additionally, one simulation was performed using the source error  $e$ , as defined in Eq. (4.2), as acoustic source. The acoustic pressure  $p^a$  is extracted at a microphone position inside the propagation region (see Fig. 4.3), which is located at a distance of 1 m in a straight line to the center of the end of the vocal tract (microphone location depicted in Fig. 4.1). Figure 4.24 shows the sound pressure level (SPL) spectrum for these four simulations. Additionally, it includes the SPL spectrum measured at the underlying experimental

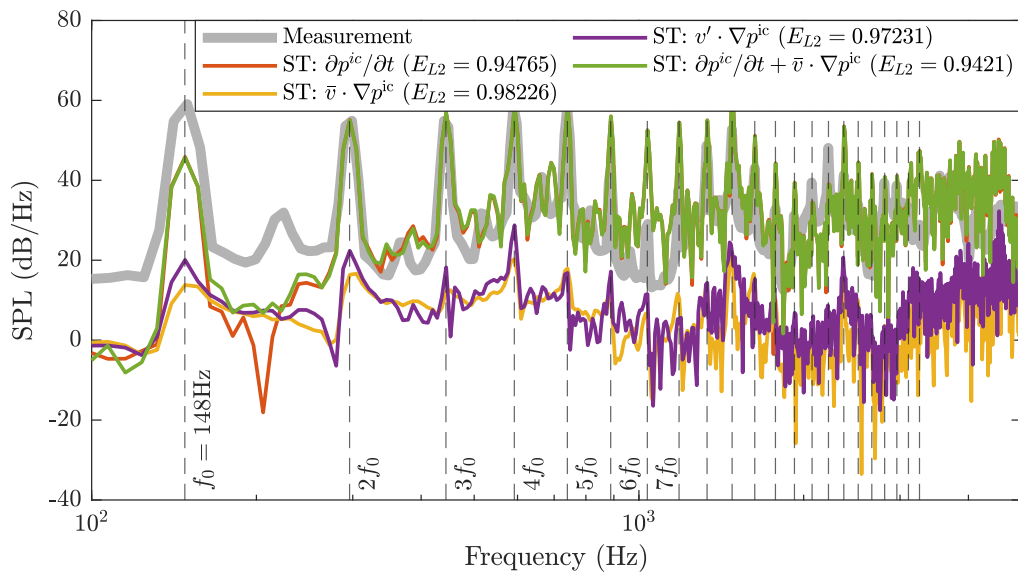


Figure 4.24: Sound pressure level of simulations using  $\partial p^{\text{ic}}/\partial t$ , the convective part  $\bar{\mathbf{v}} \cdot \nabla p^{\text{ic}}$ , the source error  $\mathbf{v}' \cdot \nabla p^{\text{ic}}$  and the full PCWE source term as acoustic source in comparison with experimental measurement data at a microphone positioned 1m from the end of the vocal tract (see [28]).

model, on which this simulation is based on [28]. Comparing the spectrum of the convective source error with the spectrum of the convective part of the PCWE source term, it produces a similar spectrum which indicates a significant difference between the convective parts of the PCWE and PCE source terms. However, both spectra result in a low SPL that further decreases with increasing frequency. In contrast, the SPL gained from the other 2 simulations using the local time derivative of the incompressible flow pressure and the full PCWE source term respectively are visually indistinguishable, especially for high frequencies. Overall the obtained spectrum matches well with the measurement data for frequencies  $f > 2f_0 = 296$  Hz.



Die approbierte gedruckte Originalversion dieser Diplomarbeit ist an der TU Wien Bibliothek verfügbar.  
The approved original version of this thesis is available in print at TU Wien Bibliothek.

# Chapter 5

## Application - Axial Fan

In this chapter, the methods, that were introduced in chapter 3 are applied to numerically simulate the flow induced sound of an axial fan and validate the results with measurement data. This work gives a more detailed version of the results published in [6]. Section 5.1 describes the experimental setup, that is used to validate the simulation results. The simulation setup and in particular the setup for both, the CFD-computations and the CAA-computations, is given in section 5.2.

### 5.1 Experimental setup

The experimental setup consists of a fan in a short duct, which is depicted in figure 5.1(a). The fan has nine blades with a tip diameter of 495 mm and is installed in a duct with a diameter of 500 mm. The fan is driven by a motor inside the duct and is embedded in a sound hard tube. All measurements of sound pressure were performed according to ISO 5801 [37] in a standardized test chamber, which is depicted in figure 5.1(b). The rotational speed of the fan is approximately 1500 rpm yielding a volume flow of  $1.3 \text{ m}^3/\text{s}$ . A more detailed explanation of the experimental setup can be found in [38], where the same setup was used.

### 5.2 Simulation setup

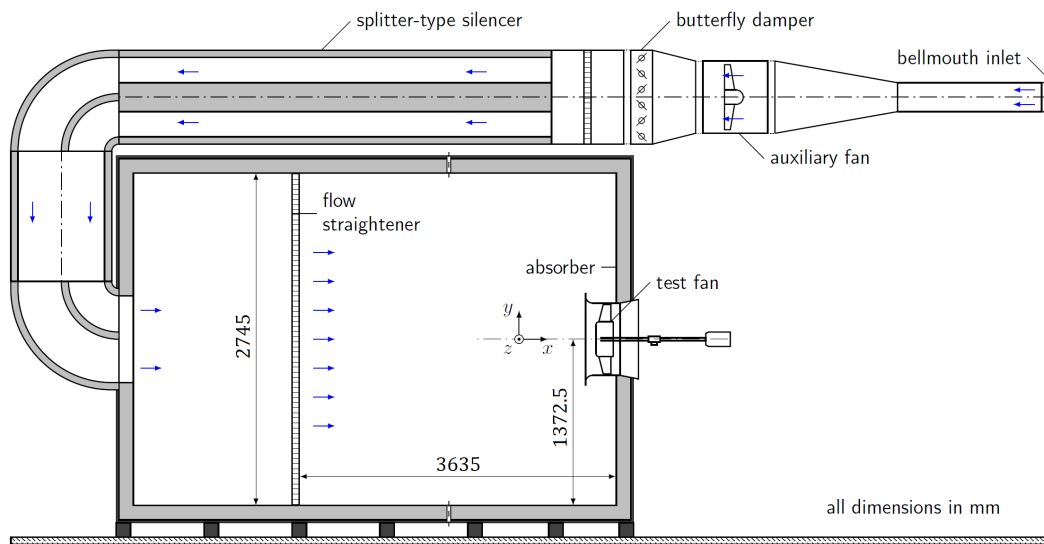
The simulation setup follows the hybrid approach described in chapter 3 and consists of a CFD simulation for the incompressible turbulent flow and a FE-based computation of the acoustic wave propagation.

#### 5.2.1 Computational fluid dynamics (CFD)

The rotational speed of 1500 rpm gives a circumferential velocity of about  $38.9 \text{ m/s}$ , which yields a Mach number of  $\text{Ma} \approx 0.113$ . Therefore, the flow can be described by an incompressible flow field, which is formulated with the use of the conservation equations introduced in chapter 2. The CFD mesh is depicted in Fig. 5.2 and consist of about 33



(a) Investigated fan.

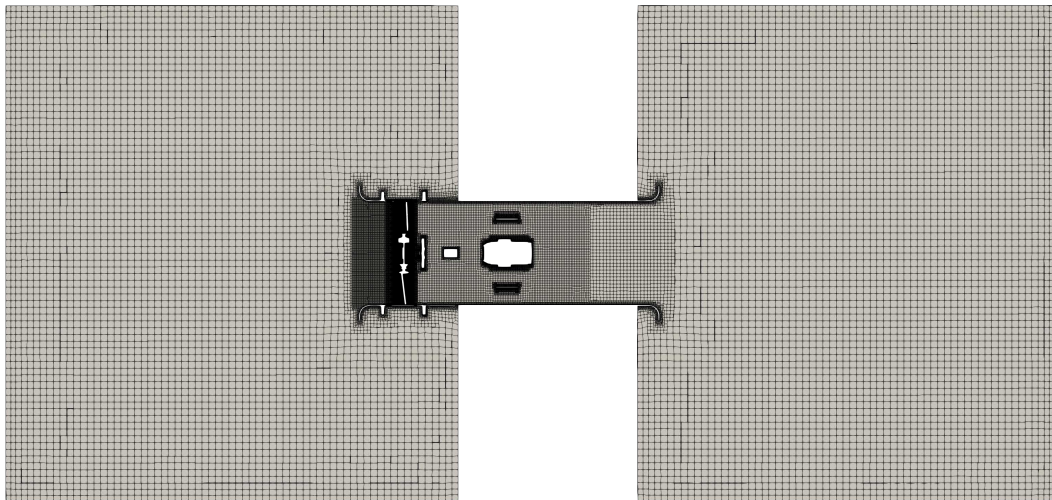


(b) Standardized inlet test chamber

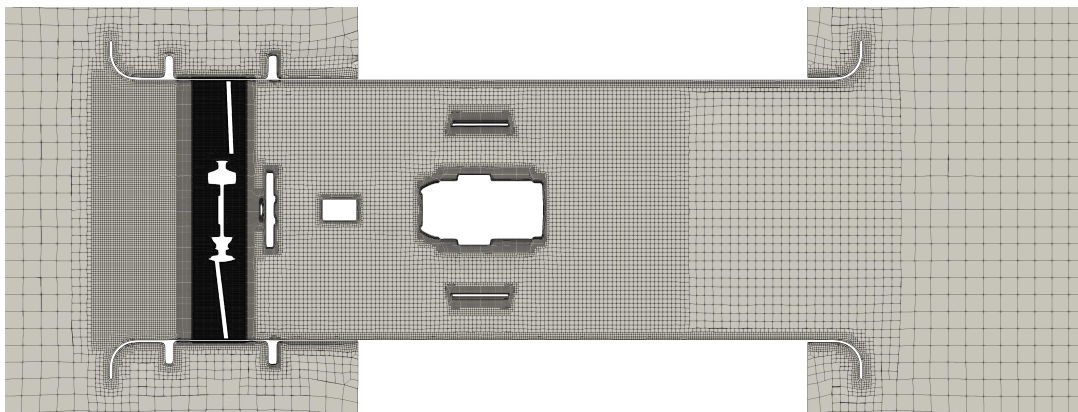
Figure 5.1: Experimental setup.

million cells. It is separated into 3 regions: an inlet region, containing the suction pipe and the surrounding air, the rotor region, which discretizes the surrounding air of the rotor blades and rotates with the rotor angular velocity, and the outlet region, which contains the air in the outlet pipe as well as the surrounding air at the outlet. The rotor region has a maximum cell size of 1 mm and is refined towards the blade tips and therefore makes up about 22 million cells by itself.

To model the turbulent flow, a detached eddy simulation was used analog to the computations done in [38]. The computations were performed using the OpenFOAM (Open Field Operation and Manipulation) Toolbox v2.3.0, which is an open source C++ library and capable of solving the incompressible Navier-Stokes equations based on a finite vol-



(a) Slice of the whole CFD domain



(b) Closer view of the axial fan

Figure 5.2: CFD mesh

ume scheme. The incompressible pressure, required for the source term computation later on is then exported in the EnSight Case Gold file format.

### 5.2.2 Computational aeroacoustics (CAA)

To model the aeroacoustics, the PCWE formulation (see section 2.3.2) was used. Because of the splitting of incompressible and acoustic pressure, it is possible to analyze the sound generating mechanisms by investigating the aeroacoustic sources. It also takes reflections and refractions into account, which is very important, because the duct and the nozzle have a significant impact on the wave propagation. Figure 5.3 depicts the simulation domain for the aeroacoustic computations. Again, the computational domain is split into the 3 regions, that were defined for the CFD calculations. On the boundaries of the inlet and outlet regions, 2 PML (perfectly matched layer - see section 3.2) regions are

added to account for the free radiation condition. The reflecting surfaces of the nozzle, duct, strut, driving shaft, and motor are modeled as sound-hard walls. In contrast to the CFD, for the wave propagation, the mesh in the rotor region, where the main acoustic source terms occur, is static and therefore, the elements have to be connected accordingly during the interpolation. The 2 propagation regions in red and gray yield large mesh ratios  $\Gamma$ , and therefore produce source artifacts for the cell centroid based interpolation. However, as explained in section 3.4.3, this should have nearly no effect on the resulting sound pressure level at the microphone positions. After the interpolation, the acoustic propagation computation was done with the FE solver CFS++ [22].

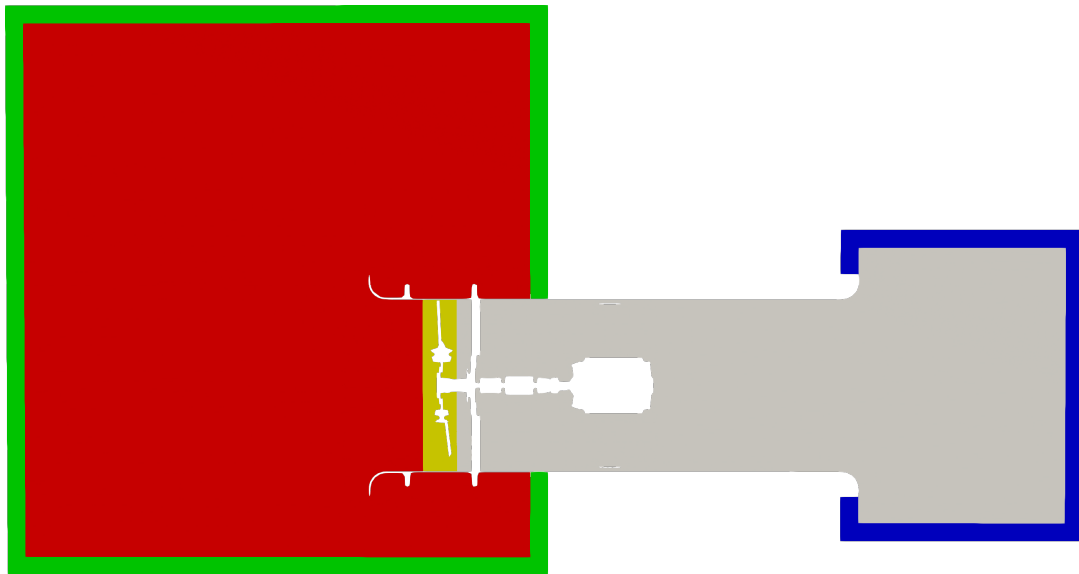


Figure 5.3: Geometry of acoustic domain: rotating source region in yellow, inlet region in red, outlet region in gray, and PML regions in green and blue

### 5.3 Comparison of the interpolation algorithm

To study the behavior of the interpolation algorithms, the sound source term was calculated using the incompressible pressure and its gradient, both of which were obtained from the CFD simulation. The source term was interpolated onto the acoustic network using the two different interpolation approaches. The acoustic propagation simulation was carried out with the same solver settings that were used in [38]. The results of the two simulations are compared with the measurement results in Fig. 5.5. To make the measurement and the simulation comparable, the sound power spectral density (PSD) was used:

$$\text{PSD} = 10 \log \left( \frac{\hat{P}}{p_0^2} \right) \quad (5.1)$$

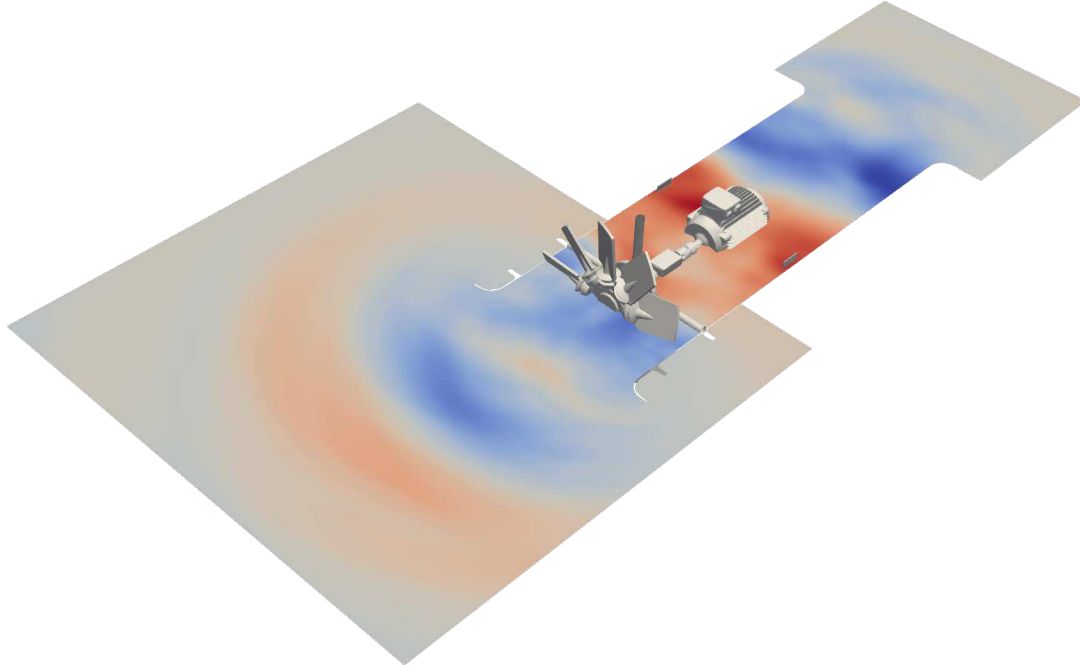


Figure 5.4: Acoustic pressure field in a cross-section of the CAA domain at a simulation time of 320 ms

$p_0 = 20 \mu\text{Pa}$  is the reference pressure and  $\hat{P}$  is the power spectral density estimate of the acoustic pressure, obtained with Welch's method [39],

$$\hat{P} = \frac{1}{M} \sum_{i=1}^M \hat{P}^{(i)} \quad (5.2)$$

$$\hat{P}^{(i)} = \frac{1}{LU} \left| \sum_{k=1}^L w(k) p_i(k) e^{-j\omega k} \right|^2 \quad (5.3)$$

after applying a kaiser window function [40] ( $\beta = 2$ ) on the selected data (window normalization constant  $U = 1/L \sum_{k=1}^L |w(k)|^2$ ), which is separated into  $M$  samples of length  $L = 2048$ .

All depicted results show the PSD at a position of 1 m in front of the inlet nozzle. The black line represents a measurement with a measurement time of 30 seconds. The gray lines are measurement results with a measurement time of 0.1 s, which is close to the simulation time of 0.08 s. Both simulation results show a step drop above 6 kHz, with the mesh resolution in the propagation range being coarse compared to the acoustic wavelength. The dominant peak at a frequency of 300 Hz is a result of both the interaction of the tip gap flow and the blade passing frequency [41]. It should be emphasized that these frequencies are not the same; However, due to the frequency resolution used in this case, they merge into one peak. This peak is well represented in both frequency and amplitude. The red curve shows the result of the cell-centroid-based approach. It predicts PSD well over the entire frequency range and is therefore useful in cases with complex

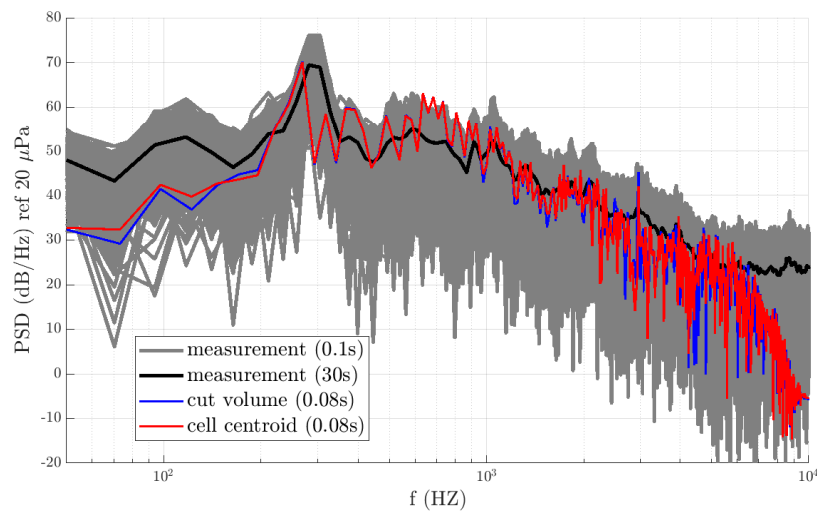


Figure 5.5: Comparison of the PSD using the cell-centroid based and the cut-volume cell interpolation algorithm with measurement results.

geometry and distorted grid cells of different cell sizes. This statement applies as long as the CFD cells are smaller than the CAA cells. The blue graph represents the result of the cut-volume cell approach, which shows overall good agreement with the measurement. This application shows that cut-volume cell based interpolation can process complex geometries that occur in real applications. The intersection algorithm has an additional computing time of around 45 minutes and depends heavily on the number of CFD cells. Table 5.1 shows a slight increase in the intersection time with increasing CAA elements. Based on the coverage ratio, the calculations can be automated to switch from ordinary cell-centroid based interpolation to more advanced interpolation if necessary.

## 5.4 Artifacts inside the propagation domain

In regions with a highly refined CAA mesh (or a highly coarsened CFD mesh - which both leads to a large mesh ratio  $\Gamma$ ), artifacts occur within the finite element source distribution for the cell-centroid interpolation. Figure 5.6 shows these artifacts in comparison to the cut-volume cell sources, which have no artifacts within the computation domain. As previously explained, however, these artifacts have little impact on low Mach number applications. Although a small phase error is introduced, these artifacts should not be a particular problem. However, in the direction of higher Mach numbers, these artifacts can have an impact. Source blending can then be used to mitigate spurious acoustic modes as an alternative to the illustrated cut-volume cell interpolation.

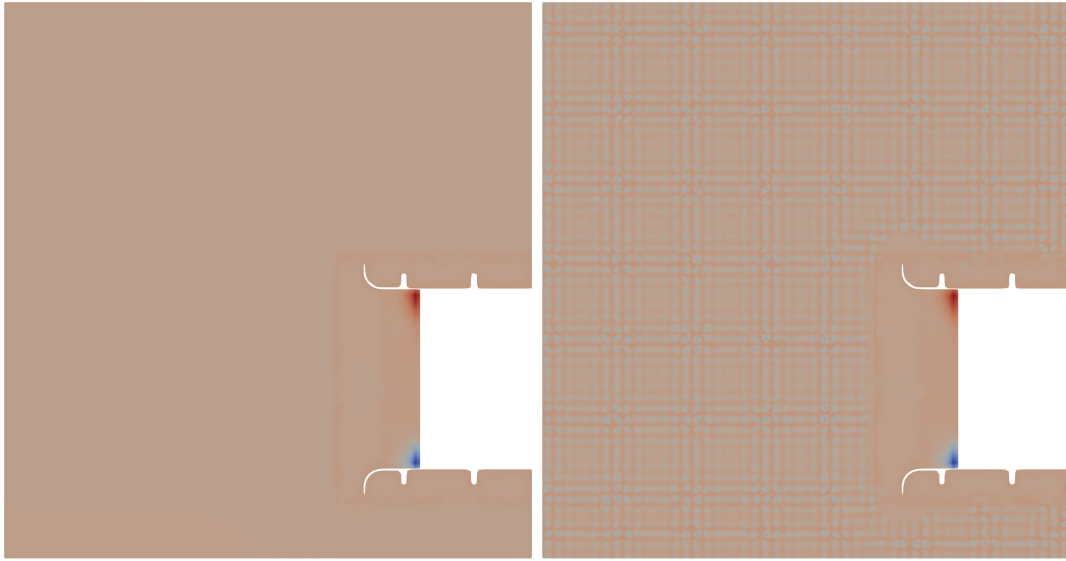


Figure 5.6: Comparison of the nodal values using the cut-volume cell interpolation (left) and the cell-centroid based cell interpolation algorithm (right).

## 5.5 Grid study

In order to investigate the influence of the CAA grid resolution on the cut-volume cell algorithm, a grid study was performed. The cut-volume cell algorithm was used to interpolate the acoustic source on five different grids in the rotating area. All grids are tetrahedral and have different grid sizes. The numbers of elements in the source region are shown in Tab. 5.1, where mesh 1 is the finest and mesh 5 is the coarsest mesh with comparatively poor mesh quality. The mesh of the propagation domain was not changed for the various simulations and counted 1,804,377 nodes. A change to this mesh would cause an additional deviation in the results that is not subject to this mesh study.

The different meshes of the rotating region are shown in Fig. 5.7, where the meshes become coarser from left to right. The minimum cell size of the CAA mesh occurs in the tip gap, whereby the element size for all CAA meshes is 1 mm. This is necessary in order to resolve the gap with at least two elements independently of the discretization of the rest of the mesh. Therefore, the elements in the tip gap dominate the total number of elements for coarse meshes and therefore limit the minimum number of elements. The maximum CFD cell size at this point is 0.2 mm, which gives a ratio of  $CAA/CFD = 5$ . The PSD that resulted from the CAA computation using the interpolated source term and the PSD of the measurements are displayed in Fig. 5.8.

The colored lines are the result of the numerical simulations with the different meshes. Fig. 5.8(a) shows the PSD that results from simulation with all different meshes using the cell-centroid interpolation, while Fig. 5.8(b) shows the same results when using the cut-volume cell interpolation. In the low frequency range, all simulations underestimate the

Table 5.1: Different meshes used in the source region to investigate the cut-volume cell interpolation and the cell-centroid based interpolation. The coverage ratio measures the relative coverage of CAA cells by CFD cells for the cell-centroid based interpolation. The intersection time describes the excess CPU time of the cut-volume cell interpolation, due to the intersection algorithm. The execution time describes the averaged CPU time (using 4 threads), that was used to calculate the acoustic sources with the cut-volume interpolation for one time step.

	Source region		Max.	Coverage	Intersection	Execution
	elements	nodes	element size	ratio $\varepsilon$	time	time per step
Mesh 1	7690908	1322937	7 mm	85.24 %	49 min	33.3 s
Mesh 2	1021697	181186	12 mm	99.78 %	45 min	29.0 s
Mesh 3	555562	96535	18 mm	92.87 %	42 min	24.7 s
Mesh 4	337013	58708	24 mm	95.14 %	41 min	23.9 s
Mesh 5	153256	27765	48 mm	98.36 %	42 min	25.3 s

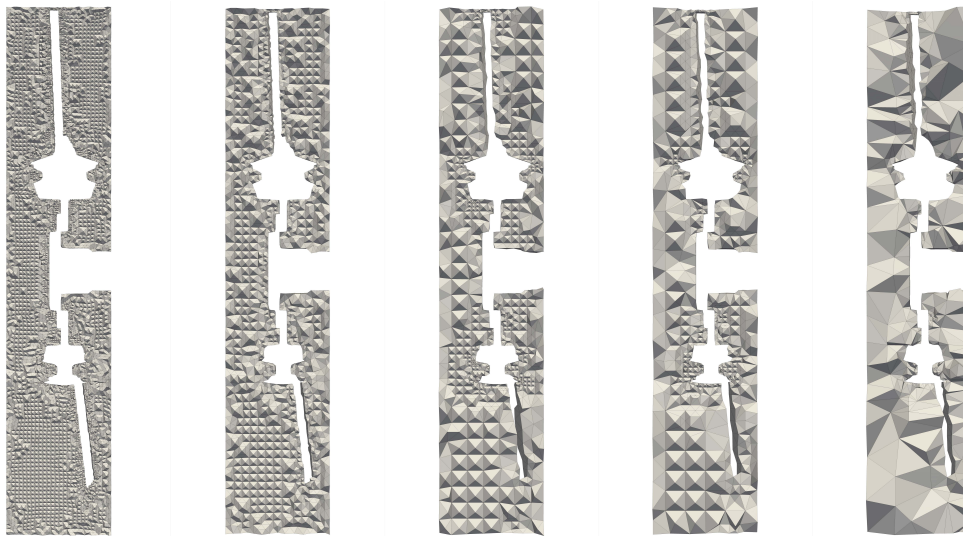
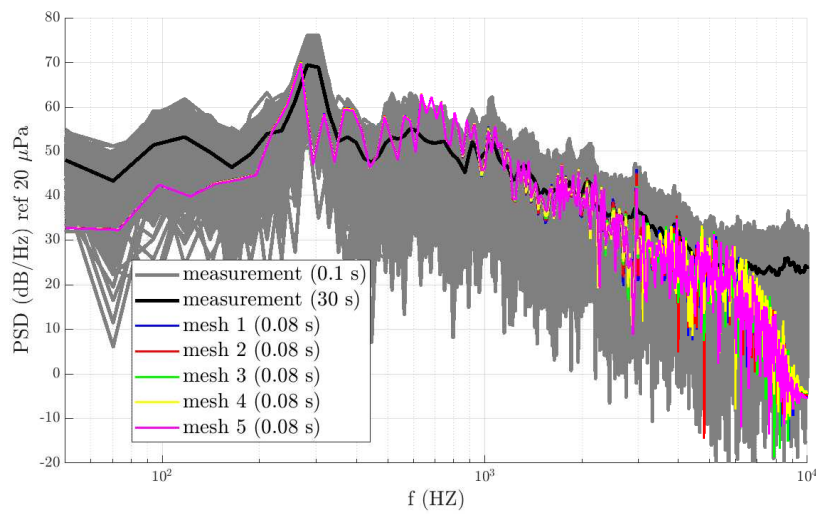
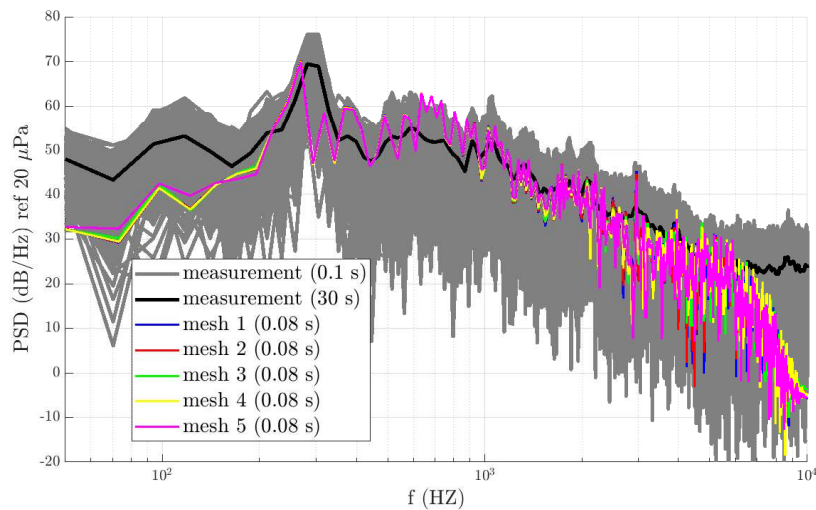


Figure 5.7: Different meshes used for the computation (finest mesh 1 to the coarsest mesh 5 from left to right).

PSD, which is possibly due to the short numerical simulation time and the aeroacoustic formulation. The trend in the higher frequency range agrees well with the measurement. Above a frequency of 6 kHz the PSD drops because the mesh density in the propagation region is too coarse to resolve the respective wavelengths and the time-stepping scheme with controlled dispersion (Hilber-Hughes-Taylor) numerically attenuates sound waves with higher frequency. For the cell-centroid interpolation, all meshes deliver al-



(a) Acoustic power spectral density using cell-centroid interpolation.



(b) Acoustic power spectral density using cut-volume cell interpolation.

Figure 5.8: Acoustic power spectral density comparison of different discretizations.

most identical result up to a frequency of 1 kHz. Above this frequency it can be seen that the finer meshes lead to more distinctive peaks, but the deviation is rather small. For the cut-volume interpolation, again, meshes 1 to 4 provide almost identical results up to a frequency of 1 kHz. Mesh 5 delivers small deviations even at low frequencies. This could be caused by the rather poor mesh quality due to the above-mentioned limitation of the maximum mesh size in the tip gap. It is assumed that the deviation in the high frequency range has its origin in the mesh density of the source region, in which the coarsest mesh fulfills its limitations, to resolve the geometric shape of the source

terms. Overall, the results of all 10 simulations combined confirm the robustness of the cut-volume cell interpolation algorithm. [6] In addition, reducing the number of nodes in the rotating region reduces the total number of nodes. This reduces the size of the FE system and thus the computing time. For the finest mesh, the total CPU time was 930 h, and for the coarsest mesh, the total CPU time reduced to 229 h. The large reduction in CPU time is due to the fact that the finite element simulation time is proportional to the square of the number of nodes. Overall, in this case of an axial fan, due to the geometric properties and the properties of the aeroacoustic source resulting from the tip gap flow, the breakdown of the cut-volume cell approach is limited, since the tip gap must be resolved by at least one element.

To continue with further comparisons, the averaged sound pressure level is introduced to quantify the accuracy of each simulation in a scalar. The averaged sound pressure level is defined by

$$\bar{L}_P = 10 \log \left( \frac{1}{T} \int p_n^2 dt / p_0^2 \right) \text{ dB}, \quad (5.4)$$

with a reference pressure  $p_0 = 20 \mu Pa$ .

Table 5.2: Comparison of the sound pressure level and the deviation of the power spectral density for the different meshes using cut-volume and cell-centroid interpolation

	cut-volume cell interpolation		cell-centroid based interpolation		
	$e_{L_2}^*$	$\bar{L}_P$	$e_{L_2}^*$	$e_{L_2}^{**}$	$\bar{L}_P$
Mesh 1	0 %	88.2972 dB	5.45 %	0 %	88.2835 dB
Mesh 2	3.37 %	88.2550 dB	6.52 %	5.45 %	88.2454 dB
Mesh 3	7.82 %	88.1963 dB	8.85 %	6.38 %	88.1748 dB
Mesh 4	10.83 %	88.1617 dB	10.81 %	8.70 %	88.1490 dB
Mesh 5	13.85 %	88.0037 dB	13.85 %	12.66 %	88.0038 dB

\* in reference to simulation of Mesh 1 and cut-volume cell interpolation

\*\* in reference to simulation of Mesh 1 and cell-centroid based interpolation

Table 5.2 shows the averaged sound pressure level at the microphone position for all simulations examined. The sound pressure level varies only slightly for the various meshes and both simulation setups. This is as expected as the PSD of all simulations was pretty similar. Furthermore, the relative  $L_2$ -error of the power spectral density is calculated by

$$e_{L_2} = \sqrt{\frac{\sum_{f_{\min}}^{f_{\max}} (PSD_{\text{ref}} - PSD)^2}{\sum_{f_{\min}}^{f_{\max}} PSD_{\text{ref}}^2}} \quad (5.5)$$

and shown in Tab. 5.2 with reference to the finest mesh (mesh 1).  $f_{\min}$  and  $f_{\max}$  are selected as 100Hz and 5kHz, respectively. Both interpolation methods result in small

deviations for the finest mesh. The  $L_2$ -error increases steadily with increasing mesh size. However, both conservative interpolation methods give similar and acceptable accuracy.

Another aspect is the monotonically converging averaged sound pressure level for finer meshes. This is examined using the Grid Convergence Index (GCI) introduced in chapter 3.5. The averaged sound pressure level from the simulations with meshes 1, 2, 4 and 5 are therefore used to estimate an approximate result for an infinite mesh resolution. Mesh 3 is not included in this analysis because it is considered an outlier and also in order to guarantee a refinement ratio of  $r_{i,j} = \frac{h_j}{h_i} > 1.3$ , as proposed by [27]. The relative refinement is estimated by the ratio of the averaged element sizes

$$r_{i,j} \approx \sqrt[3]{\frac{n_{el,i}}{n_{el,j}}} \quad (5.6)$$

where  $n_{el}$  is the number of elements inside the rotating region of the corresponding mesh. As a result of this analysis, the estimated averaged SPL  $\bar{L}_p^{\text{ext}} = 88.2972$  dB and  $\bar{L}_p^{\text{ext}} = 88.2835$  dB and orders of convergence  $p = 2.835$  and  $p = 2.659$  are extrapolated for the cut volume and cell centroid interpolated simulations, respectively. Figure 5.9 shows the averaged sound pressure level in respect to the normalized element size estimate and the extrapolated value. Table 5.3 summarizes the results for the cut-volume interpolation and includes the averaged SPL for the 30s measurement as well as the spread for 0.1s measurements in the frequency range of 100Hz to 5kHz. The measurements yield an averaged SPL of  $\bar{L}_P = 88.556$  dB for the 30s measurement. Fig. 5.10 also shows the SPL spread for 0.1s measurement data. The measured signal generally results in a slightly higher averaged sound pressure level, since low and high frequencies are underestimated by the simulation. However, all the meshes that were analyzed give an approximation for the averaged SPL, which is well within the bandwidth of the 0.1s measurements.

Table 5.3: GCI based on Richardson Extrapolation and measurement results

	cut-volume		cell-centroid		refinement ratio $r_{i,i+1}$
	$\bar{L}_P$	$GCI$	$\bar{L}_P$	$GCI$	
30 s Measurement	88.556* dB	-	88.556* dB	-	-
Extrapolation	88.3049 dB	-	88.2956 dB	-	-
Mesh 1	88.2972 dB	0.1041 ‰	88.2835 dB	0.1084 ‰	1.960
Mesh 2	88.2550 dB	0.7142 ‰	88.2454 dB	0.8172 ‰	1.447
Mesh 4	88.1617 dB	2.0301 ‰	88.1490 dB	2.0398 ‰	1.3004
Mesh 5	88.0037 dB	4.2745 ‰	88.0038 dB	4.1013 ‰	-

\* for 30s measurement, [84.746, 92.176] dB bandwidth for measurements with 0.1s measurement time.

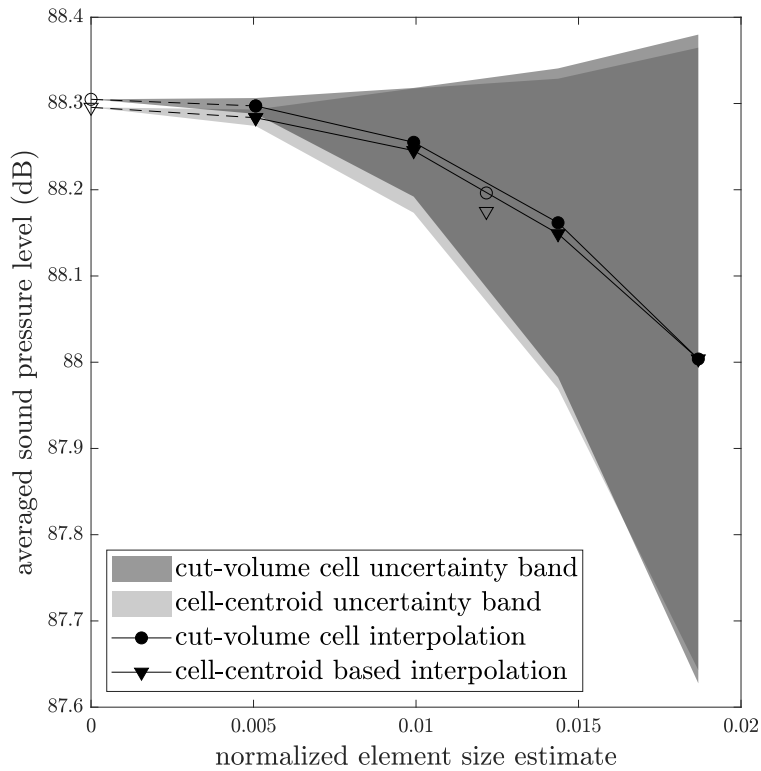


Figure 5.9: Grid convergence regarding mesh refinement using Richardson Extrapolation.

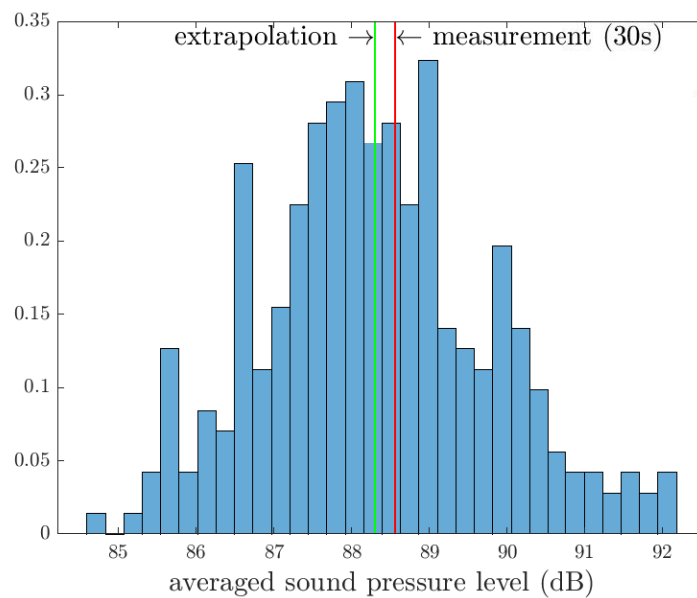


Figure 5.10: Histogram of the averaged sound pressure level of the measurement.

# Chapter 6

## Conclusion and Outlook

This thesis describes a hybrid CAA approach that uses the Perturbed Convective Wave Equation (PCWE) to separate acoustics from fluid dynamics. Starting with introducing the fundamentals of fluid dynamics and acoustics, the work provided a detailed explanation of the used methodology to numerically simulate aeroacoustic problem sets starting from a CFD simulation of the incompressible flow field.

One focus was set on the conservative interpolation, which allows optimal grids for both CFD and CAA computations. Therefore, two interpolation methods were introduced and compared in regards of their limitations. Furthermore, a grid study was performed for an axial fan analyzing the feasibility of both methods in real technical applications. The second focus of this thesis was on analyzing and discussing the aeroacoustic sources that appear inside an experimental vocal tract, which models human phonation. Thereby, various components of the acoustic source terms, that are defined by the PCWE analogy are visualized both in time and frequency domain, and investigated towards their impact on a prolonging acoustic propagation computation.

Finally, it is remarked, that during the work on this thesis, two publications were created based on the previously described work as well as existing simulation results, that were evaluated and interpreted.

As a next step in the FWF (Austrian Research Council) project *Numerical computation of the human voice source*, the findings of this work are incorporated in the existing simulation workflow in order to create a more accurate methodology. Furthermore, the improved simulation workflow is going to be used to simulate various types of dysphonia. This allows for working out methods to investigate the cause of any voice disorder by evaluating simple measurement results.



Die approbierte gedruckte Originalversion dieser Diplomarbeit ist an der TU Wien Bibliothek verfügbar.  
The approved original version of this thesis is available in print at TU Wien Bibliothek.

# List of Figures

3.1	CAA workflow . . . . .	12
3.2	Cell-centroid based interpolation approach . . . . .	15
3.3	General mesh sizes of flow and acoustic grid . . . . .	16
3.4	Cut-volume cell approach . . . . .	17
3.5	RHS values of FE nodes for different mesh ratios and interpolation method	20
3.6	Wave number content . . . . .	21
3.7	Source regions with different generic sources . . . . .	22
3.8	Regions and mesh of the CAA simulation. . . . .	23
3.9	Different meshes for the interpolations . . . . .	24
3.10	Results of the coarsest discretizations for the generic sources . . . . .	25
3.11	Results of the fine discretizations for the generic sources . . . . .	26
4.1	Experimental Setup . . . . .	30
4.2	GAW . . . . .	31
4.3	CAA Setup . . . . .	32
4.4	GAW with characteristic timesteps . . . . .	33
4.5	Fluid pressure visualization during a full VF cycle. . . . .	34
4.6	Fluid pressure visualization for several frequencies. . . . .	35
4.7	Flow pressure and velocity over the computational domain . . . . .	36
4.8	Fluid mean velocity field magnitude $ \bar{\mathbf{v}} $ . . . . .	36
4.9	Turbulent kinetic energy (TKE) $k$ during a full VF cycle. . . . .	37
4.10	Flow velocity visualization for several frequencies. . . . .	38
4.11	Flow pressure gradient field magnitude $ \nabla p^{\text{ic}} $ in the time domain . . . . .	38
4.12	Flow pressure gradient field magnitude $ \nabla p^{\text{ic}} $ visualization for several frequencies. . . . .	39
4.13	Convective part of the source term $\mathbf{v} \cdot \nabla p^{\text{ic}}$ as it is present in the perturbed compressible equations during a full cycle. . . . .	40
4.14	Convective part of the source term $\bar{\mathbf{v}} \cdot \nabla p^{\text{ic}}$ as it is present in the PCWE formulation during a full cycle. . . . .	40
4.15	Convective part of the source term $\bar{\mathbf{v}} \cdot \nabla p^{\text{ic}}$ as it is present in the PCWE formulation during a full cycle. . . . .	41
4.16	Visualization of $\mathbf{v} \cdot \nabla p^{\text{ic}}$ for in the frequency domain. . . . .	42
4.17	Visualization of $\bar{\mathbf{v}} \cdot \nabla p^{\text{ic}}$ for in the frequency domain. . . . .	43

4.18	$\partial p^{ic}/\partial t$ during a full cycle. . . . .	43
4.19	Visualization of $\partial p^{ic}/\partial t$ for in the frequency domain. . . . .	44
4.20	PCWE source term during a full cycle. . . . .	45
4.21	Visualization of $\partial p^{ic}/\partial t + \bar{\mathbf{v}} \cdot \nabla p^{ic}$ in the frequency domain. . . . .	46
4.22	Comparison of the flow pressure time derivative and convective source term along the center line in x direction . . . . .	47
4.23	Global averaged source of the partial derivative and the convective term .	48
4.24	Sound pressure level of simulations and measurement data . . . . .	49
5.1	Experimental setup. . . . .	52
5.2	CFD mesh . . . . .	53
5.3	Geometry of acoustic domain . . . . .	54
5.4	Acoustic pressure field in a cross-section of the CAA domain . . . . .	55
5.5	PSD comparison . . . . .	56
5.6	Nodal values comparison . . . . .	57
5.7	Different meshes . . . . .	58
5.8	PSD for different discretizations . . . . .	59
5.9	Grid convergence regarding mesh refinement using Richardson Extrapolation. . . . .	62
5.10	Histogram of the averaged sound pressure level of the measurement. . . .	62

# List of Tables

3.1	Ratio of the energy corresponding to the actual wavelength and the total energy . . . . .	21
3.2	Different meshes used in the source region to investigate the cut-volume cell interpolation. . . . .	24
3.3	Averaged deviations in the acoustic results between reference mesh and finer or coarser meshes . . . . .	26
5.1	Different meshes used in the source region . . . . .	58
5.2	Comparison of the sound pressure level and the deviation of the power spectral density . . . . .	60
5.3	GCI based on Richardson Extrapolation and measurement results . . . . .	61



Die approbierte gedruckte Originalversion dieser Diplomarbeit ist an der TU Wien Bibliothek verfügbar.  
The approved original version of this thesis is available in print at TU Wien Bibliothek.

# Bibliography

- [1] Elaine Smith, Katherine Verdolini, Steven Gray, Sara Nichols, Jon Lemke, Julie Barkmeier, Heather Dove, and Henry Hoffman. Effect of voice disorders on quality of life. *Journal of Medical Speech-Language Pathology*, 4(4):223–244, 1996.
- [2] Seth M Cohen. Self-reported impact of dysphonia in a primary care population: An epidemiological study. *The Laryngoscope*, 120(10):2022–2032, 2010.
- [3] Ray M Merrill, Allison E Anderson, and Arielle Sloan. Quality of life indicators according to voice disorders and voice-related conditions. *The Laryngoscope*, 121(9):2004–2010, 2011.
- [4] Enda Murphy and Eoin King. *Environmental noise pollution: Noise mapping, public health, and policy*. Newnes, 2014.
- [5] Stefan Schoder, Paul Maurerlehner, Andreas Wurzinger, Klaus Roppert, Sebastian Falk, Stefan Kniesburges, Michael Döllinger, and Manfred Kaltenbacher. Aeroacoustic source term analysis of human voiceproduction - perturbed convective wave equation. *In preparation*.
- [6] Stefan Schoder, Andreas Wurzinger, Clemens Junger, Michael Weitz, Clemens Freidhager, Klaus Roppert, and Manfred Kaltenbacher. Application limits of conservative source interpolation methods using a low mach number hybrid aeroacoustic workflow. *In preparation*.
- [7] Franz Durst. *Grundlagen der Strömungsmechanik: eine Einführung in die Theorie der Strömung von Fluiden*. Springer-Verlag, 2007.
- [8] Manfred Kaltenbacher. *Theoretical Acoustics, lecture script*, 2017.
- [9] Stefan Schoder and Manfred Kaltenbacher. Hybrid aeroacoustic computations: State of art and new achievements. *Journal of Theoretical and Computational Acoustics*, 27(04):1950020, 2019.
- [10] Michael James Lighthill. On sound generated aerodynamically i. general theory. *Proceedings of the Royal Society of London. Series A. Mathematical and Physical Sciences*, 211(1107):564–587, 1952.

- [11] Michael James Lighthill. On sound generated aerodynamically ii. turbulence as a source of sound. *Proceedings of the Royal Society of London. Series A. Mathematical and Physical Sciences*, 222(1148):1–32, 1954.
- [12] N Curle. The influence of solid boundaries upon aerodynamic sound. *Proceedings of the Royal Society of London. Series A. Mathematical and Physical Sciences*, 231(1187):505–514, 1955.
- [13] JE Ffowcs Williams and David L Hawkings. Sound generation by turbulence and surfaces in arbitrary motion. *Philosophical Transactions for the Royal Society of London. Series A, Mathematical and Physical Sciences*, pages 321–342, 1969.
- [14] JC Hardin and DS Pope. An acoustic/viscous splitting technique for computational aeroacoustics. *Theoretical and computational fluid dynamics*, 6(5-6):323–340, 1994.
- [15] Wen Zhong Shen and Jens Nørkær Sørensen. Aeroacoustic modelling of low-speed flows. *Theoretical and Computational Fluid Dynamics*, 13(4):271–289, 1999.
- [16] Roland Ewert and Wolfgang Schröder. Acoustic perturbation equations based on flow decomposition via source filtering. *Journal of Computational Physics*, 188(2):365–398, 2003.
- [17] Jung-Hee Seo and Young J Moon. Perturbed compressible equations for aeroacoustic noise prediction at low mach numbers. *AIAA journal*, 43(8):1716–1724, 2005.
- [18] Claus-Dieter Munz, Michael Dumbser, and Sabine Roller. Linearized acoustic perturbation equations for low mach number flow with variable density and temperature. *Journal of Computational Physics*, 224(1):352–364, 2007.
- [19] A Hüppe. *Spectral finite elements for acoustic field computation (Measurement-, Actuator-, and Simulation-technology)*. PhD thesis, Ph. D. thesis, Shaker Verlag GmbH, doi: 10.2370/9783844024609, 2014.
- [20] DG Crighton. Computational aeroacoustics for low mach number flows. In *Computational aeroacoustics*, pages 50–68. Springer, 1993.
- [21] Claus Wagner, Thomas Hüttl, and Pierre Sagaut. *Large-eddy simulation for acoustics*, volume 20. Cambridge University Press, 2007.
- [22] Manfred Kaltenbacher. *Numerical simulation of mechatronic sensors and actuators*, volume 2. Springer, 2007.
- [23] Nathan M Newmark. A method of computation for structural dynamics. *Journal of the engineering mechanics division*, 85(3):67–94, 1959.

- [24] Stefan J. Schoder, Clemens Junger, Michael Weitz, and Manfred Kaltenbacher. Conservative interpolation of aeroacoustic sources in a hybrid workflow applied to fan. <https://arxiv.org/abs/2009.02341>, 2020.
- [25] M Kaltenbacher, M Escobar, S Becker, and I Ali. Numerical simulation of flow-induced noise using les/sas and lighthill's acoustic analogy. *International journal for numerical methods in fluids*, 63(9):1103–1122, 2010.
- [26] Patrick J Roache. Quantification of uncertainty in computational fluid dynamics. *Annual review of fluid Mechanics*, 29(1):123–160, 1997.
- [27] Ismail Celik, U Ghia, P.J. Roache, Chris Freitas, H Coloman, and Peter Raad. Procedure of estimation and reporting of uncertainty due to discretization in cfd applications. *J. Fluids Eng.*, 130:078001, 07 2008.
- [28] Stefan Schoder, Michael Weitz, Paul Maurerlehner, Alexander Hauser, Sebastian Falk, Stefan Kniesburges, Michael Döllinger, and Manfred Kaltenbacher. Hybrid aeroacoustic approach for the efficient numerical simulation of human phonation. *The Journal of the Acoustical Society of America*, 147(2):1179–1194, 2020.
- [29] Stefan Kniesburges. *Fluid-Structure-Acoustic Interaction during Phonation in a Synthetic Larynx Model: Fluid-Struktur-Akustik-Interaktion Während der Phonation in Einem Künstlichen Kehlkopfmodell*. PhD thesis, FAU Erlangen, 2014.
- [30] Stefan Kniesburges, Veronika Birk, Alexander Lodermeier, Anne Schützenberger, Christopher Bohr, and Stefan Becker. Effect of the ventricular folds in a synthetic larynx model. *Journal of Biomechanics*, 55:128–133, 2017.
- [31] Ronald C Scherer, Daoud Shinwari, Kenneth J De Witt, Chao Zhang, Bogdan R Kucinski, and Abdollah A Afjeh. Intraglottal pressure profiles for a symmetric and oblique glottis with a divergence angle of 10 degrees. *The Journal of the Acoustical Society of America*, 109(4):1616–1630, 2001.
- [32] Scott L Thomson, Luc Mongeau, and Steven H Frankel. Physical and numerical flow-excited vocal fold models. In *Third International Workshop on Models and Analysis of Vocal Emissions for Biomedical Applications*, 2003.
- [33] Franck Nicoud and Frédéric Ducros. Subgrid-scale stress modelling based on the square of the velocity gradient tensor. *Flow, turbulence and Combustion*, 62(3):183–200, 1999.
- [34] Hossein Sadeghi, Stefan Kniesburges, Sebastian Falk, Manfred Kaltenbacher, Anne Schützenberger, and Michael Döllinger. Towards a clinically applicable computational larynx model. *Applied Sciences*, 9(11):2288, 2019.

- [35] Barbara Kaltenbacher, Manfred Kaltenbacher, and Imbo Sim. A modified and stable version of a perfectly matched layer technique for the 3-d second order wave equation in time domain with an application to aeroacoustics. *Journal of computational physics*, 235:407–422, 2013.
- [36] S Zörner, P Sidlof, A Hüppe, and M Kaltenbacher. Flow and acoustic effects in the larynx for varying geometries. *Acta Acustica united with Acustica*, 102(2):257–267, 2016.
- [37] International Organization for Standardization. ISO 5801:2007 Industrial fans — Performance testing using standardized airways, 2007.
- [38] Manfred Kaltenbacher, Andreas Hüppe, Aaron Reppenhagen, Florian Zenger, and Stefan Becker. Computational aeroacoustics for rotating systems with application to an axial fan. *AIAA journal*, 55(11):3831–3838, 2017.
- [39] P. Welch. The use of fast fourier transform for the estimation of power spectra: A method based on time averaging over short, modified periodograms. *IEEE Transactions on Audio and Electroacoustics*, 15(2):70–73, 1967.
- [40] Fredric J Harris. On the use of windows for harmonic analysis with the discrete fourier transform. *Proceedings of the IEEE*, 66(1):51–83, 1978.
- [41] Florian Krömer, Johannes Müller, and Stefan Becker. Investigation of aeroacoustic properties of low-pressure axial fans with different blade stacking. *AIAA Journal*, 56(4):1507–1518, 2018.